ERA - Enhanced Retrieval of Aerosol properties: reference and NRT algorithm prototype for 3MI mission

Task Proposal for Enhanced Aerosol Retrieval Algorithm

FINAL REPORT

Testing of Enhanced NRT aerosol retrieval algorithm

Prepared by

Oleg Dubovik, Pavel Litvinov, Florian Poustomis, Jean-Francois Vinuesa, David Fuertes and Fabrice Ducos

Document	Author	Organization
Final Report	Oleg Dubovik	LOA: Laboratoire d'Optique Atmospherique, CNRS UMR8518
	Pavel Litvinov	GRASP - SAS: Generalized Retrieval of Atmosphere and Surface Properties
	Florian Poustomis	NOVLETIS
	Jean-Francois Vinuesa	NOVLETIS
	David Fuertes	GRASP - SAS: Generalized Retrieval of Atmosphere and Surface Properties
	Fabrice Ducos	LOA: Laboratoire d'Optique Atmospherique, CNRS UMR8518

Content

Overview of the project

The work in this this project includes three complimentary parts:

1. The focus of the work was on the development and testing of the state-of-the art algorithm for near-real-time (NRT) retrieval of aerosol microphysical and optical properties from 3MI instrument observations on EUMETSAT Polar System – Second Generation (EPS-SG).
2. Second important part of study was devoted to the development and testing a function for co-registration of Level 1B 3MI data in order to generate 3MI data of Level 1C.
3. The work also includes effort on testing existing EUMETSAT Look-Up-Table (LUT) retrieval algorithm. However, based on the results of the study, it was decided to reduce the work on analysis of LUT approach within this study (see some explanations in part describing Task 3).

The project efforts were organized via sequent sub-work packages tasks as illustrated on organogram in Fig.1. The detailed description of the work in each WP – Tasks are discussed below corresponding Sections.

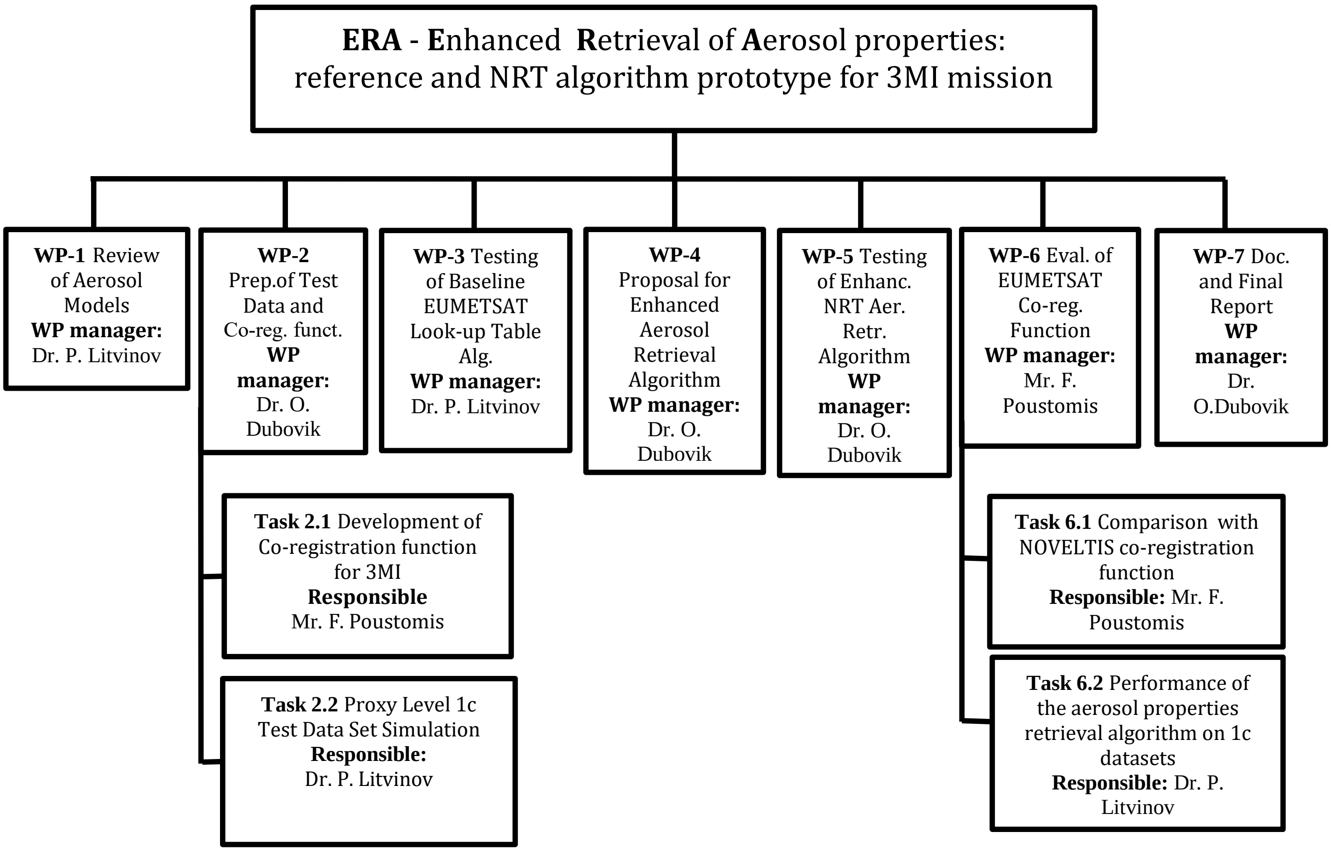

Figure 1. Work breakdown structure

1. TASK 1: Review of aerosol model chosen for LUT algorithm

1.1 Aerosol models in LUT EUMETSAT 3MI algorithm

EUMETSAT 3MI aerosol model covers several distinct types of aerosols: oceanic, continental, continental polluted, dust, volcanic and smoke (Kokhanovsky et al., 2016). Atmospheric aerosol is usually composed of fine and coarse fractions. EUMETSAT 3MI aerosol model contains one fine mode fraction and six coarse fractions (Table 1.1).

Table 1.1 Fine and coarse mode fractions (the complex refractive index (Re(m) and Im(m)) and the parameters of size distribution (average radius a_0 and logarithm of standard deviation s of log-normal size distribution)) of EUMETSAT 3MI aerosol model (more detailed description can be found in (Kokhanovsky et al., 2016).

Fine mode	Coarse mode
Spectral dependent *m is* defined in 12 3MI spectral channels. Re(m): 1.418 (410 nm) - 1.321 (2130 nm) Im(m): 0.0023 (410 nm) – 0.007 (1650 nm) – 0.0037 (2130 nm) Size distribution a_0= 0.0804; s = 0.43. Spherical particles.	**1. Continental clean** Re(m): 1.42 (410 nm) – 1.45 (1650) – 1.4 (2130 nm); Im(m) = 0.001. a_0 = 0.34; s = 0.72. Spherical particles. **2. Continental pollution** Re(m): 1.42 (410 nm) – 1.45 (1650) – 1.4 (2130 nm); Im(m) = 0.01. a_0 = 0.918; s = 0.63. Spherical particles. **3. Oceanic** Re(m): 1.36 (410 nm) – 1.307 (2130 nm); Im(m): 0 (410) - 0.001 (2130 nm). a_0= 0.547; s = 0.72. Spherical particles. **4. Smoke** Re(m): 1.53 (410 nm) – 1.585 (865 nm)- 1.4(2130 nm); Im(m) = 0.01 . a_0 = 0.46; s = 0.81. Spherical particles. **5. Dust** Re(m) = 1.56. Im(m) = 0.003 – 0.001 . a_0= 0.788; s = 0.6. Non-Spherical particles. **6. Volcanic** Re(m): 1.5 - 1.46. Im(m) = 0.008. a_0= 0.59; s = 0.56. Spherical particles.

1.2 Evaluation of EUMETSAT 3MI aerosol model

The physical basis of EUMETSAT 3MI aerosol model was considered through comparison with with several existent aerosol models:

- Aerosol models for look up table retrieval from PARASOL instrument (Deuzé et al., 2000; Herman at al., 2005; De Leeuw, et al., 2015)
- Aerosol CCI (Climate Change Initiative) model for AATSR, MERIS and future Sentinel-3 (SLSTR, OLSI) instruments (De Leeuw, et al., 2015; Holzer-Poppet al., 2013).
- Aerosol model used in MISR retrieval (Kahn and Gaitley, 2015).

- Climatological aerosol models from AERONET (Dubovik et al., 2002).

In terms of aerosol type classification and microphysical aerosol properties description, EUMETSAT 3MI aerosol models are very close to key aerosol types description from AERONET worldwide locations (Dubovik et al., 2002). Dubovik et al. (2002) identified urban-industrial and mixed aerosol; biomass burning; desert dust and oceanic aerosol and discussed the variability of their detailed properties depending on geolocation.

The following criteria was used for evaluation of the aerosol model:

1. **Adequate Representation** of Fine and Coarse mode of dominated aerosols.
2. ***Comprehensive Representation*** of aerosol microphysical properties (complex refractive index, size parameter, nonspherisity).
3. **Ability** (*flexibility*) of representing of mixed aerosols appearance.

Figure 1.1 shows typical size distribution for five AERONET-based climatological aerosol types (Dubovik at al. 2002).

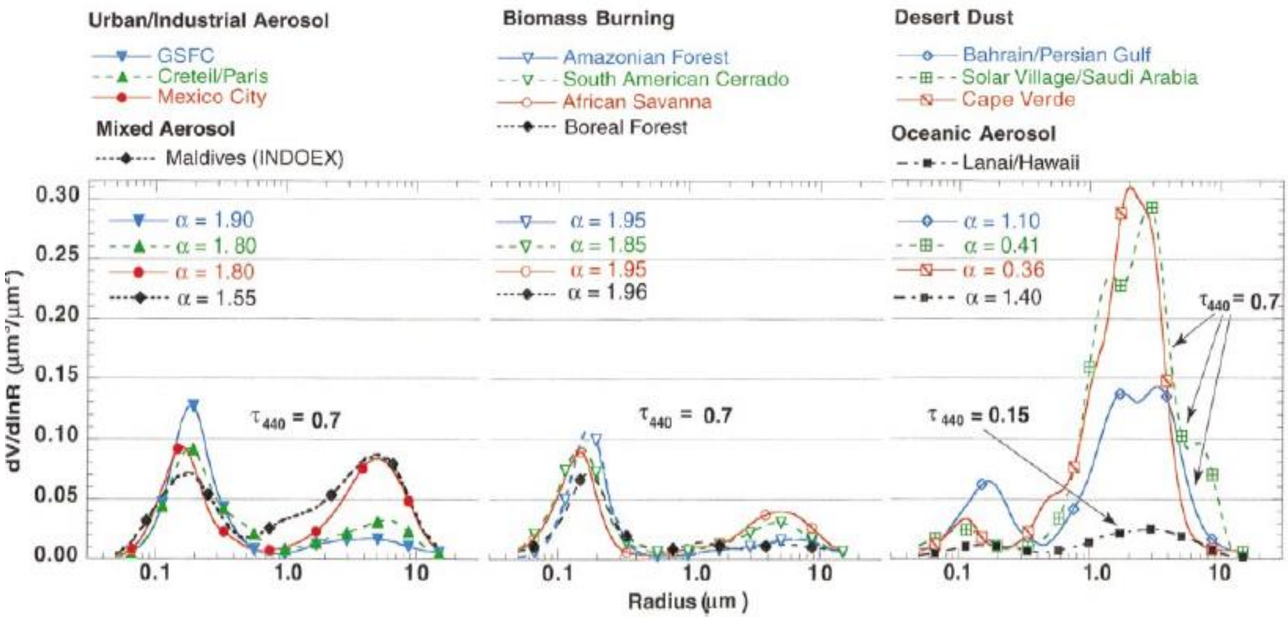

Figure 1.1 Size distribution for 5 AERONET-based climatological aerosol types (Dubovik at al. 2002).

EUMETSAT 3MI aerosol models clearly cover major aerosol types following from the AERONET climatology. Nevertheless, the microphysical description of the fine and the coarse mode aerosols by the EUMETSAT 3MI models should be modified. As it follows from Fig.1, depending on the aerosol type, the two modes (fine and coarse) can be of the same order (Urban/Industrial, Mixed, Oceanic) or one of the modes can be dominating (fine mode for biomass burning and coarse mode for dust aerosol). Current EUMETSAT 3MI models contain only one aerosol mode (Table 1.1). This is likely not enough for description of the fine mode of absorbing aerosols such as urban polluted aerosol or biomass burning (Dubovik at al. 2002). The description of the fine mode of the oceanic aerosol may need to be modelled as less absorbing aerosol with the refractive index closer to 1.33 than in the existent EUMETSAT fine mode (Dubovik at al. 2002). The microphysical properties of the coarse modes in EUMETSAT model is consistent with AERONET-based aerosol climatological models. Retrieval of volcanic ash microphysical properties shows domination of nonspherical particles in coarse mode (Derimian et al., 2012), while EUMETSAT 3MI aerosol model of volcanic ash does not take into account the nonspehricity (Table 1.1).

Table 1.2 EUMETSAT 3MI aerosol model limitations

Aerosol type	Fine	Coarse
Continental clean	Available	Available
Continental polluted	Can not be covered by the existent fine mode (Can be the same as Fine smoke mode)	Available
Oceanic	Can not be covered by the existent fine mode	Available
Smoke	Can not be covered by the existent fine mode	Available (Can be neglected if necessary)
Dust	Can be neglected	Available
Volcanic	Can be neglected	Available (Volcanic particles are rather nonspherical (Derimian et al., 2012). Modifications are recommended)

1.3 Recommended changes in EUMETSAT selection of aerosol models

Recommendations for the modifications:

1. It is recommended to add three fine modes with the same refractive index as provided for coarse mode in EUMETSAT 3MI aerosol models.
2. For all new fine modes it is recommended to keep the same parameter of SD (Size Distribution) as for current fine mode:

   a_{0f}=0.08 μm, s=0.43

$$f(a) = \frac{c}{\sqrt{2\pi} s_f a} \exp\left[-\frac{1}{2s_f^2} \ln \frac{a}{a_{0f}}\right] + \frac{1-c}{\sqrt{2\pi} s_c a} \exp\left[-\frac{1}{2s_c^2} \ln \frac{a}{a_{0c}}\right]$$

3. It is recommended to take model of non-spherical particles for volcanic aerosol.

The detailed microphysical properties for proposed aerosol models are described in Tables 1.3-1.6.

Table 1.3 Real part of the refractive index for 3 fine modes.

λ, nm	410	443	490	555	670	763	765	865	910	1370	1650	2130
Oceanic	1.36	1.36	1.36	1.35	1.35	1.35	1.35	1.345	1.345	1.340	1.333	1.307
Continental clean	1.42	1.42	1.42	1.42	1.43	1.43	1.43	1.44	1.44	1.44	1.45	1.40
Smoke	1.53	1.53	1.53	1.54	1.55	1.56	1.56	1.585	1.58	1.50	1.50	1.40

Table 1.4 Imaginary part of the refractive index for 3 fine modes

λ, nm	410	443	490	555	670	763	765	865	910	1370	1650	2130
Oceanic	5.e-9	4.e-9	3.e-9	3.e-9	3.e-8	3.e-7	3.e-7	5.e-6	6.e-6	1.e-4	2.e-4	1.e-3
Continental clean	0.001	0.001	0.001	0.001	0.001	0.001	0.001	0.001	0.001	0.001	0.001	0.001
Smoke	0.01	0.01	0.01	0.01	0.01	0.01	0.01	0.01	0.01	0.01	0.01	0.01

Table 1.5 Real part of the refractive index for 5 coarse modes

λ, nm	410	443	490	555	670	763	765	865	910	1370	1650	2130
Continental clean	1.42	1.42	1.42	1.42	1.43	1.43	1.43	1.44	1.44	1.44	1.45	1.40
Dust	1.56	1.56	1.56	1.56	1.56	1.56	1.56	1.56	1.56	1.56	1.56	1.56
Oceanic	1.36	1.36	1.36	1.35	1.35	1.35	1.35	1.345	1.345	1.340	1.333	1.307
Continental plluted	1.42	1.42	1.42	1.42	1.43	1.43	1.43	1.44	1.44	1.44	1.45	1.40
Volcanic	1.50	1.50	1.50	1.50	1.50	1.50	1.50	1.50	1.50	1.50	1.48	1.46

Table 1.6 Imaginary part of the refractive index for 5 coarse modes

λ, nm	410	443	490	555	670	763	765	865	910	1370	1650	2130
Continental clean	0.001	0.001	0.001	0.001	0.001	0.001	0.001	0.001	0.001	0.001	0.001	0.001
Dust	0.0032	0.0029	0.0024	0.0019	0.0013	0.00115	0.00115	0.001	0.001	0.001	0.001	0.001
Oceanic	5.e-9	4.e-9	3.e-9	3.e-9	3.e-8	3.e-7	3.e-7	5.e-6	6.e-6	1.e-4	2.e-4	1.e-3
Continental polluted	0.01	0.01	0.01	0.01	0.01	0.01	0.01	0.01	0.01	0.01	0.01	0.01
Volcanic	0.008	0.008	0.008	0.008	0.008	0.008	0.008	0.008	0.008	0.008	0.008	0.008

The parameters for the size distribution for 5 coarse modes can be kept as they are in the current ATBD Level 2 Algorithm Theoretical Basis Document (Aerosol).

Table 1.7 Assumed parameters of PSD for the coarse modes and non-shericity.

N	Aerosol type	$a_0, \mu m$	s	Reference	Comments

1	Oceanic(coarse)	0.5469	0.72	Sayer et al., 2012	The contribution of non-spherical particles is neglected
2	Continental clean (coarse)	0.3400	0.72	Dubovik et al., 2002	Spherical particles
3	Continental Pollution (coarse)	0.9181	0.63	Dubovik et al., 2002	Spherical particles
4	Dust (coarse)	0.7879	0.60	Dubovik et al., 2002	The particles are of non-spherical shape
5	Volcanic(coarse)	0.59	0.56	Derimian et al., 2012	The particles are of non-spherical shape

1.4 Summary of Task 1 resuluts

Aerosol Model sellection for EUMETSAT 3MI LUT algorithm is consistent with aerosol type identification from AERONET-based climatology (Dubovik et al., 2002). Aerosol refractive index and size distribution parameters of coarse mode represent well the aerosol types. Currently selected only one fine mode is not enough to describe the cases of absorbing aerosol like biomass burning. Due to domination of fine mode in smoke aerosol type, coarse mode can be neglected if there are requirements to reduce the size of LUT. Volcanic aerosol should be considered as non-spherical particles.

Presented section on Aerosol Model review is based on analysis of physical representativeness of EUMETSAT 3MI aerosol model LUT selection. However, aerosol model performance depends also on the retrieval algorithm design. Therefore, more feedbacks on aerosol model likely will be provided during fulfilment of Task 3 of ERA project when the retrieval algorithm will be tested on synthetic data set

2. TASK 2: Preparation of Test Data and Development of co-registration function

The work in this task included efforts on development of Co-registration function and preparation of test data sets based PARASOL and AERONET aerosol climatologies

2.1 TASK 2.1: Development of co-registration function

2.1.1 Introduction

This section describes the work carried out by NOVELTIS in the task 2.1: Simulated Level L1C Test Data Set. This task consists in processing level 1B data for level 1C generation.

The low orbit instrument 3MI on-board the Second Generation of Metop platform will acquire successive measurements in a short time laps while the satellite moves along its orbit enables to look at a target under different viewing angles, each measurement covering a very large footprint and scanning several spectral bands on a wide spectral domain. Each measurement will be shifted from its previous one due to the displacement of the satellite. Each target will be viewed under 14 VNIR angles and 7 SWIR angles. This target has to be geo-localized and co-registered. Moreover, each target will be viewed under several spectral bands acquired successively in a time-lapse of 7 seconds. During this short period, the satellite displacement leads to a shift of the footprint of each spectral images.

The different modules used in the level 1B to level 1C conversion are scripted and enable to process routinely the 3MI measurements. The processing chain is described in section 2.1.2. The co-registration method used in the first step is detailed in section 2.1.3. Then the orthorectification is applied and the data is reprojected in a global grid, see section 2.1.4. Finally an overlap between the several views is computed, as is described in section 2.1.5.

2.1.2 L1B to L1C processing chain

Level 1B files of the 3MI measurements contain information on geolocation, radiances and ancillary data for 14 VNIR angles at 9 wavelengths and 28 SWIR angles at 4 wavelengths. Table 2.1 and Table 2.2 described the L1B VNIR and SWIR radiances at each channel, respectively.

We notice that only 3 SWIR wavelengths are necessary for the 3MI L1C data (1370, 1650 and 2130nm) so the 910mn SWIR channel should not be processed. The number of VNIR and SWIR angles in each L1B file is schematized in Table 2.3.

Table 2.1 : List and description of L1B VNIR radiances datasets for VNIR channels

Dataset name	Description and units	Dimension
3mi_00410	I, Q and U Stokes vector components for the 410 nm channel (in W m-2 sr-1 microns-1)	4-D (14x3 x512x512)(1) vector
3mi_00443	I, Q and U Stokes vector components for the 443 nm channel (in W m-2 sr-1 microns-1)	4-D (14x3 x512x512)(1) vector
3mi_00490	I, Q and U Stokes vector components for the 490 nm channel (in W m-2 sr-1 microns-1)	4-D (14x3 x512x512)(1) vector
3mi_00555	I, Q and U Stokes vector components for the 555 nm channel (in W m-2 sr-1 microns-1)	4-D (14x3 x512x512)(1) vector
3mi_00670	I, Q and U Stokes vector components for the 670 nm channel (in W m-2 sr-1 microns-1)	4-D (14x3 x512x512)(1) vector
3mi_00763	I, Q and U Stokes vector components for the 763 nm channel (in W m-2 sr-1 microns-1)	4-D (14x3 x512x512)(1) vector
3mi_00765	I, Q and U Stokes vector components for the 765 nm channel (in W m-2 sr-1 microns-1)	4-D (14x3 x512x512)(1) vector
3mi_00865	I, Q and U Stokes vector components for the 865 nm channel (in W m-2 sr-1 microns-1)	4-D (14x3 x512x512)(1) vector
3mi_00910b	I, Q and U Stokes vector components for the 910 nm channel (in W m-2 sr-1 microns-1)	4-D (14x3 x512x512)(1) vector

Table 2.2 : List and description of L1B SWIR radiances datasets for VNIR channels

Dataset name	Description and units	Dimension
3mi_00910a	I, Q and U Stokes vector components for the 763 nm channel (in W m-2 sr-1 microns-1)	4-D (28x3 x512x512)(1) vector
3mi_01370	I, Q and U Stokes vector components for the 765 nm channel (in W m-2 sr-1 microns-1)	4-D (28x3 x512x512)(1) vector
3mi_01650	I, Q and U Stokes vector components for the 865 nm channel (in W m-2 sr-1 microns-1)	4-D (28x3 x512x512)(1) vector
3mi_02130	I, Q and U Stokes vector components for the 910 nm channel (in W m-2 sr-1 microns-1)	4-D (28x3 x512x512)(1) vector

Table 2.3 : L1B file angles

<table>
<tr><td></td><td colspan="28">L1B file 1</td></tr>
<tr><td>VNIR angle</td><td colspan="2">1</td><td colspan="2">2</td><td colspan="2">3</td><td colspan="2">4</td><td colspan="2">5</td><td colspan="2">6</td><td colspan="2">7</td><td colspan="2">8</td><td colspan="2">9</td><td colspan="2">10</td><td colspan="2">11</td><td colspan="2">12</td><td colspan="2">13</td><td colspan="2">14</td></tr>
<tr><td>SWIR angle</td><td>1</td><td>2</td><td>3</td><td>4</td><td>5</td><td>6</td><td>7</td><td>8</td><td>9</td><td>10</td><td>11</td><td>12</td><td>13</td><td>14</td><td>15</td><td>16</td><td>17</td><td>18</td><td>19</td><td>20</td><td>21</td><td>22</td><td>23</td><td>24</td><td>25</td><td>26</td><td>27</td><td>28</td></tr>
</table>

The first step of the processing chain consists in extracting the desired data from the L1B files to generate a L1C overlap. A L1C overlap is the resulting area of the intersection between data acquired at 14 VNIR consecutive angles and at 7 SWIR consecutive angles. A L1C overlap is made of 14 VNIR angles at the 9 VNIR wavelengths and 7 SWIR angles at the 3 SWIR L1C wavelengths and could be considered as a fictitious central image viewed along several directions and spectral filters. Figure 2.1 shows the overlap of the I component at 410nm acquired at the first VNIR angle of a L1B file (angle #1) and at the last VNIR angle of the same L1B file (angle #14 in transparency). Figure 2.2 shows the overlap of the I component at 1370nm acquired at the first SWIR angle of a L1B file (angle #1) and at the last SWIR angle of the same L1B file (angle #28). The overlap is null and that is why a L1C overlap is the intersection of just 7 SWIR angles among the 28 available in the L1B files. Acquisitions along maximum 7 consecutive SWIR angles can be overlapped without generating gaps because of the SWIR acquisition footprint. More information concerning the overlap generation is given in section 2.1.5.

For an acquisition at a given wavelength and angle, an image is built with 6 or 9 bands by extracting information from the L1B data files. Each image has 3 bands for the I, U and Q components and 3 bands for the geometric angles, the satellite zenith angle, the solar zenith angle and the relative azimuth angle. Moreover, the images generated for the data acquired at 670nm and 1370nm (and at all the VNIR and SWIR angles respectively) have 3 more bands corresponding to the cloud mask, the land/water mask and snow-ice mask for VNIR and SWIR data respectively. The hypothesis that a mask at a VNIR (SWIR respectively) angle is the same for all the VNIR (SWIR respectively) wavelengths at this viewing angle is done.

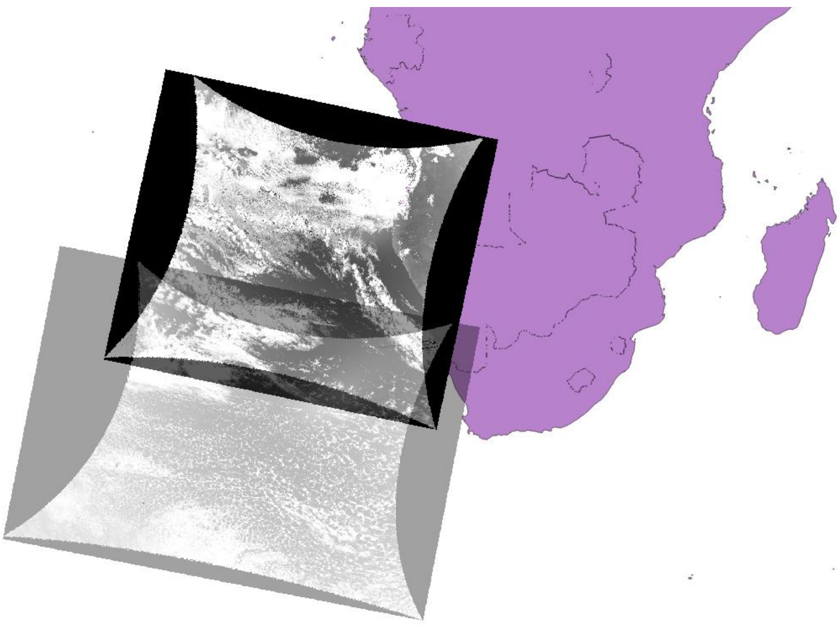

Figure 2.1 : overlap of the I component at 410nm acquired at the first and the last VNIR angles of a L1B file

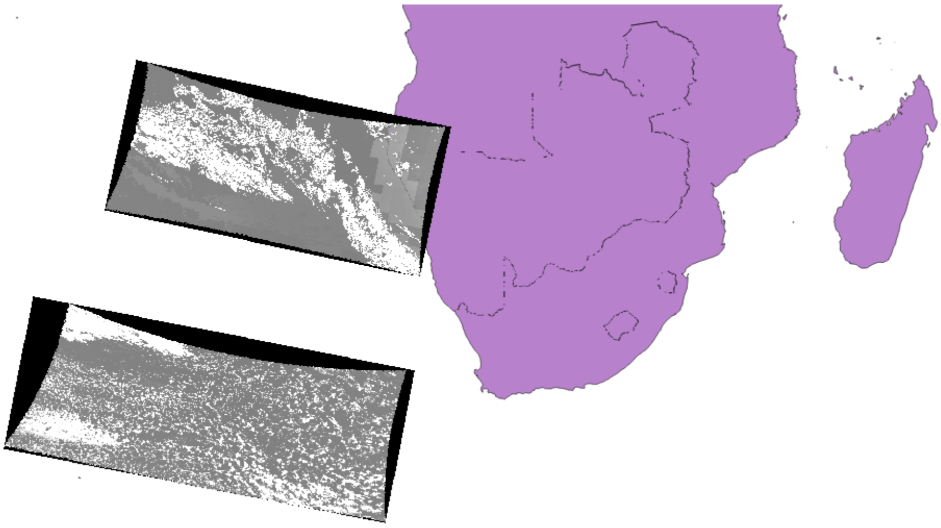

Figure 2.2 : overlap of the I component at 1370nm acquired at the first and the last SWIR angles of a L1B file

So in the first loop, a L1C overlap will be generated with the angle VNIR #7 as central angle. Thus, data for the 14 VNIR angles is extracted from the L1B file 1. As two SWIR angles "correspond" to one VNIR angle, data for two sets of 7 consecutive SWIR angles are extracted (corresponding to 8 SWIR angles), as coloured in the top table in Table 2.4 . Figure 2.3 shows the areas of the intersections of the 14 VNIR angles in red, of the 7 SWIR angles from #10 to #16 in green and of the 7 SWIR angles from #11 to #17 in blue. As is explained in section 2.1.5, the final L1C overlap results of the intersection of these three different overlaps.

Table 2.4: generation of overlap #1 and overlap #2

	L1B file 1																											
VNIR angle	1		2		3		4		5		6		7		8		9		10		11		12		13		14	
SWIR angle	1	2	3	4	5	6	7	8	9	10	11	12	13	14	15	16	17	18	19	20	21	22	23	24	25	26	27	28

	L1B file 1																											
VNIR angle	1		2		3		4		5		6		7		8		9		10		11		12		13		14	
SWIR angle	1	2	3	4	5	6	7	8	9	10	11	12	13	14	15	16	17	18	19	20	21	22	23	24	25	26	27	28

	L1B file 1																											
VNIR angle	1		2		3		4		5		6		7		8		9		10		11		12		13		14	
SWIR angle	1	2	3	4	5	6	7	8	9	10	11	12	13	14	15	16	17	18	19	20	21	22	23	24	25	26	27	28

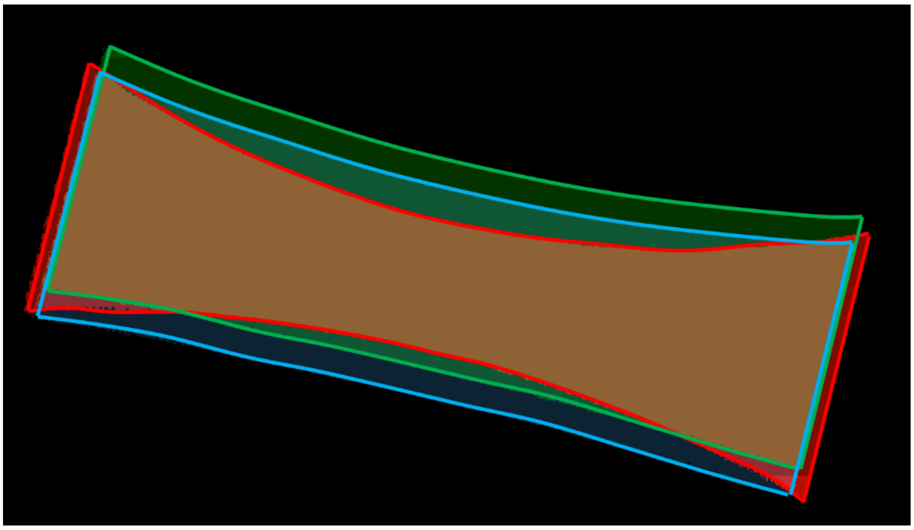

Figure 2.3 : different overlaps of 3MI angles

Thus, co-registration using the VNIR angle #7 as central angle is applied to data at all the extracted VNIR and SWIR angles. Then the data are orthorectified and reprojected in a global grid. The following step consists in generating the overlapping area. Finally L1C data is written in an output netCDF file, generating the overlap corresponding to the VNIR angle #7 of the L1B file. These different processing steps are explained in the following sections.

In the second loop, the input angles are incremented. As data acquired at 14 VNIR angles and two sets of 7 SWIR corresponding angles have to be extracted of the L1B files, a second L1B file must be opened and data acquired at the coloured angles in the bottom table in Table 2.4 are extracted. Then all the processing steps are applied (with then angle #8 as central angle for the co-registration) and the resulting L1C overlap is added to the output netCDF file generating a new overlap corresponding to the VNIR angle #8 of the L1B file.

At the end of the processing, there are as many output L1C files as input L1B files written. The L1B granularity has been kept at the L1C. In each L1C file (except for the first and the last ones), 14 overlaps have been generated, where each overlap is the intersection of the co-registered and orthorectified data acquired at 14 VNIR angles and 7 SWIR angles.

2.1.3 Co-registration

To ensure that multi-angle and multi-spectral images stack can be superimposed, allowing the comparison of pixel values for the same on-ground area in different images acquired on different angles and/or for different spectral bands, it is important to co-register images. NOVELTIS has developed a co-registration processing chain containing several images co-registration algorithms.

As is explained in the section2.1.2, a set of images corresponding to acquisitions along 14 VNIR angles at 9 wavelengths and along 8 SWIR angles at 3 wavelengths has to be co-registered using as a reference image the one that has been acquired at the central VNIR angle and wavelength, *i.e.* 670nm. The co-registration is computed using the first band of the images, *i.e.* the band containing the I component.

The algorithm used is based on feature extraction and it is divided in two steps:

- The collect of control points;

- The geometric transformation.

The collect of control points

The control points are collected according the following technique, as is illustrated in Figure 2.4. For each pixel in the base image, the corresponding pixel in the warp image is searched in a search window (red window in Figure 2.4) the central pixel of which is located at the predicted location of the searched pixel, *i.e.* at the same place as the base pixel in the base image (red pixel in the base image and pink pixel in the warp image in Figure 2.4). A patch around the control point location is used as a matching window (smaller than the search window, the green window in Figure 2.4). In the base image, the matching window which the central pixel is the pixel we want to retrieve in the warp image, is fixed. In the warp image, the matching window, which has the same size as the matching window in the base image, is mobile in the search window. For each pixel of the warp image in the search window, a matching window is located around the central pixel and all the pixels located into the matching window of the warp image are compared to the pixels located in the matching window of the base image.

Several matching methods exist but the most appropriate one in our case study is the mutual information. This method is optimized for registering images with different modalities (*i.e.* images acquired in different ways or at different wavelengths). The normalized mutual information between the matching window in the base image and the matching window in the warp image is computed as the matching score. Mutual information is based on information theory and measures the mutual dependence of the two random variables. Mutual information produces more accurate results than the traditional correlation based measures for cross-modality image registration. Thus, for each pixel in the base image, a corresponding pixel is found in the search window of the warp image. This selected pixel generates the highest matching score with the pixel in the base image among the matching scores of all the pixels located in the search window. Larger is the search window longer is the processing, but more shifted could be the base image and the warp image. Indeed, if the pixel offset between the two images to register is greater than the search window size, the search will not be able to detect corresponding features in the images. If the images are shifted of p pixels, the minimum search window size to use should be $2(p+5)$ pixels.

In our case, the images are not very shifted, so a small search window works perfectly.

A minimum matching score allows to filter the control points to keep only the bests by applying a threshold. The minimum requested number of control points is 9. However, as the geometric transformation applied to the warp image will be based on these control points, more control points, better the co-registration.

The error measurement represents the distance of each control point in the warp image to its predicted location, in pixel units. Higher errors may indicate bad control points. A threshold on this error is applied to remove control points too far from their predicted location. However, the best way to check the accuracy of the control points is to visually examine their placement in the base and warp images but it is not possible: because of the huge number of image to co-register, the function has been automatized.

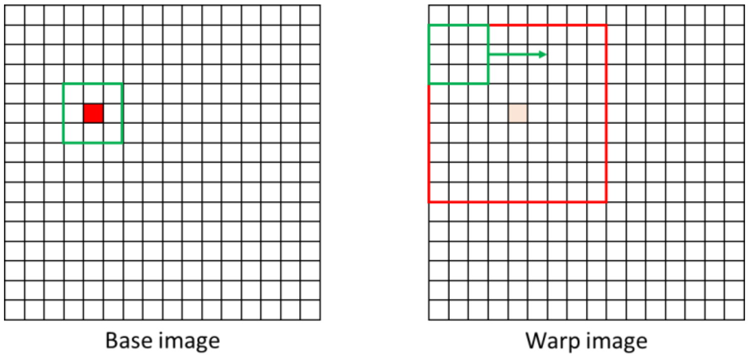

Figure 2.4 : control point selection

The geometric transformation

Once the control points have been selected and filtered, a geometric transformation based on these control points is applied to the warp image. Several warping methods exist:

- RST: Rotation, scaling, and translation, this is the simplest method. The RST warping algorithm uses an affine transformation:

$$x = a_1 + a_2X + a_3Y$$
$$y = b_1 + b_2X + b_3Y$$

This algorithm does not allow for shearing in the image warp;

- Polynomial: A first-order polynomial warp includes an XY interaction term to account for image shear:

$$x = a_1 + a_2X + a_3Y + a_4XY$$
$$y = b_1 + b_2X + b_3Y + b_4XY$$

- Triangulation: It is the most complex warping method that has to be used if there is local distortion between the base and warp images.

Different resampling methods are available:

- Nearest Neighbour;
- Bilinear;
- Cubic convolution.

Chosen parameters

As the different L1B views are not very shifted (some pixels only), the size of the search window is 31 pixels. The size of the matching window is 21 pixels. There is not a huge difference between the search window size and the matching window size such as the control points are found close from their predicted location.

The polynomial geometric transformation is applied to co-register the images as the images are very close.

The chosen resampling method is the Nearest Neighbour method, because the other ones (bilinear and cubic convolution) introduce a blurring in the co-registered images.

2.1.4 Orthorectification and reprojection

Orthorectification

The orthorectification method developed at NOVELTIS needs a DEM and RPC. However, RPCs are not available for 3MI data. But the orthorectification method from the Orfeo Toolbow developed by the CNES does not need RPC necessarily. So this method has been used with the ACE2 DEM at 9 arc sec. Unfortunately, without RPC, the method is not very efficient and no improvement is applied to the images after orthorectification. The generation of RPC should allow to better orthorectify the data.

Reprojection

The co-registered and orthorectified images should be reprojected in a fixed sinusoidal grid with 3.97km resolution corresponding to 28 grid sampling by degree of latitude. The whole Earth is thus covered by 10 080 x 5 040 cells.

The images are projected in a sinusoidal grid with cells of 3.97km resolution thanks to the gdalwarp function according the following projection definition '+proj=sinu +lon_0=0 +x_0=0 +y_0=0 +a=6371007.181 +b=6371007.181 +units=m +no_defs'. Then, the L1C row and column numbesr are computed thanks to the following formula:

$$row^{\#} = round\left(grid_{param}(lat^{\circ} + 90) - \frac{1}{2}\right)$$

$$column^{\#} = round\left(grid_{param}\left(\cos lat^{\circ}\left(long^{\circ} - ref_{long}\right) + 180\right) - \frac{1}{2}\right)$$

With $grid_{param} = 28$ and $ref_{long} = 5°$.

The latitude and longitude of each L1C cell can be retrieved thanks to the following formula:

$$lat^{\circ} = \frac{row^{\#} + \frac{1}{2}}{grid_{param}} - 90$$

$$long^{\circ} = \left(\frac{column^{\#} + \frac{1}{2}}{grid_{param}} - 180\right) \Big/ \cos lat^{\circ} + ref_{long}$$

2.1.5 Overlapping

After the reprojection, all the images for the L1C overlap must be cut. As is explained in section 2.1.2, a L1C overlap is the resulting area of the intersection between data acquired at 14 VNIR consecutive angles for all the VNIR wavelengths and at 7 SWIR consecutive angles for all the L1C SWIR wavelengths. A L1C overlap is made of 14 VNIR angles at the 9 VNIR wavelengths and 7 SWIR angles at the 3 SWIR L1C wavelengths and could be considered as a fictitious central image viewed along several directions and spectral filters.

Because of the different footprints between VNIR and SWIR acquisitions, three intersections are created as is shown in Figure 2.3. The red area is generated by intersecting the VNIR data selected for this L1C overlap acquired at 14 VNIR angles for the 9 VNIR wavelengths. The green area is generated by intersecting the first set of SWIR data selected for this L1C overlap acquired at 7 SWIR angles for the 3 SWIR wavelengths. Finally, the blue area is generated by intersecting the second set of SWIR data selected for this L1C overlap acquired at 7 SWIR angles (shifted of one angle compared to the first set) for the 3 SWIR wavelengths.

The global L1C overlap is the intersection of the red area and the sum of the green and blue areas. So the considered L1C overlap contains data acquired at the 14 VNIR angles for each VNIR wavelength in the intersection of the red area with the sum of the green and blue areas. The L1C overlap contains also data acquired at the first set of 7 SWIR angles (from #10 to #16 in the example section 2.1.2) at each SWIR L1C wavelength in the intersection of the red area with the green area, and data acquired at the second set of 7 SWIR angles (from #11 to #17 in the example section 2.1.2) at each SWIR L1C wavelength for each pixel in the intersection of the red area with the blue area but that is not in the green area. Indeed a L1C cell should have a unique value for a given band (radiances, geometric angles and masks), acquisition angle and wavelength, so if a cell is affected by a value because it is in the green area, this cell must not be affected by another value.

The same problem occurs on successive L1C overlaps. As is shown in Figure 2.5, two successive L1C overlaps have a common area. So all the cells of the overlap #2 that are already in another overlap (the overlap #1 in the example below) are not taken into account in the current overlap as is illustrated in the right map in Figure 2.5.

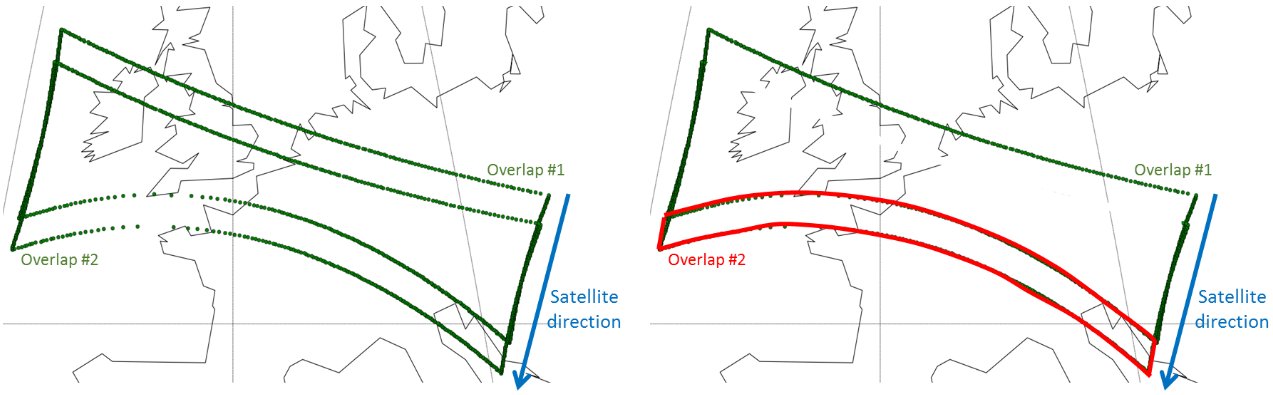

Figure 2.5 : successive L1C overlaps (before deleting the double cells on the left and after on the right)

So a L1C overlap could be viewed as a mask generated by the intersection of a VNIR mask and the sum of two SWIR masks. The cells of this L1C mask do not appear in other masks representing others L1C overlaps.
Figure 2.6 shows the I component acquired at 410nm and at the central angle associated to each successive overlap.

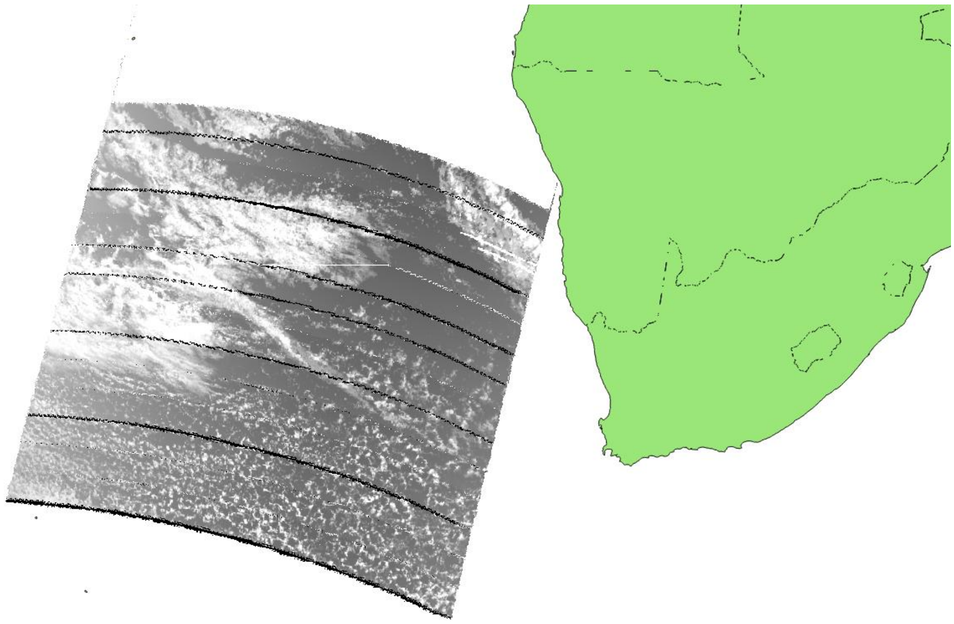

Figure 2.6 : I component acquired at 410nm and at the first VNIR angle for successive overlaps near South Africa

2.2 TASK: Preparation of Test Data

2.2.1 Approach for GRASP L1C test DATA Set Simulation

GRASP algorithm is designed both for data inversion and TOA measurements simulations. Indeed, GRASP can provide forward calculations using very accurate and complete atmosphere and surface radiation model. Combining this feature with 3MI instrument specification and illumination/measurements geometry definition the 3MI synthetic measurement can be generated. This approach has already been used for synthetic data simulation for PARASOL. In Task 2 it is used for GRASP Proxy Test Data Set simulation for 3MI.

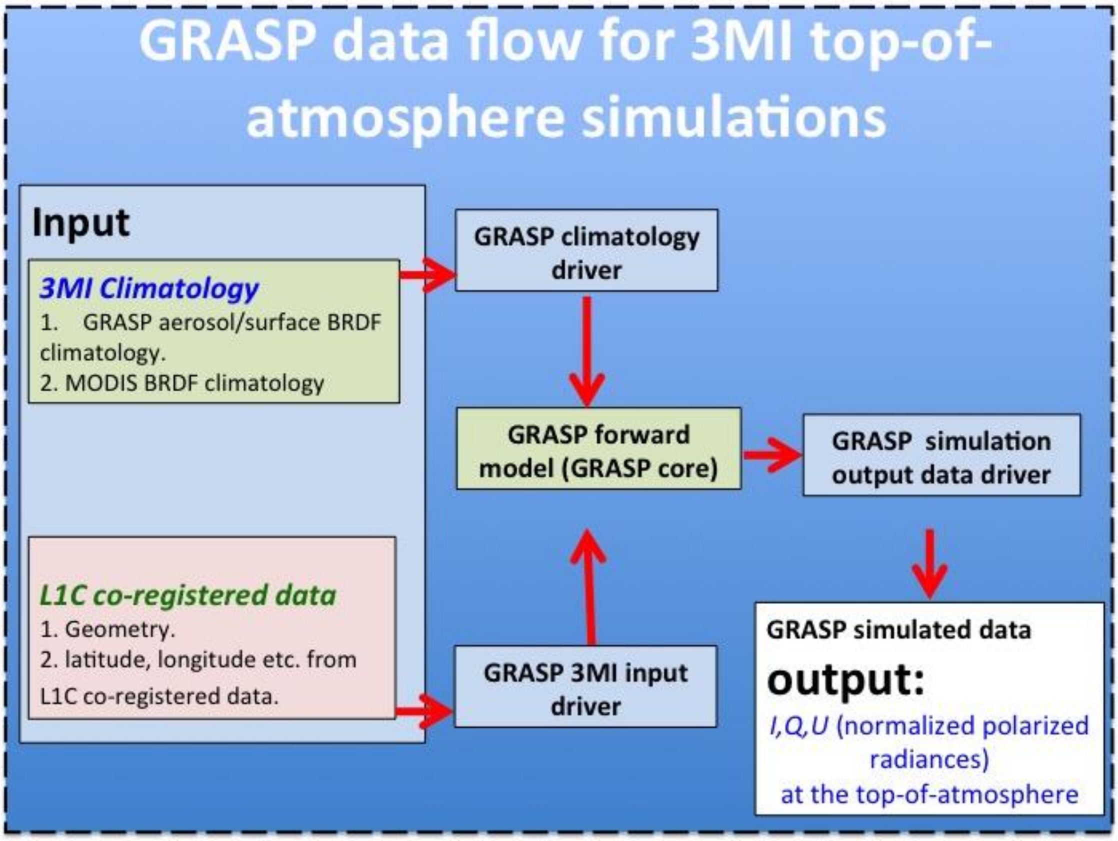

Figure 2.7 GRASP data flow for 3MI top-of-atmosphere simulation

In general, the approach requires the following inputs and drivers:

1) L1C co-registered data of identical structure as original EUMETSAT and NOVELTIS L1C (with 3MI geometry, latitude, longitude, surface elevation etc.).
2) Aerosol properties from GRASP/PARASOL climatology and surface properties from GRASP/PARASOL and MODIS BRDF climatology taken for pixels geo-collocated with L1C 3MI pixels.
3) GRASP climatology driver for aerosol/surface characteristics interpolation/extrapolation to 3MI channels.

4) GRASP 3MI driver for 3MI L1C data reading and preparation for GRASP inversion.
5) Forward model calculation of top of atmosphere Stokes vector with GRASP.
6) GRASP output driver for writing simulated data into 3MI L1C (or other) data format.

Within Task 2 all required components were developed and one orbit of 3MI synthetic measurements was simulated. In addition, the simulation of 3MI measurements were performed for aerosol/surface properties typical for certain AERONET stations (Banizoumbou, Mongu, Kanpur, Beijing, Forth-Crete) differ by their aerosol and surface properties. AERONET provides extended and accurate aerosol parameters: multispectral AOD, SSA, Angstrom exponent, complex refractive index, size distribution etc. This extended aerosol characterization is extremely useful for direct aerosol retrieval validation. In the AERONET based simulations the surface properties were taken from GRASP/PARASOL and MODIS BRDF climatology whereas the aerosol surfaces were taken from AERONET inversion and direct AOD measurements.

It should be note that in the GRASP simulation it is assumed that simulated top-of atmosphere values of all Stokes parameters *I, Q, U* are already corrected for gas absorption in all channels. Moreover, the simulation is performed for cloud free conditions and possible “missed values” for the certain pixels of the simulations are caused by absent of climatological values for these pixels.

2.2.2 GRASP climatology for 3MI

Interpolation/extrapolation to 3MI channels

GRASP 3MI climatology for 3MI orbits is based on GRASP/PARASOL aerosol and surface retrieval climatology and combined GRASP/PARASOL and MODIS surface BRDF climatology. To avoid unphysical values, all interpolation/extrapolation of aerosol/surface characteristics were performed in logarithmic scale. Assuming linear dependence

$$\ln x = -\alpha \ln \lambda + \beta, \tag{2.1}$$

the value of a parameter x at wavelength λ can be defined from the value of x_1 at the wavelength λ_1 as follows:

$$x = x_1 \left(\frac{\lambda}{\lambda_1} \right)^{-\alpha}, \tag{2.2}$$

where Angstrom Exponent α of a parameter x can be defined from the known values at two wavelengths λ_1 and λ_2:

$$\alpha = -\frac{\ln(x_1/x_2)}{\ln(\lambda_1/\lambda_2)}. \tag{2.3}$$

2.2.3 GRASP aerosol climatology for 3MI

GRASP aerosol model

GRASP aerosol single scattering properties are being calculated following the ideas developed in retrieval algorithm by Dubovik and King (2000), Dubovik et al. (2006) employed in operational processing the AERONET network of ground-based sun-photometers (Holben et al. 1998). In order to account for aerosol non-sphericity, the atmospheric aerosol is modelled as an ensemble of randomly oriented spheroids. Specifically, AERONET operational retrieval uses the concept by Dubovik et al. (2006) and models the particles for each size bin as mixture of spherical and non-spherical aerosol components. The non-spherical component was modelled by ensemble of randomly oriented spheroids (ellipsoids of revolution). The capacity of the non-spherical spheroid model to reproduce actual scattering properties of non-spherical dust has been validated against detailed laboratory polarimetric measurements of detailed phase matrices made by Volten et al. (2001) and spheroid shape distribution was tuned to reproduce closely those observations as described by Dubovik et al. (2006).

GRASP 3MI orbit simulation is based on GRASP/PARASOL aerosol and surface property climatology operating with assumption of aerosol using size distribution represented by 5 lognormal size bins. For 3MI measurements simulations over chosen AERONET stations, the ARERONET based aerosol models with 22 triangle bins are used.

2.2.4 GRASP PARASOL-based aerosol climatology for 3MI

Extended aerosol properties retrieved by GRASP from multi-spectral, photopolarimetric POLDER/PARASOL measurements provides possibilities of aerosol type classification and aerosol sources identification.

Figure 2.8 and 2.9 show climatological (Summer, 2008) complex refractive index at 670 nm, aerosol non-sphericity and aerosol vertical profile parameter retrieved by GRASP algorithm from PARASOL. An example of AOD and SSA calculation is shown in Fig. 2.10.

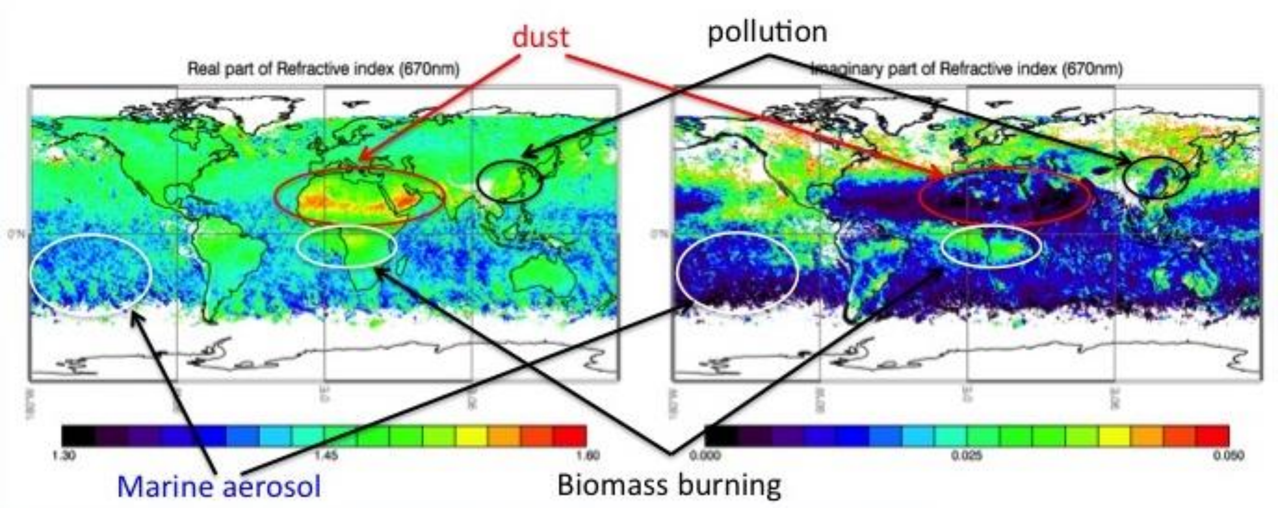

Figure 2.8 GRASP/PARASOL climatology. Complex refractive index map. Summer, 2008. Left panel: real part of the refractive index. Right panel: imaginary part of the refractive index.

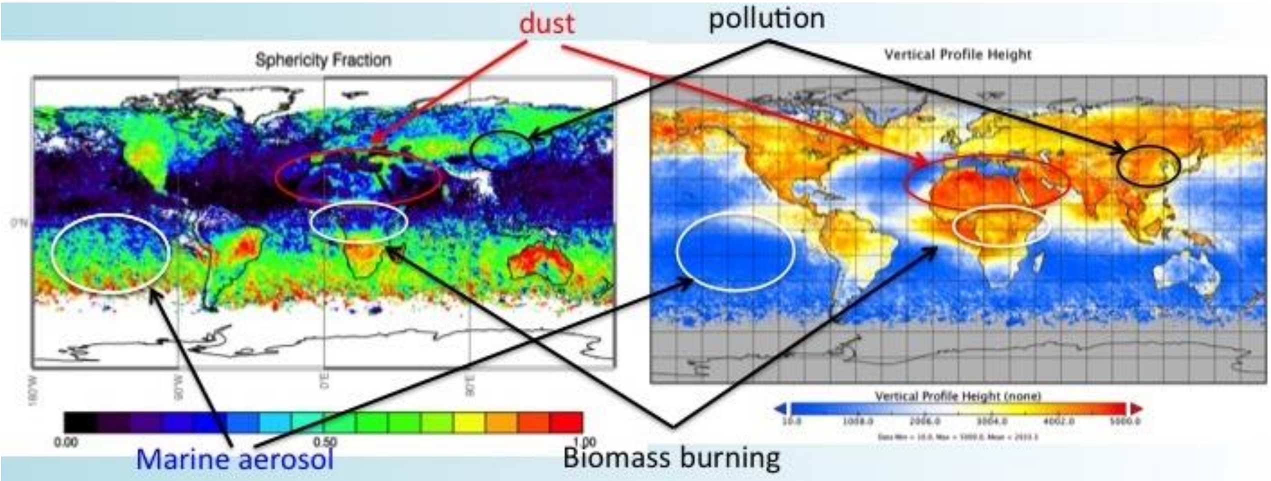

Figure 2.9 GRASP/PARASOL climatology. Sphere fraction vertical profile parameter. Summer, 2008.

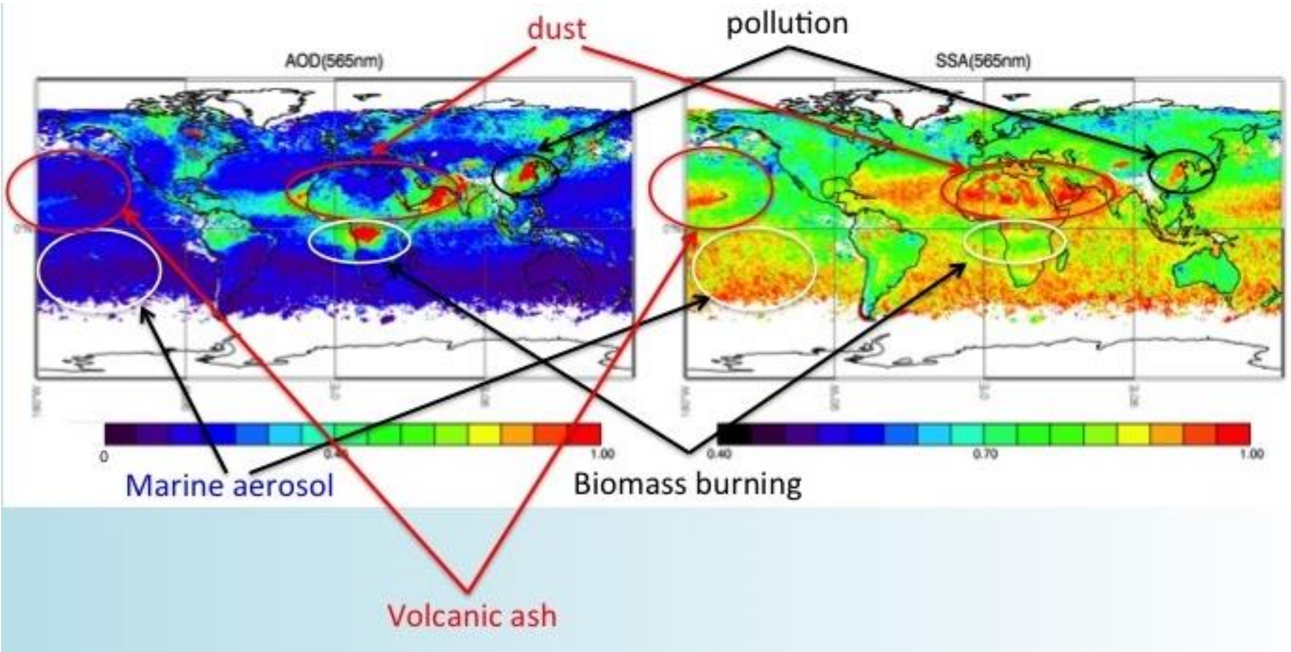

Figure 2.10 GRASP/PARASOL climatology. Example of AOD and SSA calculations.

The GRASP/PARASOL climatology presented in Fig. 2.8-2.10 or similar can be used as input for GRASP forward calculations to simulate observation orbits of 3MI measurements. In such aerosol climatology the only wavelength dependent parameter is the complex refractive index (Fig. 2.8). For this parameter the interpolation and extrapolation to 3MI channels can be performed in the way described in the Section 2.2.2 (Eqs.(2.1)-(2.3).

2.2.5 GRASP AERONET-based aerosol climatology for 3MI

AERONET provides extended and accurate aerosol parameters: multispectral AOD, SSA, Angstrom exponent, complex refractive index, size distribution etc. This extended aerosol characterization is extremely useful both for validation and synthetic data simulation.

The following AERONET sites were chosen to create AERONET-based aerosol climatology for 3MI top-of-atmosphere synthetic data simulation: (i) Banizoumbou/Niger AERONET site, (ii) Mongu/Zambia, (iii) Beijing/China, (iv) Kanpur/India, (v) Forth_Crete. These sites correspond to very different eco-systems with different types of aerosols and surface reflectance (see Table 2.5). Banizoumbou site has been chosen for the analysis because of frequent presence of desert dust outbreaks. Mongu region represents biomass burning aerosol domination in August and September. Beijing and Kanpur regions are ideal places for industrial pollution aerosol characterization. Maritime aerosol over Forth_Crete AERONET station can be a good reference for oceanic aerosol model evaluation.

Table 2.5 AERONET station for

Collocated AERONET site	Surface type	Aerosol type
Banizoumbou/Niger	Grassland	Dust
Mongu/Zambia	Savanna	Biomass burning/continental
Beijing/China	Urban	Industrial/dust
Kanpur/India	Urban	Industrial/dust/Continental polluted
Forth_Crete	Sea surface	Oceanic/dust

On the basis of the AERONET inversion and AOD measurements within 10 days during 2008, the synthetic measured data for 3MI over presented above stations were generated with GRASP.

2.2.6 GRASP surface climatology

Model for surface reflectance description

The Stokes parameters of scattered and incident radiation fields are related through 4x4 reflection matrix **R** (see, e.g., Mishchenko and Travis 1997):

$$\mathbf{I} = \frac{1}{\pi}\mathbf{R}(\lambda, \vartheta_v, \vartheta_0, \phi)\mathbf{I}_0(\lambda)\cos\vartheta_0. \qquad (2.4)$$

Here, $\mathbf{I} = (I, Q, U, V)^{\mathrm{T}}$ is the intensity column vector describing the radiance and polarization state of scattered radiation (T stands for "transposed"); $\mathbf{I}_0 = (I_0, Q_0, U_0, V_0)^{\mathrm{T}}$ is the Stokes vector, describing total and polarized incident irradiances; λ is the wavelength of the incident and scattered radiation; ϕ is the azimuth angle difference $\varphi_v - \varphi_0$, with φ_0 and φ_v being the solar and viewing azimuth angles, respectively; and ϑ_0 and ϑ_v are the solar and viewing zenith angles, respectively ($\vartheta_0 = \pi - \vartheta_{inc}$, ϑ_{inc} is the incident zenith angle).

For surface reflection description problem, the reflection matrix **R** corresponds to bidirectional reflection matrix (BRM). When the incident radiation is unpolarized, the surface reflection can be described with Bidirectional Reflectance Distribution Function (BRDF) and Bidirectional Polarization Distribution Function (BPDF) defined by the elements R_{11}, R_{21} and R_{31}:

$$BRDF = \frac{R_{11}}{p}, \quad BPDF = \frac{\sqrt{R_{21}^2 + R_{31}^2}}{p}. \qquad (2.5)$$

If single scattering by randomly oriented elementary surface (or volume) scattering elements gives the main contribution to the polarization of the scattered signal, then BRM has 2x2 block diagonal structure and the elements R_{21}, R_{31} are not independent of each other but related to polarized reflectance R_p via the following simple relations (Hovenier et al. 2004):

$$R_{21} = -R_p \cos 2\eta_v, \tag{2.6}$$

$$R_{31} = R_p \sin 2\eta_v, \tag{2.7}$$

where the dihedral angle η_v is the angle between the scattering plane (the plane containing the solar and viewing directions) and the meridional plane containing the zenith and viewing directions. It can be found, for example, from the equations

$$\cos\eta_v = -\frac{\cos\vartheta_0 + \cos\vartheta_v \cos\gamma}{\sin|\vartheta_v|\sin\gamma}, \qquad \sin\eta_v = \frac{\sin\vartheta_0 \sin\phi}{\sin\gamma}, \tag{2.8}$$

where γ is the scattering angle defined in the scattering plane, that

$$\cos\gamma = -\cos\vartheta_v \cos\vartheta_0 - \sin|\vartheta_v|\sin\vartheta_0 \cos\phi. \tag{2.9}$$

The relations (2.6) and (2.7) essentially simplify the surface reflection modelling. It was shown by Litvinov et al. (2010) that they hold for soil and vegetated surfaces measured with the airborne (Research Scanning Polarimeter (Cairns et al., 1999)) instrument.

Model for land surface reflectance description

For land surface reflection descript in 3MI synthetic measurements simulation, GRASP BRM is presented as the sum of the semi-empirical Ross-Li sparse BRDF models and the reflection matrix $\mathbf{R}_{Fr}$ based on semi-empirical Maignan-Breon BPDF (Bidirectional Polarization Distribution Function) models (Maignan et al., 2009; Litvinov et al., 2011a, 2011b, 2012):

$$\mathbf{R} = \begin{pmatrix} \mathrm{BRF} & 0 & 0 & 0 \\ 0 & 0 & 0 & 0 \\ 0 & 0 & 0 & 0 \\ 0 & 0 & 0 & 0 \end{pmatrix} + \mathbf{R}_{Fr}, \tag{2.10}$$

where BRF (Biderectional reflection Factor (Function)) is related to BRDF similarly Eq.(2.5): BRF=BRDF/π.

GRASP land BRM model for 3MI measurements simulation operates with 4 parameters: one scaling and two directional parameters of Ross-Li BRDF and one scaling parameter for Fresnel-based reflection matrix. All these parameters are allowed to change with wavelength but for the directional parameters and the scaling parameter for Fresnel-based reflection matrix the wavelength dependence is highly constrained. These strong constraints are based on previous studies from airborne measurements (Rondeaux and Herman 1991; Bréon et al. 1995; Cairns et al. 1999; Litvinov et al. 2010, 2011b).

The kernel-driven Ross-Li BRDF model uses a linear combination of three kernels f_{iso}, f_{vol}, and f_{geom} representing isotropic, volumetric, and geometric optics surface scattering, respectively (Roujean et al. 1992; Li and Strahler 1992; Wanner et al. 1995). According to [Litvinov et al. 2010, 2011] studies this model is renormalized as follows:

$$BRF_{RLi}(\lambda,\vartheta_v,\vartheta_0,\varphi) = k(\lambda)\Big(1 + k_1 f_{geom}\left(\vartheta_v,\vartheta_0,\varphi\right) + k_2 f_{vol}\left(\vartheta_v,\vartheta_0,\varphi\right)\Big), \quad (2.11)$$

$$f_{vol}\left(\vartheta_v,\vartheta_0,\varphi\right) = F_{HotS}(\gamma)\frac{\left(\pi/2-\gamma\right)\cos\gamma+\sin\gamma}{\cos\vartheta_v+\cos\vartheta_0}-\frac{\pi}{4} \quad (2.12)$$

$$f_{geom}\left(\vartheta_v,\vartheta_0,\varphi\right) = O\left(\vartheta_v,\vartheta_0,\varphi\right)-\sec\vartheta'_0-\sec\vartheta'_v+\frac{1}{2}\left(1-\cos\vartheta'\right)\sec\vartheta'_v\sec\vartheta'_0, \quad (2.13)$$

$$O=\frac{1}{\pi}\left(t-\sin t\right)\left(\sec\vartheta'_v+\sec\vartheta'_0\right), \quad (2.14)$$

$$\cos t=\frac{h}{b}\frac{\sqrt{D^2+\left(\tan\vartheta'_0\tan\vartheta'_v\sin\varphi\right)^2}}{\sec\vartheta'_v+\sec\vartheta'_0}, \quad (2.15)$$

$$D=\left[\tan^2\vartheta_1+\tan^2\vartheta_2-2\tan\vartheta_1\tan\vartheta_2\cos(\varphi_1-\varphi_2)\right]^{1/2}, \quad (2.16)$$

$$\cos\vartheta'=-\cos\vartheta'_v\cos\vartheta'_0-\sin\vartheta'_v\sin\vartheta'_0\cos\varphi, \quad (2.17)$$

$$\vartheta'_v=\tan^{-1}\left(\frac{b}{r}\tan\left|\vartheta_v\right|\right),\quad \vartheta'_0=\tan^{-1}\left(\frac{b}{r}\tan\left|\vartheta_0\right|\right). \quad (2.18)$$

$$F_{HotS}(\gamma)=1+\frac{1}{(1+\pi-\gamma)/\alpha_0},\quad \alpha_0=1.5. \quad (2.19)$$

BRDF=BRF/π; the term cos t in Eq. (2.15) is taken equal to 1 if $\left|\cos t\right|>1$. Kernels contain two parameters h/b and b/r (Wanner et al. 1995), which are fixed to $h/b=2$ and $b/r=1$ (Strahler et al. 1999).

The semi-empirical Maignan-Breon BPDF (Bidirectional Polarization Distribution Function) in GRASP is presented as follows (Maignan et al., 2009):

$$R_p(\vartheta_v,\vartheta_0,\varphi)=\alpha\frac{\exp(-\tan((\pi-\gamma)/2))F_p(m,\gamma)}{4(\cos\vartheta_0+\cos\vartheta_v)}. \quad (2.20)$$

Here $-F_p(m,\gamma)$, is the element F_{21} of the Fresnel scattering matrix, m is effective complex refractive index of land surfaces.

Model description of ocean/water surface reflectance

The seawater reflectance at short wavelengths is not negligible and depends on the properties of oceanic waters. The reflective properties of ocean surface are modeled analogously to the latest operational POLDER algorithm (Deuzé et al. 2001, Herman el al. 2005, Tanré et al. 2011) and (Mishchenko and Travis, 1997a, 1997b). The Fresnel's reflection from the sea surface is taken into account using the Cox and Munk model (Cox and Munk, 1954). The water leaving radiance is nearly isotropic (Voss et al., 2007) and is taken into account by Lambertian unpolarized reflectances a_0. Since part of water surface can be covered by foam, the fraction of surface d_{Fr} which provides Fresnel reflection is retrieved.

$$\mathbf{R} = d_{Fr}\frac{\mathbf{R}_{Fr}}{\mu_0\mu_v} f(\vartheta_v,\vartheta_0,\varphi;\sigma) + a_0(\lambda) \tag{2.21}$$

$$f(\vartheta_v,\vartheta_0,\varphi;\sigma) = \frac{1}{\pi\mu_n^4 2\sigma^2}\exp\left(-\frac{1-\mu_n^2}{\mu_n^2 2\sigma^2}\right) f_{shad}(\vartheta_v,\vartheta_0;\sigma), \tag{2.22}$$

$$\mu_n = \frac{n_v^z + n_0^z}{|\mathbf{n}_v + \mathbf{n}_0|}, \tag{2.23}$$

$$\mathbf{n}_0 = (\sin\vartheta_0\cos\phi_0;\ \sin\vartheta_0\sin\phi_0;\ \cos\vartheta_0), \tag{2.24}$$

$$\mathbf{n}_v = (\sin|\vartheta_v|\cos\phi_v;\ \sin|\vartheta_v|\sin\phi_v;\ \cos\vartheta_v), \tag{2.25}$$

where, $\mathbf{R}_{Fr}$ is the Fresnel reflection matrix (Mishchenko and Travis, 1997a); the function $f(\mathbf{n}_v,\mathbf{n}_0)$ describes the distribution of facets over orientation; σ^2 is the mean square facet slope; f_{sh} is a shadowing function for Gaussian surface (Mischenko and Travis, 1997a).

2.2.7 BRM climatology over land

Surface polarized reflectance

The results of GRASP global retrieval of polarization properties of land surfaces show essential global variation of surface polarized reflectance (Figure 2.11). For some land type surfaces polarized reflectance correlates with surface albedo and NDVI (Normalized Difference Vegetation Index) (Figure 2.12) but in the most cases GRASP shows independence of surface polarization of any other surface characteristics.

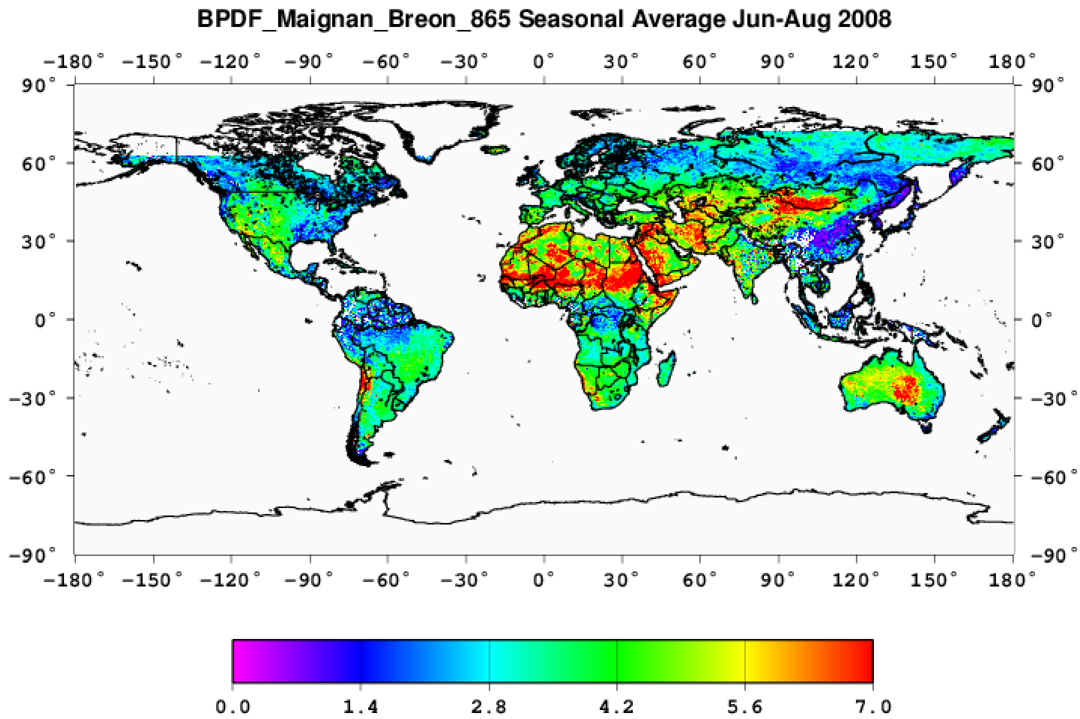

Figure 2.11 Global distribution of the polarization parameter of Maignan-Breon (Maignan et al. (2009)) BPDF model (865 nm).

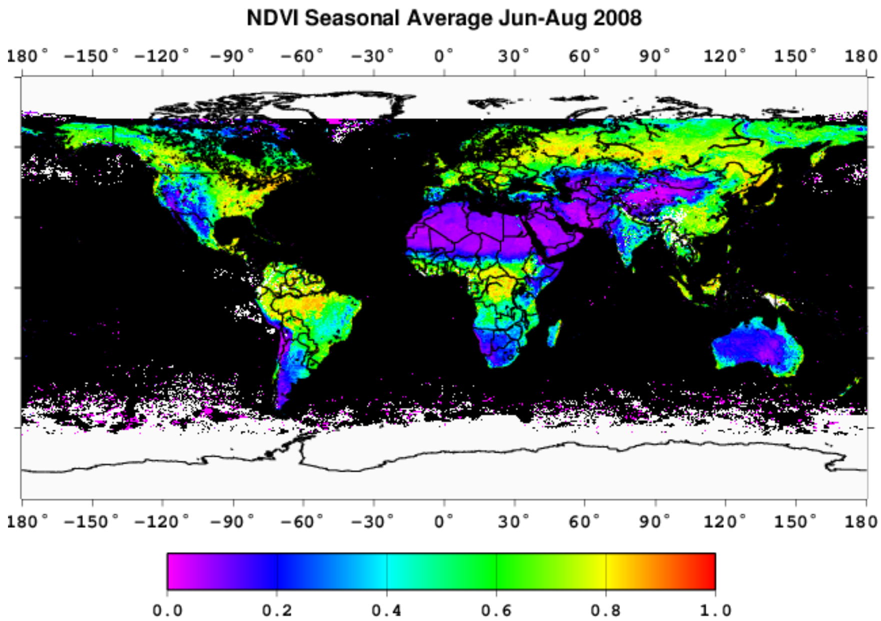

Figure 2.12 GARSP/PARASOL NDVI global map.

Weak wavelength dependence of the surface polarization was shown on airborne measurements in (Rondeaux and Herman 1991; Bréon et al. 1995; Cairns et al. 1999). It may be important to take into account when the aerosol optical thickness is small $(t_{aer} < 0.1)$ (Litvinov et al. 2010, 2011a,b). For larger values $(\tau_{aer} > 0.1)$, one can neglect the spectral dependence of the surface polarized reflectance. The slight spectral dependence of the surface polarized reflectance has already been utilized in aerosol-retrieval algorithms over land (Deuzé et al. 2001; Dubovik et al. 2011, 2014).

The assumption of spectral neutrality of the polarized reflectance is utilized in creation of 3MI climatology based on GRASP/PARASOL retrieval. Here, due to spectral neutrality of land surface polarized reflectance, the value of polarization parameter retrieved from one PARASOL wavelength can be used for all 3MI channels.

Land surface BRDF: first BRDF parameter.

Unlike polarization, the surface total reflectance strongly depends on the wavelength. Moreover different surface types exhibit big variety of the reflectance spectral dependence. Here the simple interpolation/extrapolation from VIS and NIR channels to SWIR channels is not straightforward and requires surface type classification or combination of retrieval results from different instruments covering the spectral range of 3MI measurements.

GRASP approach for 3MI surface BRDF climatology is based on combination of GRASP/PARASOL and MODIS BRDF retrieval. In this approach the values of first (isotropic) parameters of BRDF in VIS and NIR 3MI channels (in the range 410 – 910 nm) are obtained from GRASP/PARASOL BRDF retrieval at similar wavelength or interpolation/extrapolation (in the range 443-1020 nm) using the approach described in the Section: Interpolation/extrapolation to 3MI channels (see Table 2.5 for details). The parameters for SWIR 3MI channels are obtained in the similar way but using MODIS BRDF spectral retrieval as a reference (see Table 2.6 for detailed description).

Table 2.6 GRASP/PARASOL BRDF and 3MI spectral channels

3MI wavelengths, nm	3MI climatology for first BRDF parameter
410	Extrapolation from GRASP/PARASOL BRDF at 443 and 490 nm
443	GRASP/PARASOL BRDF at 443 nm
490	GRASP/PARASOL BRDF at 490 nm
555	GRASP/PARASOL BRDF at 565 nm
670	GRASP/PARASOL BRDF at 670 nm
763	Interpolation from GRASP/PARASOL BRDF at 670 and 865 nm
765	Interpolation from GRASP/PARASOL BRDF at 670 and 865 nm
865	GRASP/PARASOL BRDF at 8650 nm
910	Interpolation from GRASP/PARASOL BRDF at 865 and 1020 nm
1370	Interpolation from MODIS BRDF at 1240 and 1640 nm
1650	MODIS BRDF at 1640 nm
2130	MODIS BRDF at 2120 nm

The consistency of this combined approach for surface BRDF climatology is assured by excellent correspondent of two independent BRDF retrieval (GRASP/PARASOL and MODIS) for commonwavelengths. Figure 2.13 show an example of global distribution of first BRDF parameter at 670 nm from GRASP/PARASOL and MODIS surface product (MCD43C1) and figure 2.14 presents pixel-to-pixel comparison of the two products.

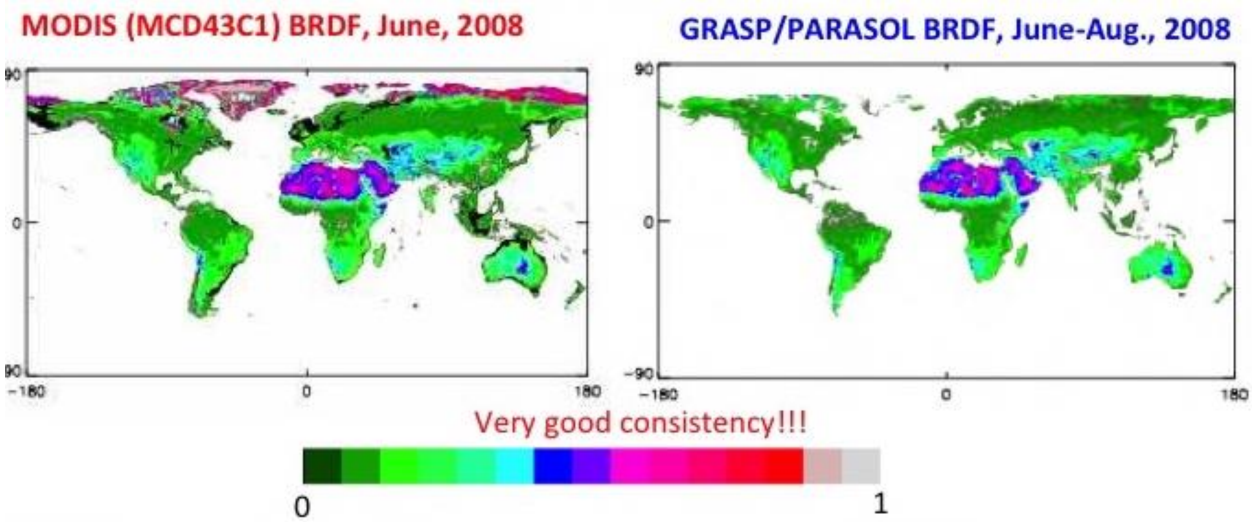

Figure 2.13 GRASP/PARASOL and MODIS BRDF climatology. 1st Ross-Li parameter, 670 nm.

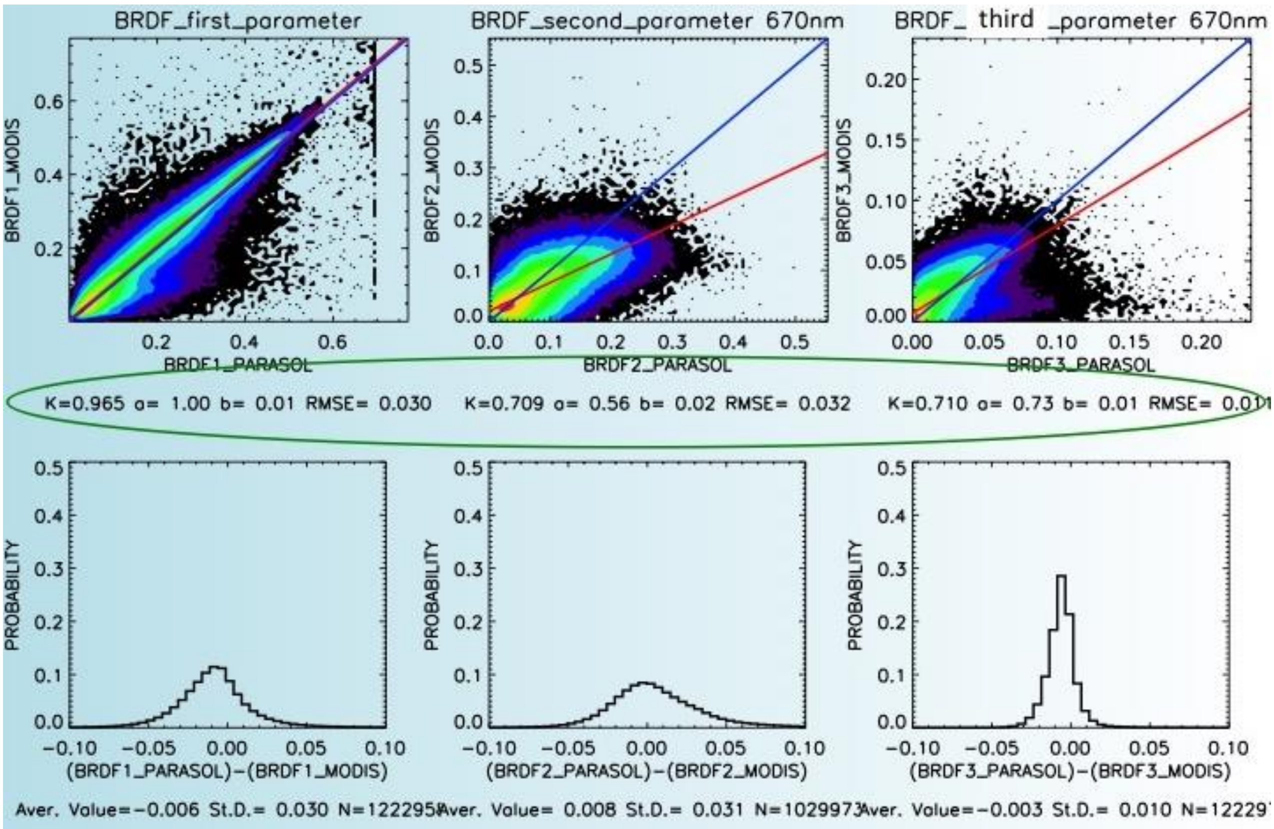

Figure 2.14 GRASP/PARASOL and MODIS BRDF pixel-to-pixel comparison for 670 nm.

Land surface BRDF: second and third renormalized BRDF parameters.

BRDF angular shape dependence on the wavelength was the subject of investigation in (Litvinov et al. 2010, 2011b). On the basis of analysis of RSP measurements over soil and vegetated surface it was shown that in the wide range of illumination and scattering geometries

BRDF shape can be considered as spectrally invariant. The spectral invariance of the geometry-dependent BRDF term has already been exploited in the aerosol retrieval algorithm over land developed for the Along Track Scanning Radiometer-2 (AATSR-2) instrument (Flowerdew and Haigh 1996; Veefkind et al. 1998) and discussed for use in the MISR algorithm (Diner et al. 2005, Kokhanovsky and de Leeuw 2009).

Being presented in the renormalized form (see Eq.(2.3.8)), renormalized BRDF second and third parameters can be considered as independent of the wavelength for wide range of illumination and observation geometries. Thus, GRASP/PARASOL renormalized second and third parameters retrieved for one of PARASOL wavelength are used in 3MI climatology for all wavelengths.

Examples of 3MI climatology for the second and third parameter for Summer, 2008 are shown on (Figs.(2.15) and (2.16)).

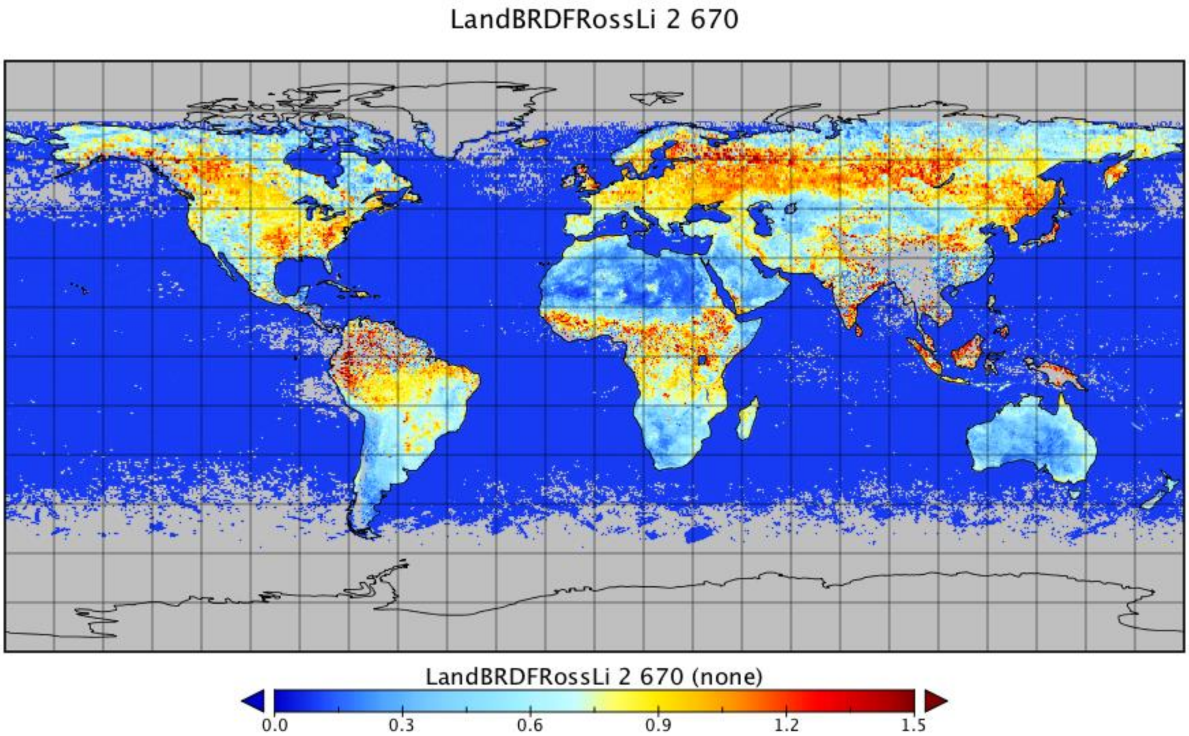

Figure 2.15 3MI BRDF second parameter climatology for Summer, 2008.

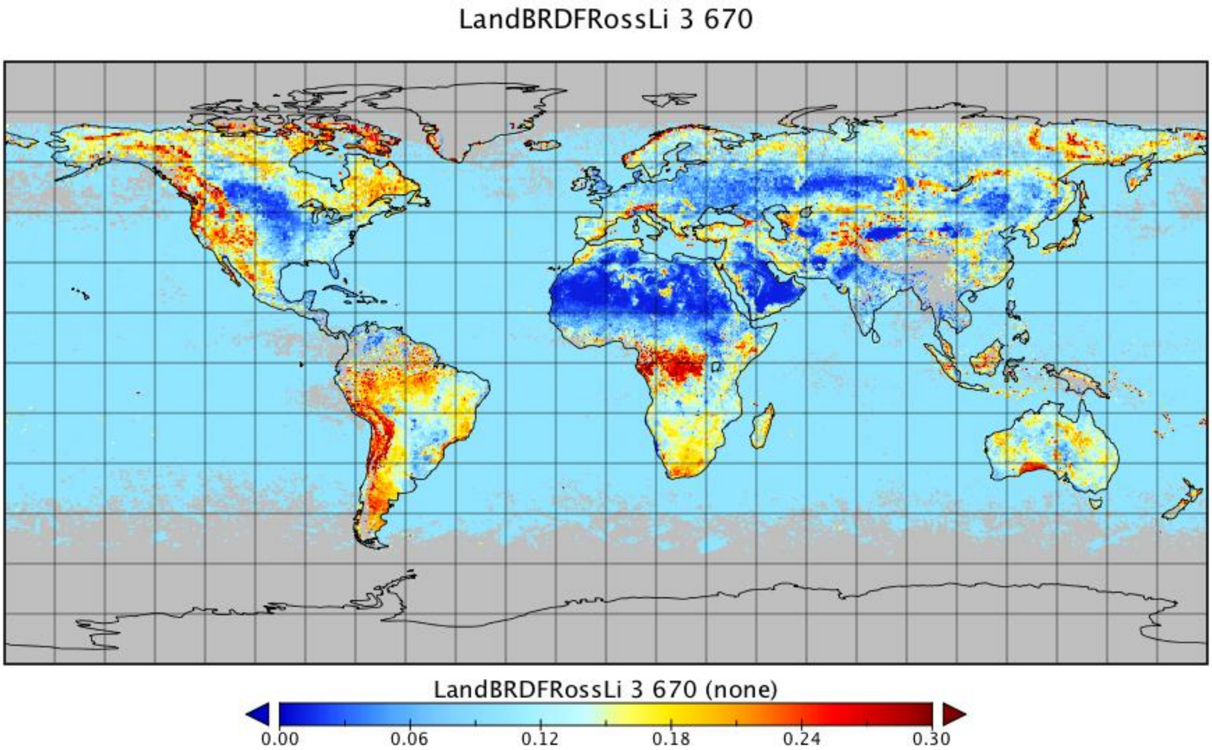

Figure 2.16 3MI BRDF third parameter climatology for Summer, 2008.

BRM climatology over water

GRASP BRM over ocean operates with three parameters (Eq.(2.11)): isotropic albedo of water body (a_0); the fraction of surface which provides Fresnel reflection $d_{Fr} = 1 - d_{foam}$, d_{foam} is foam fraction; and the mean square facet slope s^2, (for clean water $s^2 » 0.003 + 0.005W$, where W is a wind speed in (m/s)).

GRASP 3MI climatology for ocean/water BRM is generated from GRASP/PARASOL climatology with the following approach:

- The spectral dependence of the isotropic albedo of water body (parameter a_0) in 3MI range 410-865 nm is obtained from GRASP/PARASOL climatology interpolating/ extrapolating a_0 value from the range 443-1020 nm. For SWIR channels 1370, 1650, 2130 nm the water body albedo is considered to be zero ($a_0 = 0$)
- It is assumed that the whole ocean surface can provide Fresnel reflection ($d_{Fr} = 1$).
- The mean square facet slope (s^2) is wavelength independent and is taken from GRASP/PARASOL climatology.

Example of 3MI ocean climatology is presented in Figs. (2.17) and (2.18).

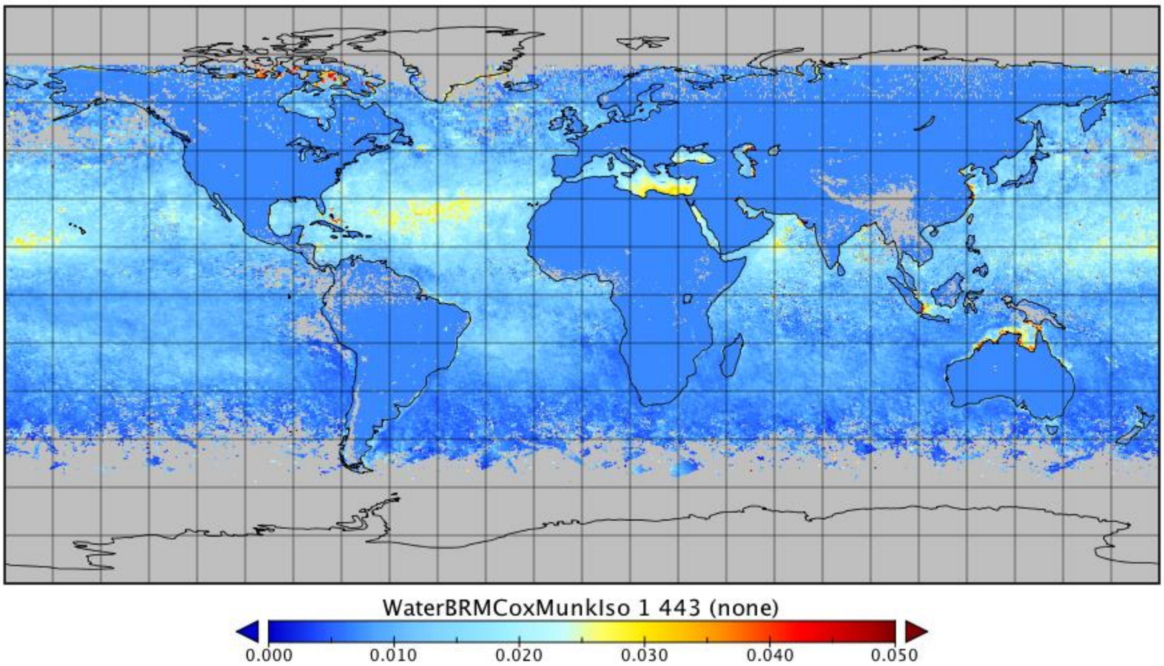

Figure 2.17 GRASP 3MI climatology for isotropic albedo of water body. Summer, 2008.

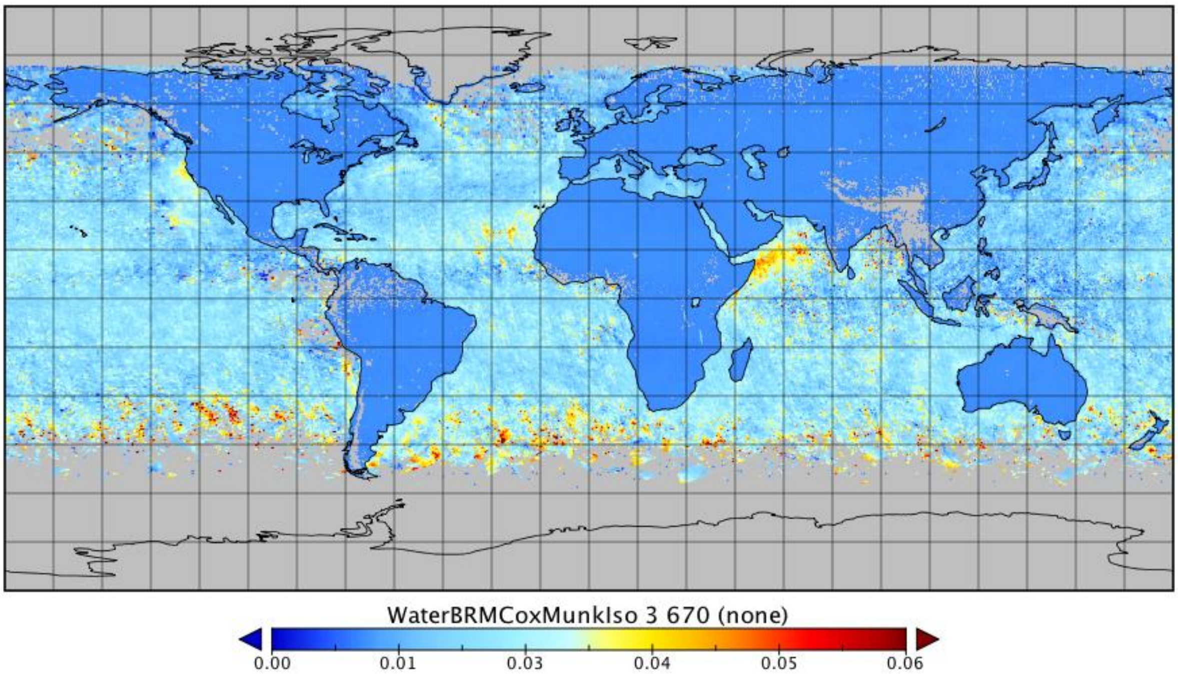

Figure 2.18 GRASP 3MI climatology for mean square facet slope. Summer, 2008.

2.2.8 GRASP 3MI L1C data simulation

Example of EUMETSAT L1C orbit simulation of the top-of-atmosphere reflectance is presented on Fig. 2.19. On the basis of described in the Sections 2 GRASP 3MI aerosol and surface climatology the top-of-atmosphere total and polarized reflectances were simulated for

EUMETSAT orbit. An example of the simulation is presented in Fig. 2.20. One can see similar surface reflectance on both figures but different aerosol properties and loading.

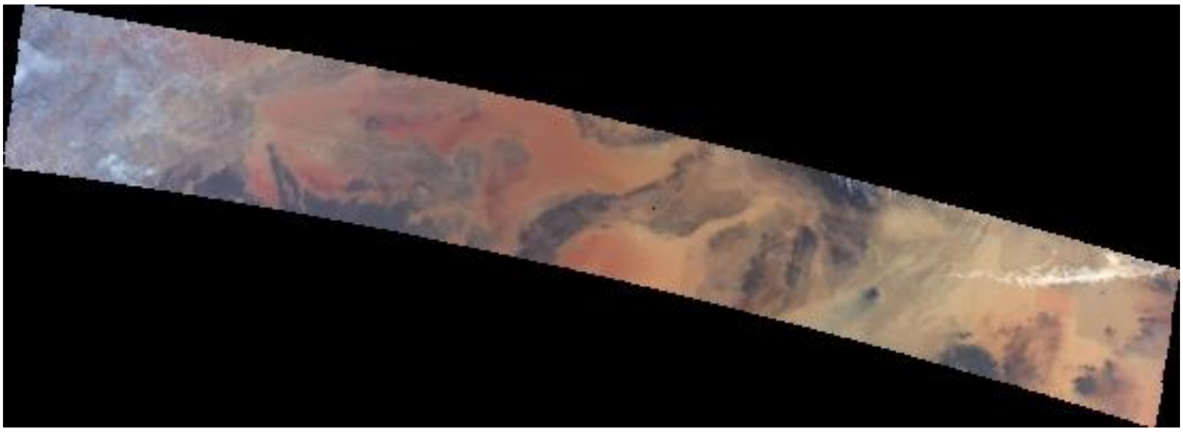

Figure 2.19 EUMETSAT L1C top-of-atmosphere total reflectance simulation over Libya.

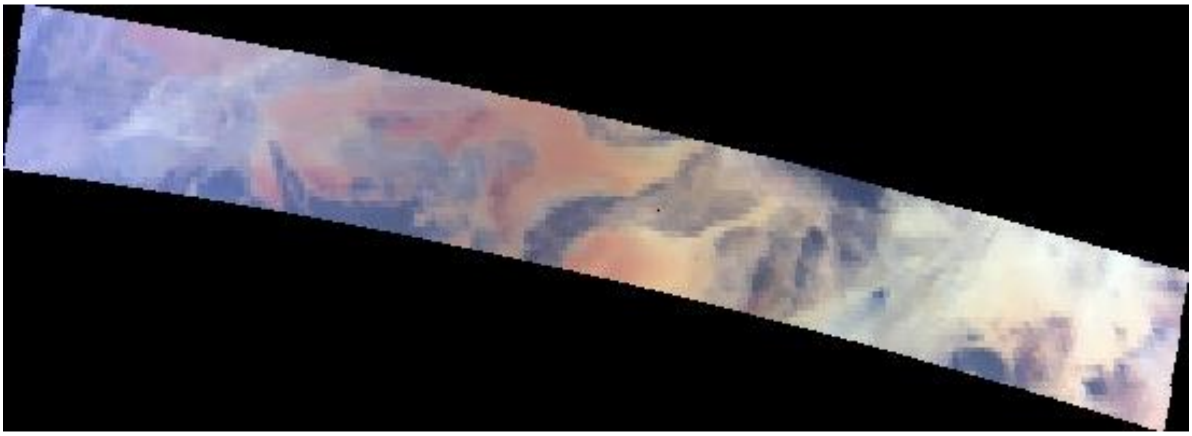

Figure 2.20 GRASP L1C top-of-atmosphere total reflectance simulation over Libya.

2.2.9 Summary of Task 2.2

On the basis of the prepared climatology and developed drivers GRASP 3MI synthetic measurements simulations were prepared for a 3MI orbit and over selected AERONET stations. The calculations are based on climatology of aerosol and surface properties retrieved from POLDER/PARASOL observations. For the spectral channels of 3MI that did not exist in POLDER/PARASOL observation, the aerosol properties such as complex refractive index were interpolated/extrapolated using known general physical tendencies (smooth monotonic variability over visible spectrum. For generating surface reflectance parameters at 3MI channel non-existent in POLDER/PARASOL, the climatology of PARASOL was complemented by observation of MODIS.

The climatological database of aerosol and surface was prepared, the necessary tools and approaches were developed and generalized so that the data can be easily used for simulation within any other specified 3MI orbit.

3. TASK 3: Testing of Baseline EUMETSAT Look-up-Table Algorithm.

After presentation and discussion of the results on the efforts to test LUT approach. It was decided that results are too questionable to be reported and further efforts on LUT approach were suspended in the project in the benefits of other activities. It also was suggested that some aspects of the verification of MARA algorithm performance can be revisited in future efforts. The decision was recorded in the minutes of ERA Progress Meeting 4 on October 17, 2017.

4. TASK 4: Proposal for Enhanced Aerosol Retrieval Algorithm

4.1 Objectives of Task 4 and overview of the efforts

The overall objective of this project is to propose state-of-art advanced algorithm for aerosol NRT retrieval from 3MI data. As defined in this project the objective the Task 4 is to suggest the specific algorithm and outline possible trade-offs of algorithm accuracy and speed. The main idea of this project is to propose the 3MI NRT algorithm based on the already extensively developed GRASP algorithm (Dubovik et al. [2014]). GRASP is a complex algorithm that have been realized in efficient computer routine, that has been applied to process entire data set of POLDER/PARASOL observations. The produced retrieval data provide extended set of aerosol parameters including size distribution parameters, spectrally dependent complex index of refraction, fraction of spherical particles, and aerosol height. The results for AOD (aerosol optical depth) and SSA (single scattering albedo) derived from PARASOL have been successfully validated against AERONET data (Popp et al. [2016]).

Thus, the intension of this project is to propose efficient for 3MI NRT retrieval based on GRASP development. The first step of such development is the adaptation of GRASP to 3MI NRT that includes two practical steps:

- adapting GRASP forward model to the specifications of 3MI observations;
- adapting inversion scheme of GRASO for NRT processing.

Once two of the above steps are realized the code then can be optimized with the objective of meeting the needs of achieving the speed requirements for processing of 3MI data.

4.2 Adaptation of GRASP to aerosol 3MI retrieval

The overall concept of 3MI sensor is very close to POLDER/PARASOL sensor, therefore the adjustments of forward model are rather straightforward, especially taking into account the flexible design of GRASP (Dubovik et al. [2014]). At the same time, GRASP uses elaborated multi-pixel scheme for using extra constraint on retrieval by using a priori limitation on time and space variability of the retrieved parameters (see Dubovik et al. [2011]).

Forward model adjustments

Figure 4.1 illustrates the input and output information for proposed 3MI NRT algorithm. As can be seen the algorithm uses all 3MI measurements in channels outside of the spectral range of strong absorption lines of atmospheric gases. The algorithm retrieves in overall more than 55 parameters including both parameters describing aerosol and surface reflectance. The details of the retrieval are provided in the submitted ATBD of the algorithm.

The main difference with the well-tested PAROSOL/GRASP version (Dubovik et al. [2011]) is the elimination of channel at 1020 nm and addition of new spectral channels at 410, 1650 and 2103 nm. Correspondingly, the spectral parameters (complex index of refraction, and parameters of BRDF and BPRF) have been changed. The model of size distribution, in principle, is spectrally independent, however it is necessary to verify if the chosen model is sufficient for providing adequate 3MI retrieval. Indeed, compared to POLDER/PRASOL 3MI has extra spectral channels and the measurement of polarization at each channel. These changes certainly improve sensitivity to different aerosol parameters including the size distribution. Correspondingly, it is necessary to check if the simplest size distribution model used by PARASOL/GRASP (5 log-normal bins) is sufficient or it needed to be modified by adding more complexities.

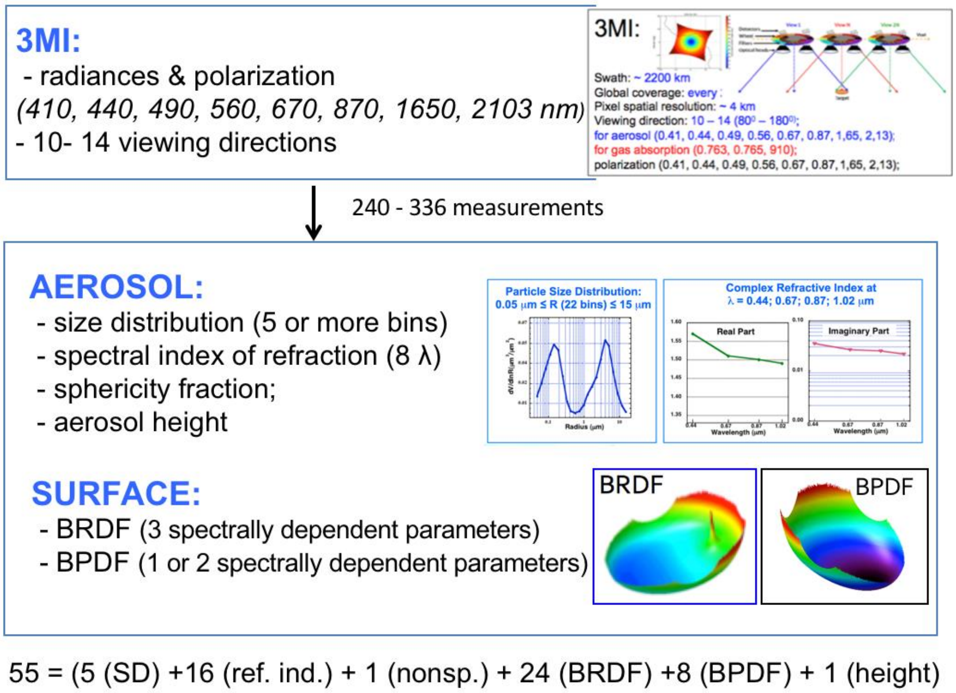

Figure 4.1 The input and output information for proposed 3MI NRT algorithm.

Multi-pixel inversion scheme adjustments

In reprocessing of POLDER/PARASOL archive by GRASP, the retrieval simultaneously used the data record of ~3 months over the same zone of 4 (2 by 2) or more pixels as illustrated by Fig. 4.2. The retrieval is implemented simultaneously using inter-pixel a priori constraints limiting time variability of the retrieved surface reflectance values and the spatial variability of aerosol parameters.

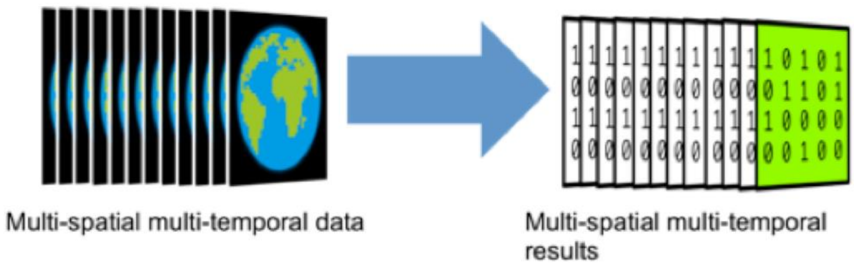

Figure 4.2 The illustration of multi-pixel PARASOL/GRASP retrieval approach

Obviously, such retrieval scheme is not acceptable for the requested NRT 3MI processing where observations over each orbit should be inverted separately. Nonetheless, "numerical inversion" module of GRASP is highly flexible and can be easily adapted for the need of NRT retrieval. Moreover, GRASP can be set up to realize adapted retrieval regimes that improve retrieval accuracy compare to conventional approaches. For example, in this study we plan to test 2 different retrieval regimes illustrated by Fig. 4.3:

A) ***Simple single-pixel retrieval*** (upper panel in Fig. 4.3). In this approach the inversion of observations of 3MI over each pixel are completely independent;

B) ***Spatial mingle-pixel retrieval under a priori constraints*** on surface reflectance (lower panel in Fig. 4.3. In this approach the temporal multi-pixel a priori constraints are reduced to the very simplified version when only a priori values surface reflectance from either retrieval in precedent time moment or the values of surface reflectance climatology are used for constraining surface retrieval. At the same time, if desired, a group of 3MI pixels from the same orbit inverted simultaneously under inter-pixel a priori constraints limiting the horizontal variability of aerosol parameters while keeping the retrieved surface reflectance parameters free of such constraints.

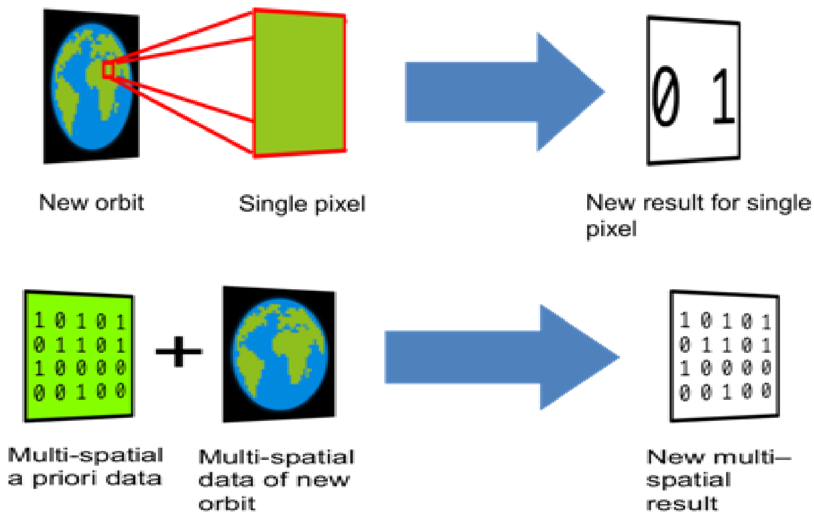

Figure 4.3 The illustration of possible modifications of the multi-pixel retrieval approach for 3MI NRT.

The approach **A)** is the simplest in the implementation, but it may face the difficulties to provide accurate aerosol retrieval in the challenging situations. For example, over bright surfaces where information content of observations regarding aerosol is very limited since the high surface reflectance suppresses the signal from aerosols. The approach **B)** addresses this challenge by using a priori constraints on surface reflectance. Indeed, it is well known, that in general land surface reflectance changes slowly in time and can be rather adequately predicted from available precedent observations or climatologies. This approach is used in the most of the satellite retrievals. In addition, this approach allows using a priori constraints on surface reflectance and constraints on spatial variability of aerosol properties.

The performances of both approaches have been tested and discussed in the following sections.

4.2.1 Testing the adjustments made for 3MI retrieval.

Size distribution assumptions effects

Figure 4.4 shows different representations of the size distributions that are implemented in GRASP:

(i) – Trapezium approximation (used in AERONET) that is suggested when detailed size distribtuion information can be retrieved;

(ii) – Approximation by set of log-normal bins (used in PARASOL retrieval) and recommended for situations when number of retrieved parameters should be decreased;

(iii) – Approximation by the bi-modal Log-normal distribution that is used in many satellite retrievals (e.g. Hasekampand Landgraf, [2007]).

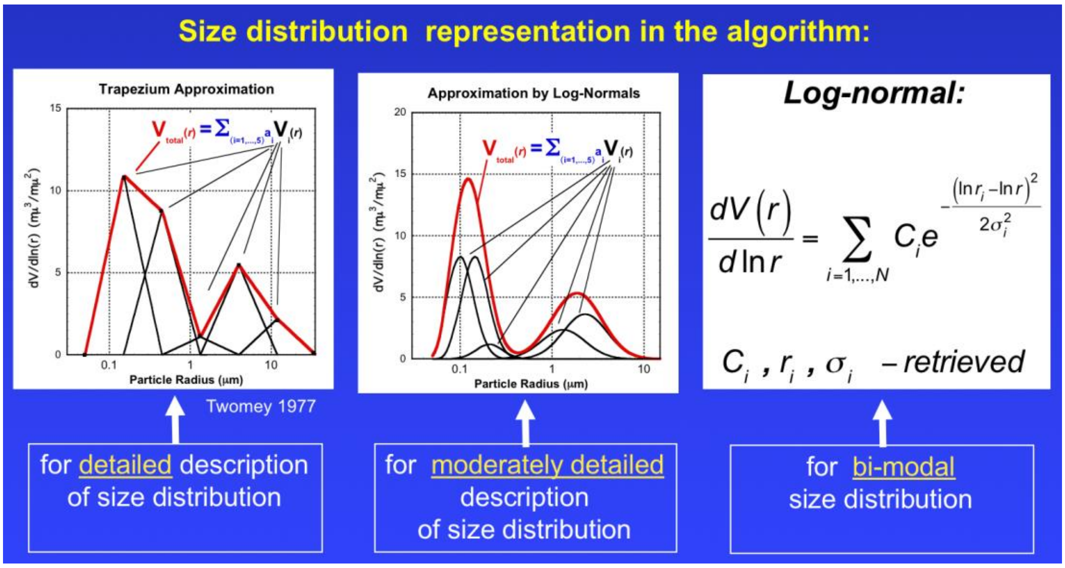

Figure 4.4 Illustration of the size distribution representations in GRASP algorithm.

In our algorithm, we suggest using 5 log-normal bins distribtuion annalogously with approach used in PARASOL/GRASP retrieval. This approch is attractive because 5 parameters is rather small in numbers that is very helpful for reducing the time required for the retrieval. The another possibility is using bi-log normal distribution approximation. This is most popular approximation for satellite retrievals, however using this approximation in GRASP takes significantly longer time. Both these assumptions were tested by applying GRASP retrieval to the "3MI data" simulated over AERONET sites in the Task 3. Specifically the retrievals were applied to the simmulations over Banizoumbou, Kanpur, Beijing, Mongu and Crete AERONET sites. It should be noted that the simulations were made using high quality settings, speifically it was used 22 bins in trapezoidal approximation for the size distribution as it is used for AERONET retrieval.

The tests were done for 2 diferent retrival scenarios: (A) single-pixel with no constaints on the surface variability and (B) multi-pixel when variability of surface was limited to be close to the ones observed easlier (previous retrieval or known from climatology).

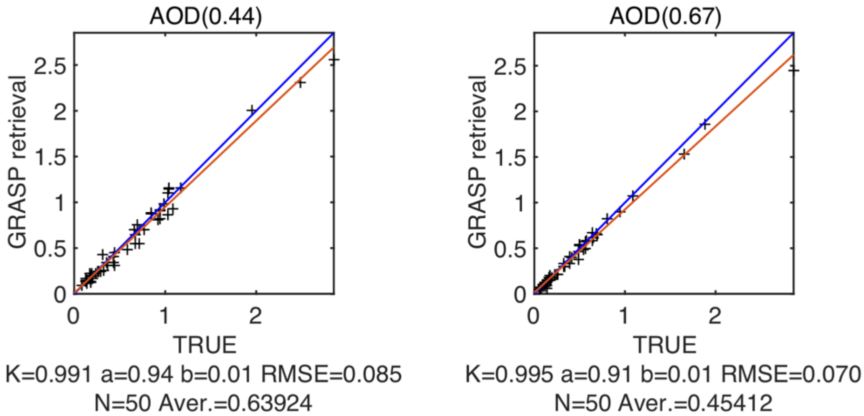

Figure 4.5 The illustration of AOD retrieval using GRASP based on 5 size bin size distribution model or single-pixel retrieval scenario.

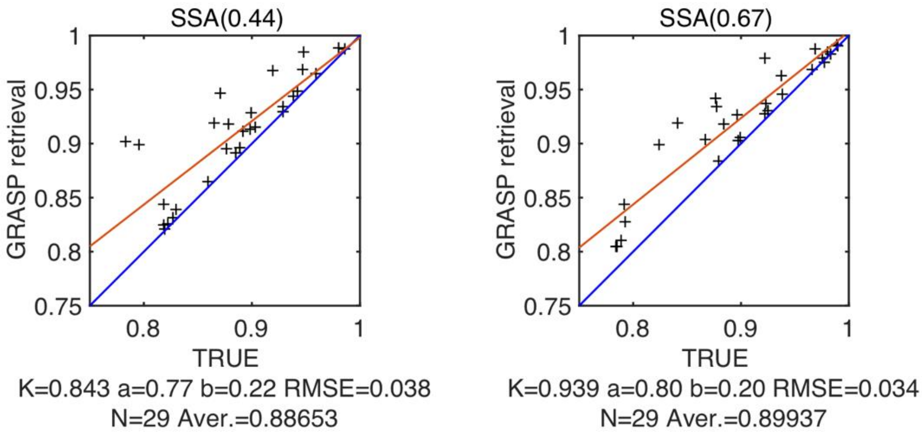

Figure 4.6 The illustration of SSA retrieval using GRASP based on 5 size bin model for single-pixel retrieval scenario (all points).

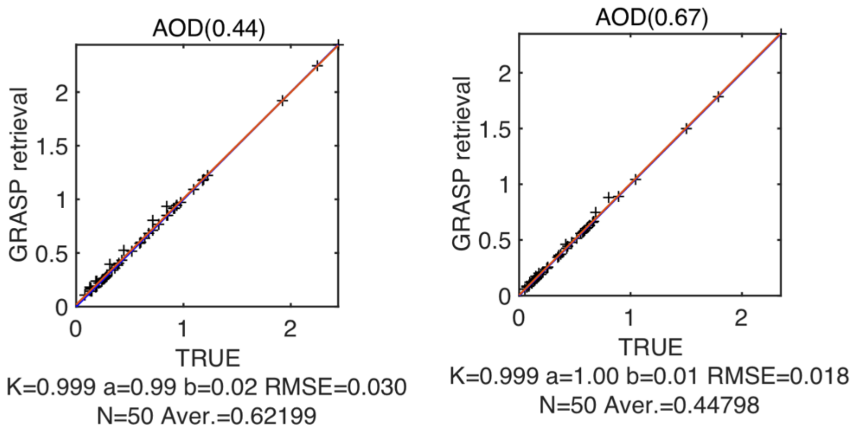

Figure 4.7 The illustration of AOD retrieval using GRASP based on 5 size bin size distribution model for multi-pixel retrieval scenario using a priori surface assumption.

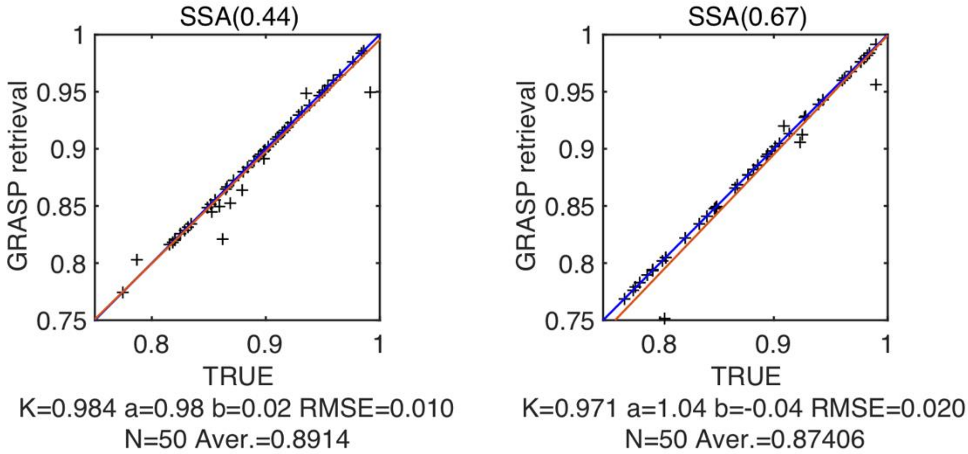

Figure 4.8 The illustration of SSA retrieval using GRASP based on 5 size bin size distribution model for multi-pixel retrieval scenario using a priori surface assumption (all points).

Figures 4.5-4.8 show the results obtained with GRASP code using assumption of 5 size bin size distribution model for 2 different retrieval scenarios. Figures 4.5-4.6 ullustrate the retrieval for single-pixel scenario and Figs. 4.7-4.8 for multi-pixel scenario using a priori constraints of surface reflectance values. It should be noted that these figures show only very few sellected of many but representative cases. Based on the obtained results, it is possible to conclude that using 5 size bin size distribution model provides rather satisfactory results for all parameters, in spite of the fact that that synthetic data is based on the 22 size binned real results of AERONET (that are in general even not lognormal). Comparing Figs. 4.5-4.6 and Figs. 4.7-4.8 we can see that using the a priori constraints on BRDF parameters helps notably to improve all retrieved aerosol parameters and especially SSA. At the same time, even single pixel scenario, when no temporary or spatial a priori constraints were used, provides higly satisfactory results that conform with EUMETSAT requirements.

Figures 4.9-4.10 provide the results for similar tests as those illustrated in Figs. 4.7-4.8 with the only difference that the results were obtained using bi-modal log-normal size distribution model. It should be noted that Fig. 4.10 shows only cases for AOD(440) > 0.2, i.e. low AOD cases with highest uncertainlty were filetered, while Fig. 4.8 shows all data points. Comparison of

Figs. 4.9-4.10 and Figs. 4.7-4.8 indicated that using simple 5 size bin size distribution model seems to provide more accurate results than using popular bi-modal log-normal size distribution model. In order to understand this observation, the retrival results were analyzed closely and Figs. 4.11-4.12 ullustrate the outcome of this analysis. It was found that apparently 5 size bin size distribution model reproduces better the actual AERONET size distribution than simmingly more rigorous bi-modal log-normal size distribution model. This can be seen from Fig. 4.11. Figure 4.12 show the differences in the retrieved spectal SSA, that overally retrieved better in the case of 5 bined size distribution. The figures show only one case (only one retrieval over Banizoumbou site), though this is just a represenative illustration from many analyzed samples.

Figures 4.11-4.12 demonstrate the fit of 3MI observations by algorithm using both size distribtuion models. It is clear from the figures that both models fit the observations with high accuracy, while 5 size bin size distribution model fits slighly better. Nonetheless, even such small deviations seem to have notable effect on the retrieval of such properties as SSA.

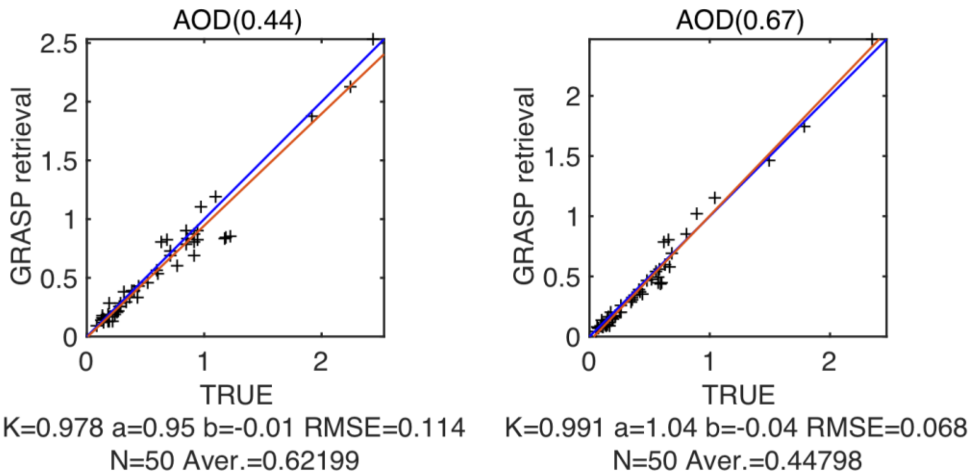

Figure 4.9 The illustration of AOD retrieval using GRASP based on bi-modal log-normal size distribution model for multi-pixel retrieval scenario using a priori surface assumption.

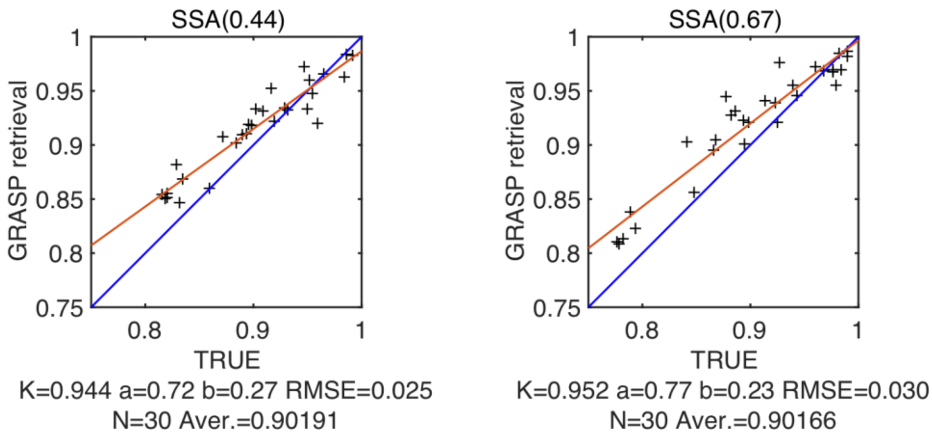

Figure 4.10 The illustration of SSA retrieval using GRASP based on bi-modal log-normal size distribution model for multi-pixel retrieval scenario using a priori surface assumption (AOD(440) > 0.2).

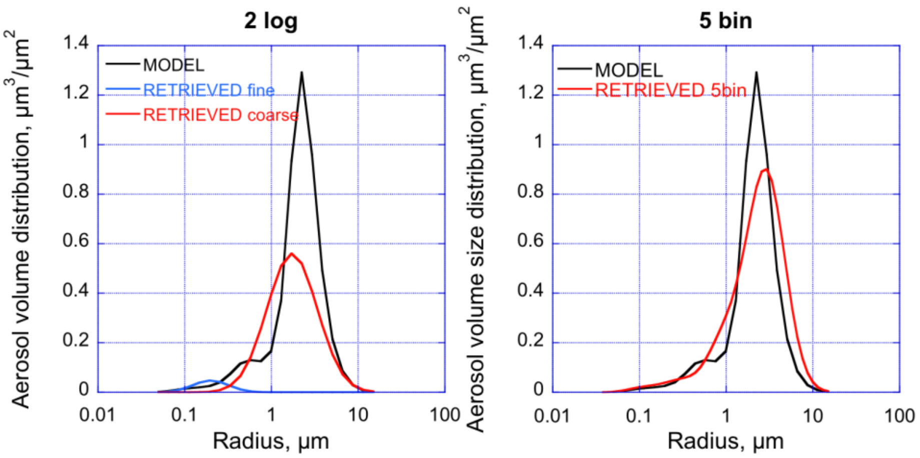

Figure 4.11 The illustration of comparison of size distribution retrieval using two different assumptions for size distribution (test for Banizoumbou site)

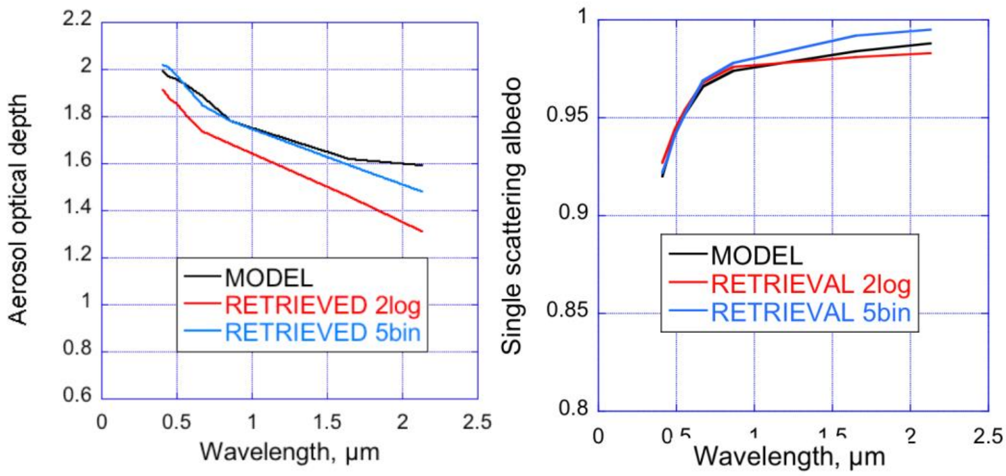

Figure 4.12 The illustration of comparison of SSA retrieval using two different assumptions for size distribution (test for Banizoumbou site)

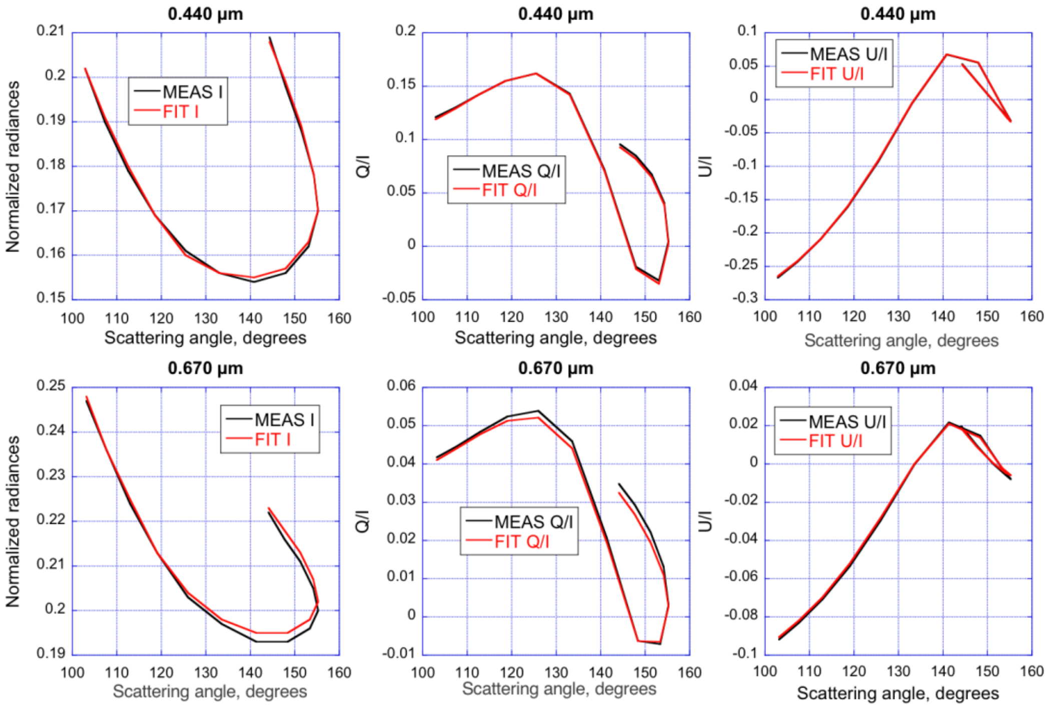

Figure 4.13 The illustration of 3MI measurement fitting for the retrievals illustrated in Figs. (4.6-4.7) for the retrieval based on assumption bi-modal log-normal size distribution.

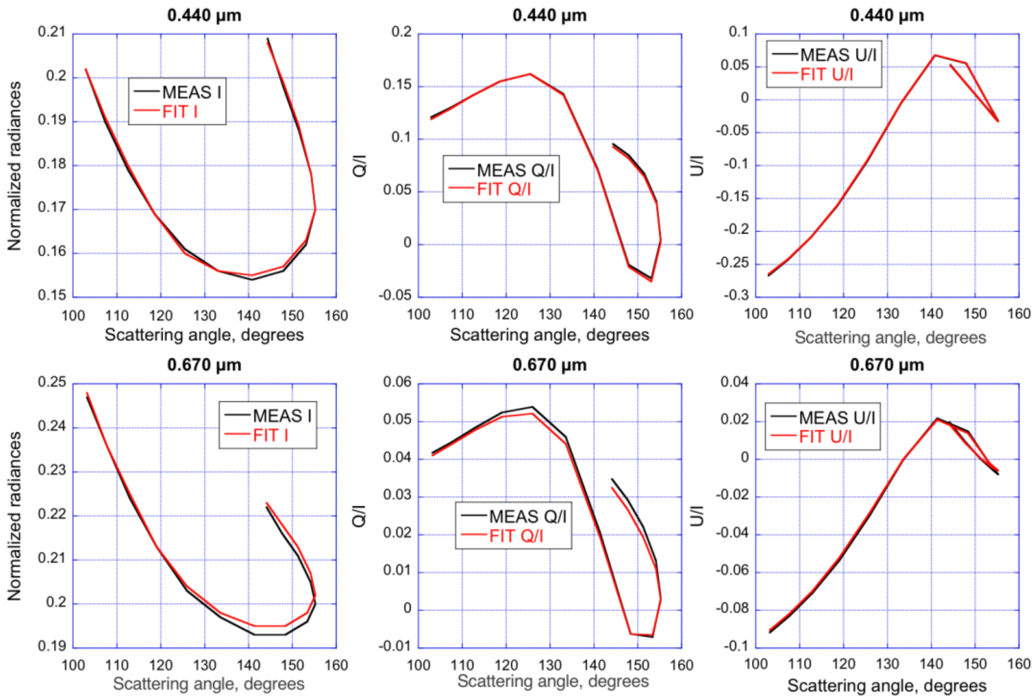

Figure 4.14 The illustration of 3MI measurement fitting for the retrievals illustrated in Figs. (4.6-4.7) for the retrieval based on assumption 5 size bin size distribution.

Multi-pixel set up of using surface update scheme

Figures 4.15-4.16 show the results of the tests on sensitivity of the retrieval to the error in a priori assumptions on the values of surface BRDF. Indeed, as was discussed in previous section, using a priori temporal constraints on variability of the surface BRDF improve the accuracy of the retrievals. At the same time, it is also clear that if the a priori values are different from real BRDF, such constraints may introduce biases that would limit the accuracy. In order to evaluate this effect, the tests were conducted where the error was introduced in the a priori BRDF parameters of the surface reflectance. Specifically, 5% bias was assumed in the BRDF. Since generally the surface reflectance is very stable in time, the daily variations of 5% can reproduce the actual uncertainty in surface reflectance a priori assumptions. As one can see from Fig. 4.15-4.16 such uncertainty doesn't affect significantly the retrieval. The only notable effect can be observed in the retrieved values of SSA.

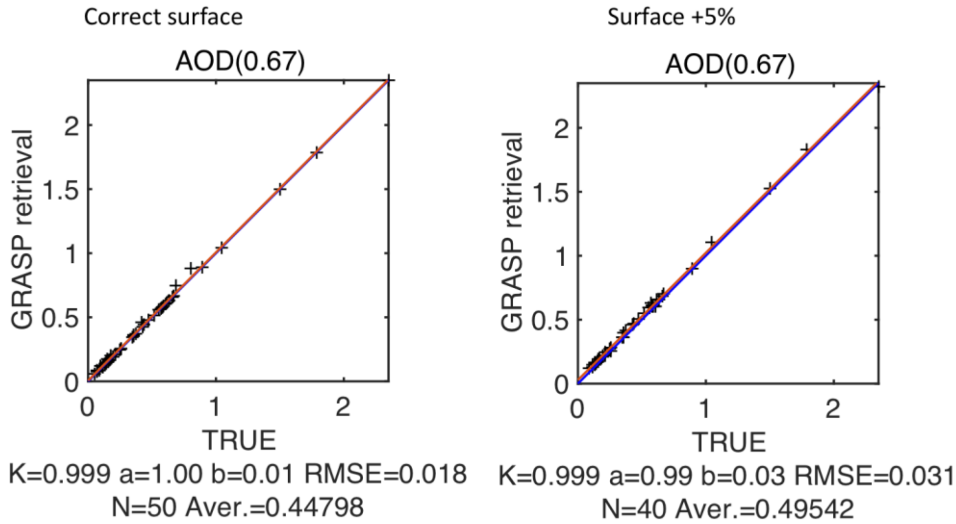

Figure 4.15 The illustration of AOD retrieval using GRASP based on 5 size bin size distribution model for multi-pixel retrieval scenario using a priori surface assumption. Demonstration of sensitivity to the errors in the a priori surface assumption.

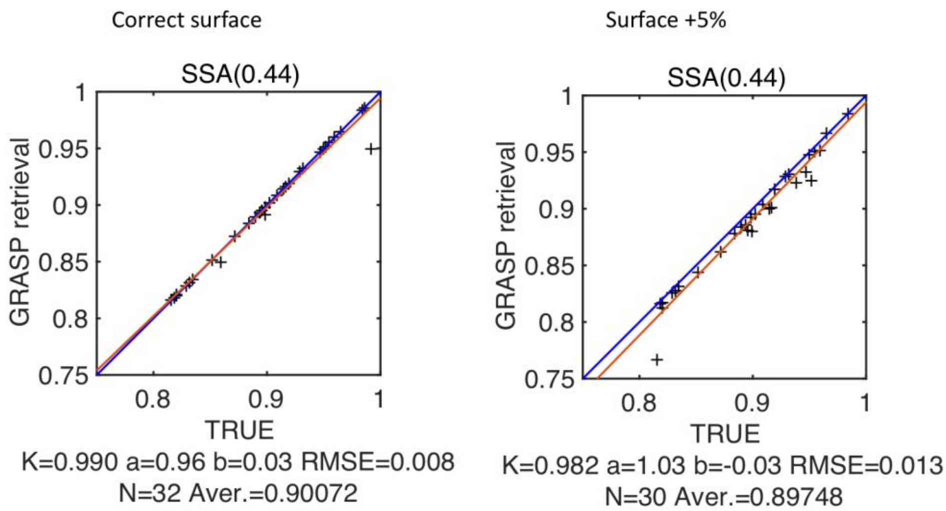

Figure 4.16 The illustration of SSA(440) retrieval using GRASP based on 5 size bin size distribution model for multi-pixel retrieval scenario using a priori surface assumption. Demonstration of sensitivity to the errors in the a priori surface assumption.

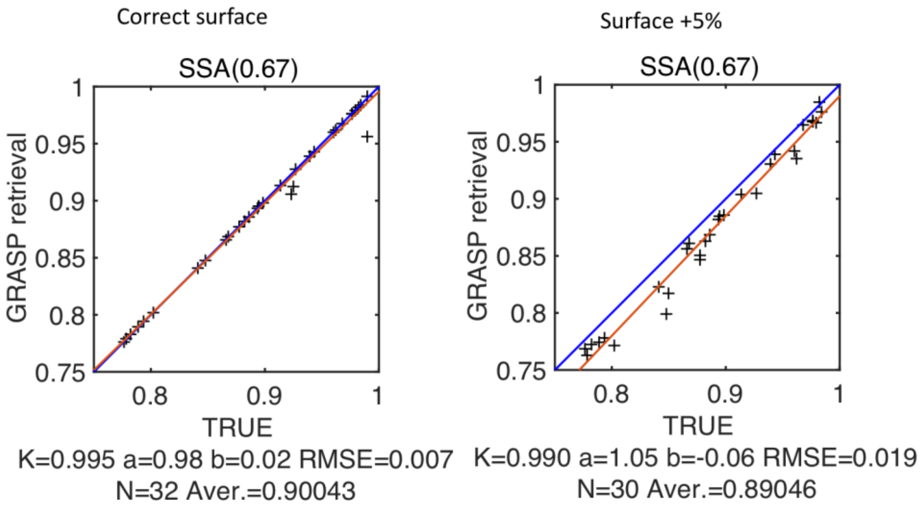

Figure 4.17 The illustration of SSA(670) retrieval using GRASP based on 5 size bin size distribution model for multi-pixel retrieval scenario using a priori surface assumption. Demonstration of sensitivity to the errors in the a priori surface assumption

4.2.2 Application of the algorithm to test data, speed verifications

Thus, as discussed in the previous sections, the 5 size bins size distribution model is sufficient to provide reliable retrieval of all derived parameters. Therefore this model is recommended for using 3MI NRT GRASP implementation. It should be noted that this model is using very small number of parameters to describe size distribution therefore it is the most appropriate for utilization in the fast algorithm aimed for NRT retrieval. Moreover as outlined in Dubovik et al. [2011], using bins instead of using directly analytical functions (e.g. log-normal distributions) helps significantly to save time by using pre-calculated kernels of single scattering properties suggested by Dubovik et al. [2006].

Therefore, 5 size bins size distribution model was implemented in 3MI NRT GRASP (see the ATBD) and the code was applied to the 3MI simulated observations based on climatologies of PARASOL and MODIS retrievals. The generation of these 3MI simulated observations was discussed in the details in the Task-3 section and is illustrated by Fig. 4.18.

Figures 4.19-4.21 demonstrate the results of applying 3MI NRT GRASP to the “one overlap” of 3MI simulated observations. As can be seen from the figures, the retrieval results reproduce assumed values quite accurate. This is not surprizing since the inverted 3MI simulations were produced fully consistent with the retrievals since they were produced using GRASP forward calculation module. At the same time, it should be noted that the illustrated inversions were done using single-pixel approach with minimum a priori assumptions.

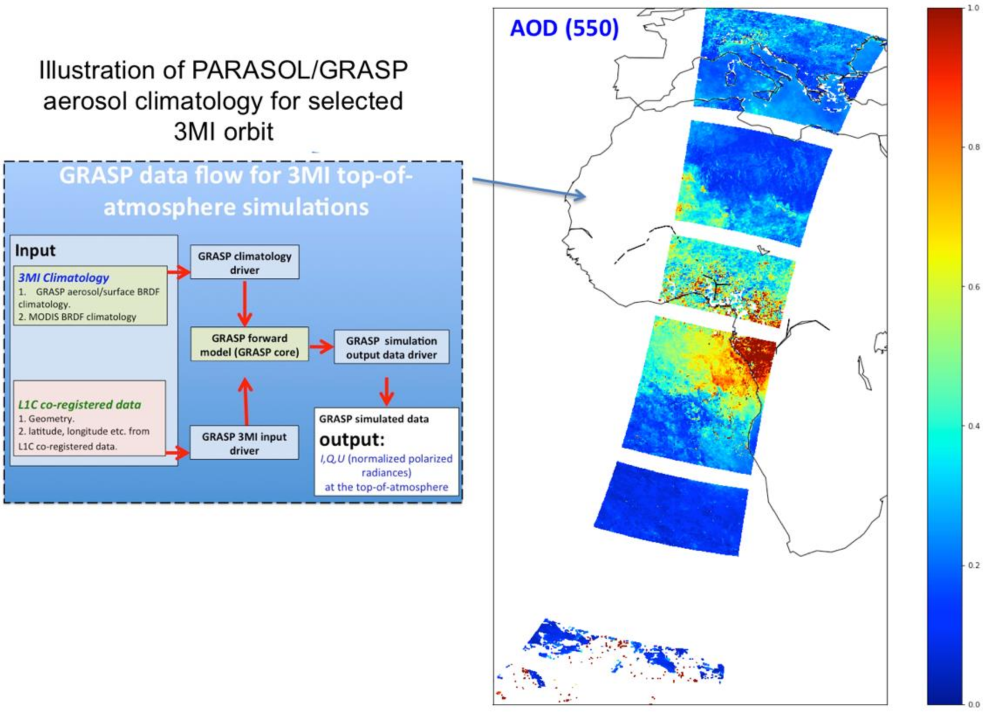

Figure 4.18 The illustration of the generation of 3MI synthetic data based on PARASOL and MODIS retrieval climatologies.

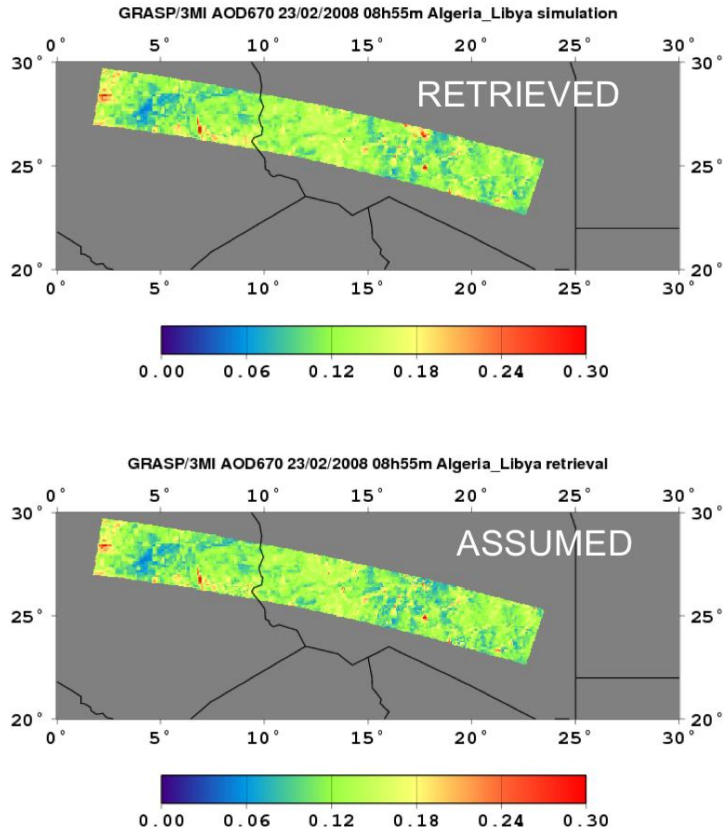

Figure 4.19 The illustration of the result of 3MI/GRASP inversion (single-pixel scenario) of 3MI synthetic data

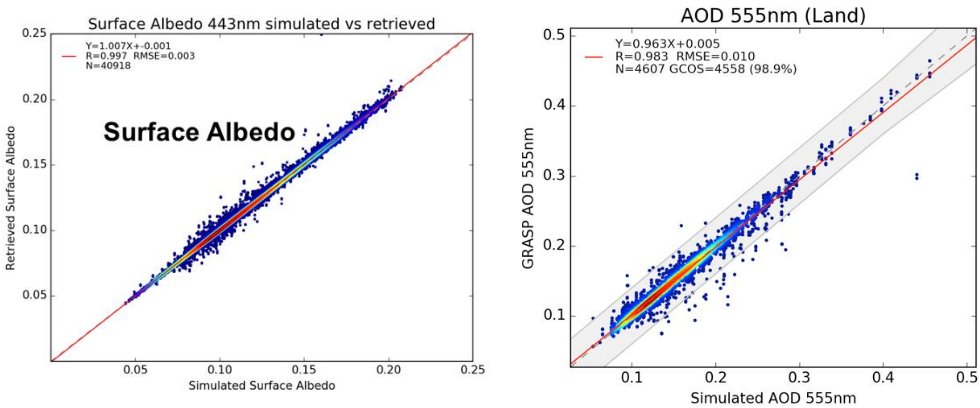

Figure 4.20 The illustration of the result of 3MI/GRASP inversion (single-pixel scenario) of 3MI synthetic data. The correlations of retrieved and assumed Surface Albedo and AOD.

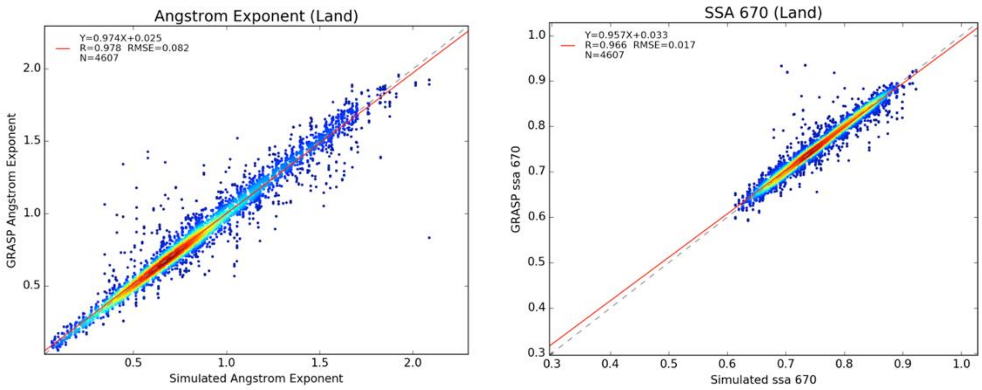

Figure 4.21 The illustration of the result of 3MI/GRASP inversion (single-pixel scenario) of 3MI synthetic data. The correlations of retrieved and assumed Angstrom Exponent and SSA.

4.2.3 Potential of further GRASP 3MI NRT algorithm acceleration

The tests shown in Section 4.2.2 were used to estimate the time performance of the 3MI NRT GRASP version. Based on the obtained results, the average time for 3MI inversion is ~ 0.5 sec per pixel. These results were obtained in the time for processing of one orbit of ~40 min using 100 cores computer cluster (assuming 50% cloud coverage).

It should be noted that the chosen versions of GRASP code seem to be the fastest for current GRASP code implementations. Other changes may require significant modifications. Indeed, the number of parameters for representing the size distribution is the minimum (further decrease may significantly decrease the accuracy), and the number of the retrieved spectral values for complex index of the refraction, BRDF and BPDF can't be decreased if all 3MI channels are inverted. Nonetheless, some practical trade-offs are possible that may change the scope of provided information but decrease the computational time. Moreover, based on the understanding of GRASP development team the accelerations of factor 4 may still be possible if some optimizations of radiative transfer calculations and IT structure of the code could be done. Here is the outline the potential 3MI NRT GRASP acceleration strategies:

- *Possible trade-offs in configuration:*
  - "not retrieving" surface (~ factor 2);
  - degrading accuracy (~ factor 2);
  - decreasing number of retrieved parameters (~ factor 2 at the maximum).

- *Evident practical trade-offs in configuration*:
  - not using all channels or polarization at all channels (~ factor 2 at the maximum);
  - decreasing spatial resolution to ~7 km (~ factor 4).

-Further sophisticated improvements (with no lose of accuracy);
  - RT calculation, etc. improvements (~ factor 2);
  - IT improvements of code implementation (~ factor 2).

4.3 Summary

Thus, in the frame of the Task 4 activities, 3MI NRT enhanced retrieval algorithm has been proposed. The algorithm is based on POLDER/GRASP developments. It uses all 3MI measurements in non-absorbing aerosol spectral channels of 3MI and derives simultaneously about 55 parameters of aerosol and surface. The algorithm has been realized; the details of the algorithm are described in the provided ATBD.

A series of numerical tests were conducted in order to verify the chosen assumptions for modelling aerosol and implementing retrieval. It was confirmed and illustrated that:

- using 5 size bin size distribution model is sufficient to provide reliable retrieval of all derived parameters;
- applying multi-pixel scenario utilizing priori constraints of surface reflectance values is improving the retrieval results compare to straightforward single pixel inversions.

A set of 3MI synthetic data was processed using recommended 3MI NRT GRASP configuration. The results demonstrated reliable retrieval of all retrieved parameters. The retrieval time records showed the 3MI NRT GRASP processing of one orbit by the realized base version can be estimated as ~40 min per orbit. Several potential trade-offs and code improvements have been outlined for discussion with EUMETSAT and follow on considerations.

5. TASK 5: Testing of Enhanced NRT Aerosol Retrieval Algorithm

5.1 Objectives of Task 5 and overview of the efforts

The objective of the Task 5 is to apply the algorithm with the settings selected in the Task 4 to the simulated 3MI data in order to demonstrate and verify the performance of the developed algorithm to the large amount of the data. Specifically, the algorithm has been applied to the "ideal" 3MI Level 1C Test **Synthetic Data Set** (generated by EUMETSAT) and to the Level 1C Test **Proxy Data Set** produced using PARASOL/GRASP and MODIS climatology., the detailed description of the data was provided in the Task 2 section.

During the executions of tests, it was observed that processing times of Synthetic Data and Proxy Data Sets are very close. At the same time some differences in the assumptions in data generation and inconsistencies between radiative transfer implementation in EUMETSAT Synthetic Data Set and GRASP retrieval were observed. Those differences and inconsistencies resulted to the fact that accuracy of data retrieval provided by GRASP code was notably lower in application to **Synthetic Data Set** compare to results from Test **Proxy Data Set** (where forward calculations and inversions were fully consistent). Therefore, the trade-offs between speed of processing and resulting accuracy were evaluated only using **Proxy Data Set.** At the same time, a separate section was added in order to provide illustration of GRASP applications to EUMETSAT **Synthetic Data Set**, where the differences and inconsistencies where analyses and discussed.

5.2 Trade-off of retrieval speed and accuracy of applying GRASP to aerosol 3MI data

5.2.1 Trade-off of retrieval speed and accuracy by varying GRASP retrieval settings

Based on the recommendations made using the results of Task 4, the following four main retrieval GRASP modifications have been tested:

- "high performance" retrieval with no a priori information on surface reflectance (Case 1);
- "optimized" retrieval with no a priori information on surface reflectance (Case 2);
- "optimized" retrieval using a priori information on surface reflectance (Case 3);
- "model" based retrieval using a priori information on surface reflectance (Case 4).

The difference between high performance and optimized is the accuracy of used radiative transfer (RT) calculation. For high performance the most accurate RT calculations were used, while in the optimized retrieval the accuracy of RT calculations was set notably lower. For example, the number of terms M in the expansion of the truncated phase function and N in the Gaussian quadrature for azimuth integration was set to M=15 and N= 10 for calculating the fit to 3MI observations and M=10 and N= 5 – for calculating Jacobian matrices. In initial modelling calculation and in "high performance" retrieval these numbers M and N are notably higher. Based on our estimations the drop in RT calculations accuracy allowed the reduction of speed by factor ~4.

When no a priori about surface reflectance is used the retrieval for all pixels is started with the same initial guess for surface reflectance (BRDF), the land/ocean mask was the only a priori information employed. Certainly, the initial guess values were different for land and ocean surface reflectance parameters. The detailed description of the employed BRDF parameters was provided in the Task 2 section. The described retrieval is aimed at the most general unbiased satellite retrieval and it was used for GRASP/PARASOL processing. However, that processing was not Near-Real-Time (NRT) and it was based on 3 months multi-pixel inversion concept (see Dubovik et al, 2011) that uses temporal constraints on surface reflectance variability helping to separate contribution of surface and aerosol. Such strategy is difficult to use in NRT retrieval, therefore a retrieval that uses a priori estimate of surface reflectance was suggested. Such strategy is well justified because reflectance of land surface (the most challenging for retrieval) is rather stable and general climatology gives rather accurate information on land BRDF in most of situations.

The high performance and optimized retrievals derive separately aerosol size distribution (assumed using 5 log-normal size bins, see Dubovik et al., 2011) and spectral complex index of refraction. In a contrast, "model based" retrieval derives the concentration of several assumed aerosol models. . In this approach, the aerosol is assumed as an external mixture of several aerosol components with assumed scattering and absorption properties. Then, only concentrations of the components were retrieved. This approach was not discussed in Task 4 because it is significantly less general. Nonetheless, it was added here since this approach has some promises in further reduction of the calculation speed. It is added here as "optional" for future research for possible consideration of EUMETSAT. The comparative results obtained using the above four retrievals are shown in figures 5.1–5.3. The presented retrievals shown for one the granule over Livia. This is one of the most difficult cases since the surface reflectance is very bright. It should be note, that, the retrieval for the Case 1 was performed for entire orbit, and it was observed that the performance of the retrieval per pixel did not differ significantly over , therefore the tests the performance analysis was done for one granule.

As one can see from Figs. (5.1–5.3), the four different retrieval scenarios provide retrievals of different qualities. Table 5.1 provides the summary of correlation parameters in comparisons of retrieved and assumed parameters, Table 5.1 provides summary of retrieval speed performances. To calculate the time required for processing one orbit of 3MI cloud-free observations composed of 44 granules (as it was in the Synthetic Data Set provided by EUMETSAT), it was assumed that one orbit contains ~ 500 000 cloud-free pixels and that processing could be done using a computer cluster of 100 cores. The object of the study in this Task 5 was to find the overall best trad-off between the speed and accuracy. The detailed analysis of each retrieval option performance in different surface areas and aerosol realization can be performed but it is out of present analysis.

Analysing the figures and the tables, one can see the expected overall tendency that the most complete and accurate retrieval that uses less assumptions corresponds to be the most time consuming version of retrieval. In sense of the best trade-off between accuracy and calculation speed, the retrieval implemented with optimized settings using a priori estimates for surface reflectance seems to be optimal. This version is rather fast (~20 min for the orbit) and provides accurate retrieval of the main aerosol parameters. Apparently, using a priori estimates on surface reflectance helps to achieve accurate retrieval even if less accurate RT is utilized.

The fastest version of GRASP retrieval is the one that used aerosol model based approach appears to provide significantly less accurate retrieval than the retrieval with optimized settings. At the same time, it should be noted that this approach is one of most promising for achieving further reduction of retrieval time, because some extra RT simplifications can be done. In addition, the performance of this approach can be further improved by tuning. For example, based on the experience of applying GRASP to PARASOL data, model based retrieval can give comparable and in some situation even more accurate retrievals than GRASP retrieval with optimized and high precision setting. Therefore, this approach is also proposed in this project for potential further consideration by EUMETSAT.

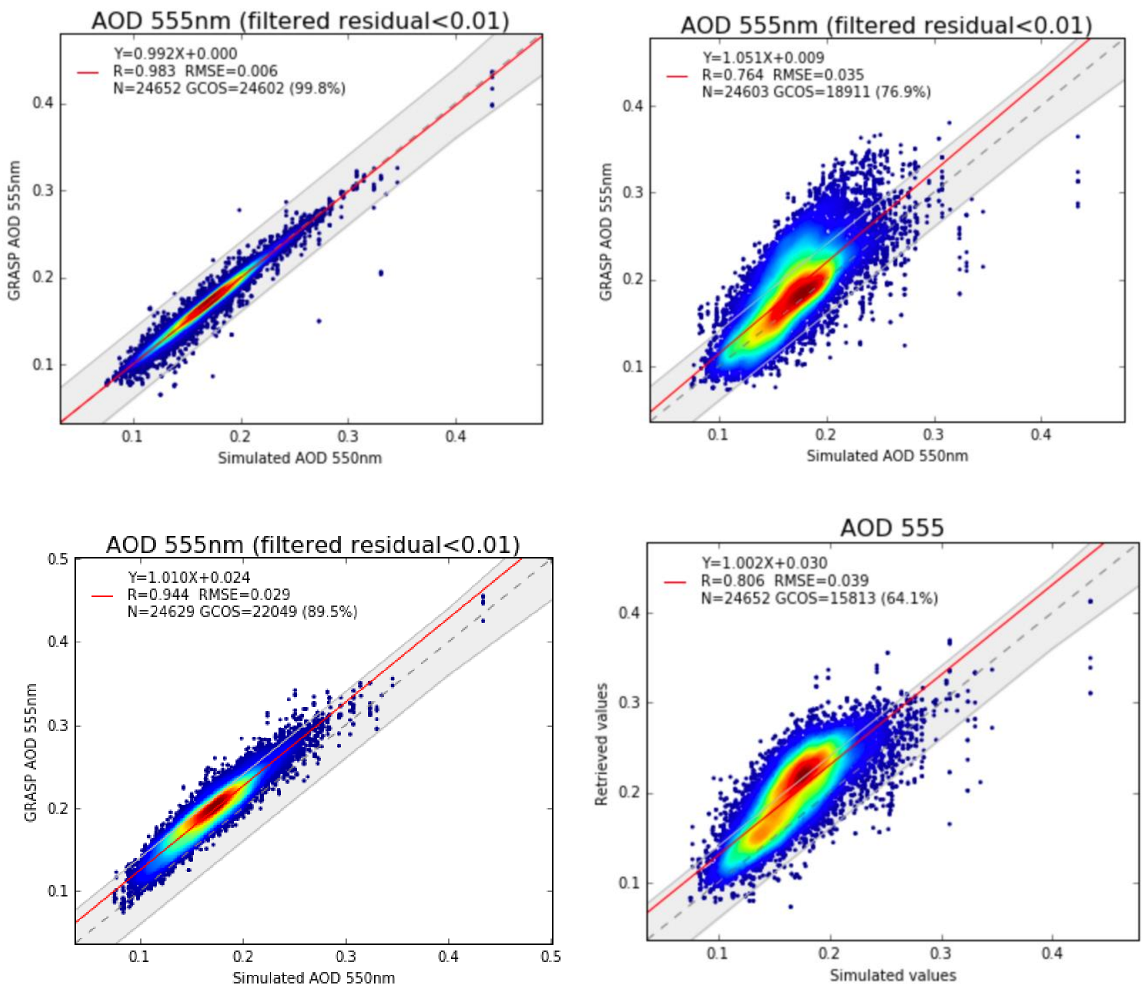

Figure 5.1 The illustration of 3MI Proxy data inverted with GRASP using different retrieval settings:

Upper panel:
-(left): *Case 1* - high performance retrieval with no a priori information on surface reflectance;
-(right): *Case 2* - optimized retrieval with no a priori information on surface reflectance;

Lower panel:

-(left): *Case 3*- optimized retrieval using a priori information on surface reflectance;

-(right): *Case 4* - model based retrieval using a priori information on surface reflectance.

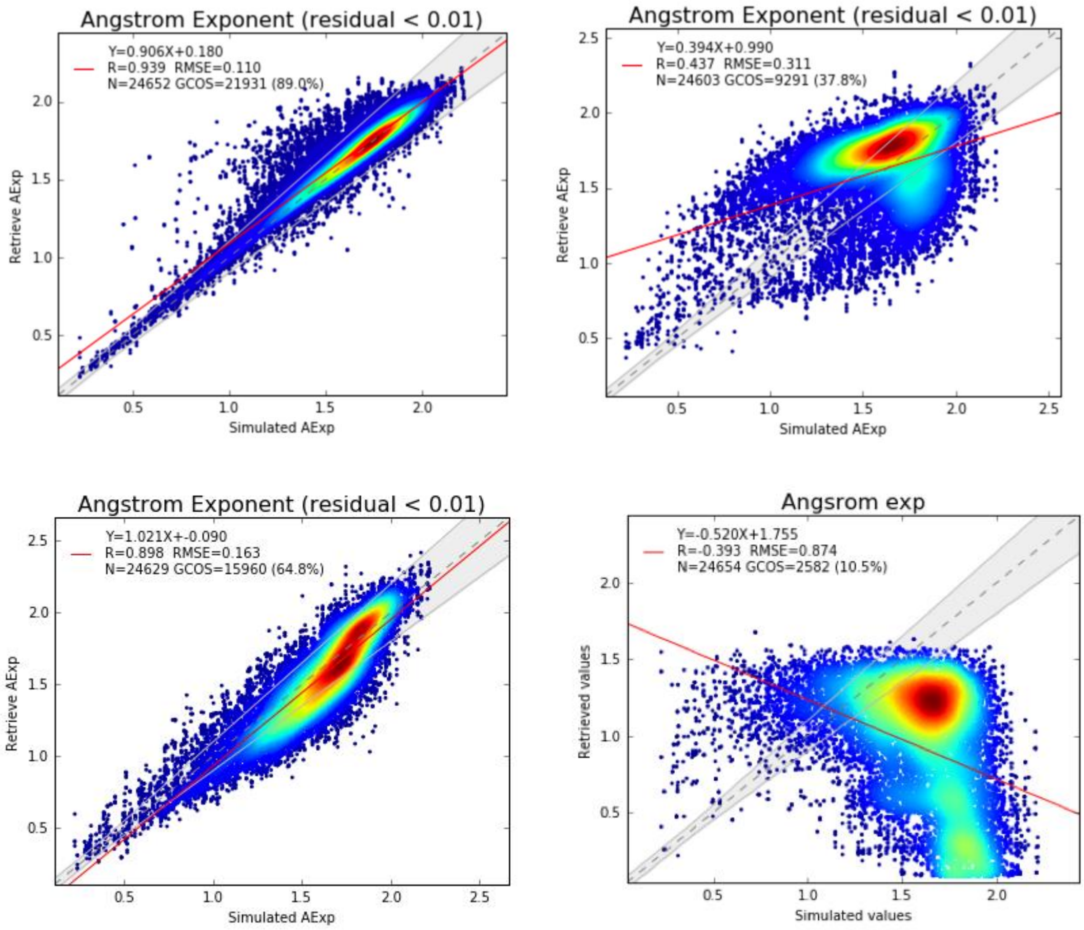

Figure 5.2. Angstrom exponent retrieval from 3MI Proxy data using GRASP with different retrieval settings:

Upper panel:

-(left): *Case 1* - high performance retrieval with no a priori information on surface reflectance;

-(right): *Case 2*- optimized retrieval with no a priori information on surface reflectance;

Lower panel:

-(left)): *Case 3* - optimized retrieval using a priori information on surface reflectance;

-(right): *Case 4* - model based retrieval using a priori information on surface reflectance.

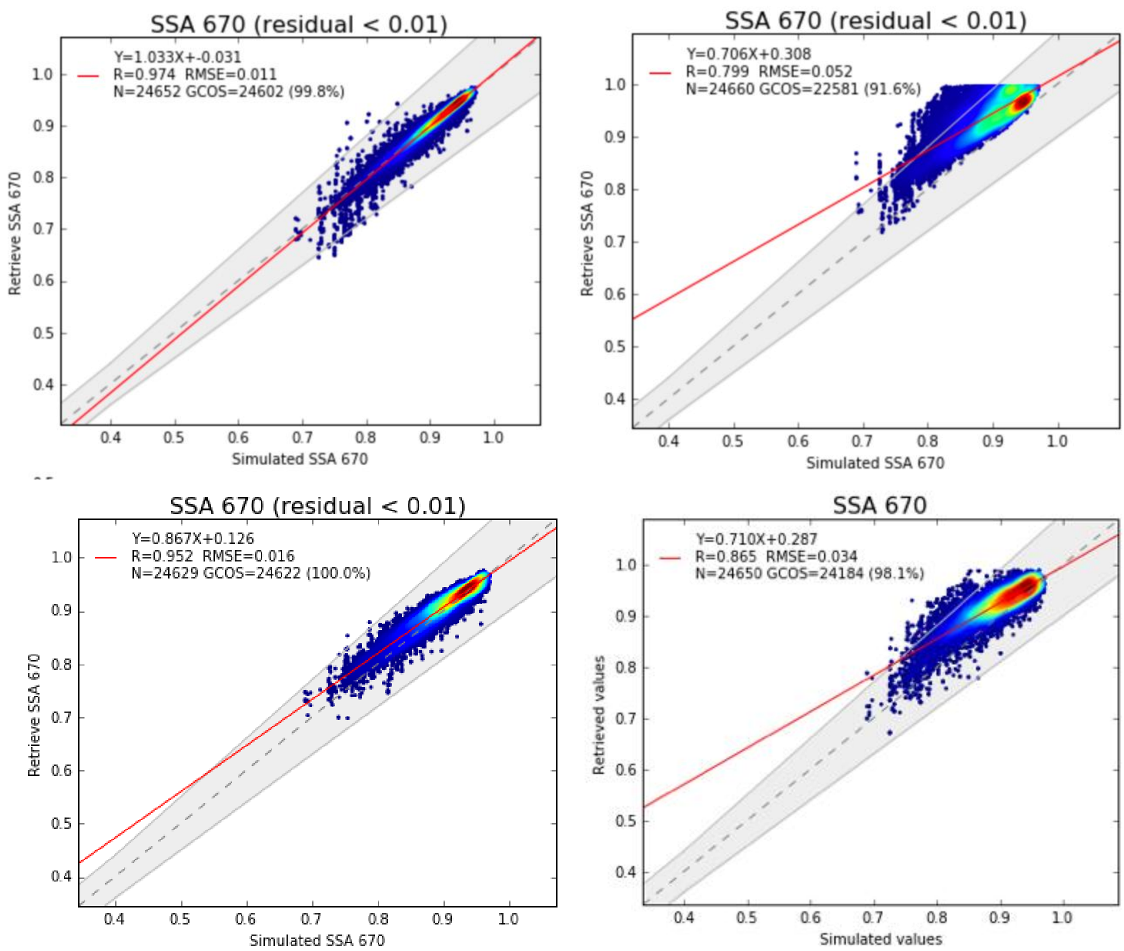

Figure 5.3. SSA of aerosol retrieval from 3MI Proxy data using GRASP with different retrieval settings:

Upper panel:

-(left): *Case 1* - high performance retrieval with no a priori information on surface reflectance;

-(right): *Case 2* optimized retrieval with no a priori information on surface reflectance;

Lower panel:

-(left): *Case 3* - optimized retrieval using a priori information on surface reflectance;

-(right): *Case 4* - model based retrieval using a priori information on surface reflectance.

Table 5.1 Summary of the comparisons of retrieved parameters retrieved using different scenarios with assumed aerosol properties.

		R -correlation	Slope	RMSE
AOD(550)	Case 1	0.983	0.993	0.01
	Case 2	0.764	1.050	0.035
	Case 3	0.984	1.01	0.03

	Case 4	0.806	1.00	0.039
Angstrom Exponent	Case 1	0.939	0.906	0.11
	Case 2	0.437	0.437	0.163
	Case 3	0.989	1.021	0.311
	Case 4	0.393	-0.52	0.874
SSA(670)	Case 1	0.974	1.03	0.011

Table 5.2 Retrieval speed summary (Cases correspond to the retrieval scenarios in Figs. 1–4).

	Inversion of one pixel	Inversion of one orbit (using a cluster of 100 cores)
Case 1	2 sec per pixel	160 min
Case 2	0.5 sec per pixel	40 min
Case 3	0.2 sec per pixel	20 min
Case 4	> ~ 0.15 sec per pixel	> ~ 15 min

5.2.2 Trade-off of speed and accuracy by decreasing number of used spectral channels

This section illustrates the potential of using the trade-off of retrieval speed and accuracy by decreasing number of the 3MI spectral channels used for the retrieval. Evidently, using less spectral channels reduces the speed of data processing. However, the quality of the retrieval is likely to deteriorate too. Figure 5.4 illustrates the retrieval of aerosol and surface properties using only four wavelengths of 3MI instrument (410, 555, 670 and 870 nm) from nominal eight channels (410, 443, 490, 555, 670, 865, 1650, 2130 nm). The retrieval was conducted using GRASP high performance retrieval settings with no a priori information on surface reflectance. This is the most general retrieval approach that normally is the most vulnerable to the decrease of information content. Nonetheless, as one can see from the Fig. 5.4 both aerosol and surface parameters can be retrieved quite reliably. Comparing Figs. 5.1–5.3 and Fig. 5.4 it is clear that obtained results are inferior only to the results of obtained with high precision settings and in some extend to high performance retrieval using a priori estimates of surface reflectance. The time of calculation has decreased 2 times, as expected. Thus, the reduction of used spectral information can be used in further considerations of potentially appropriate trade-offs in designing 3MI processing system.

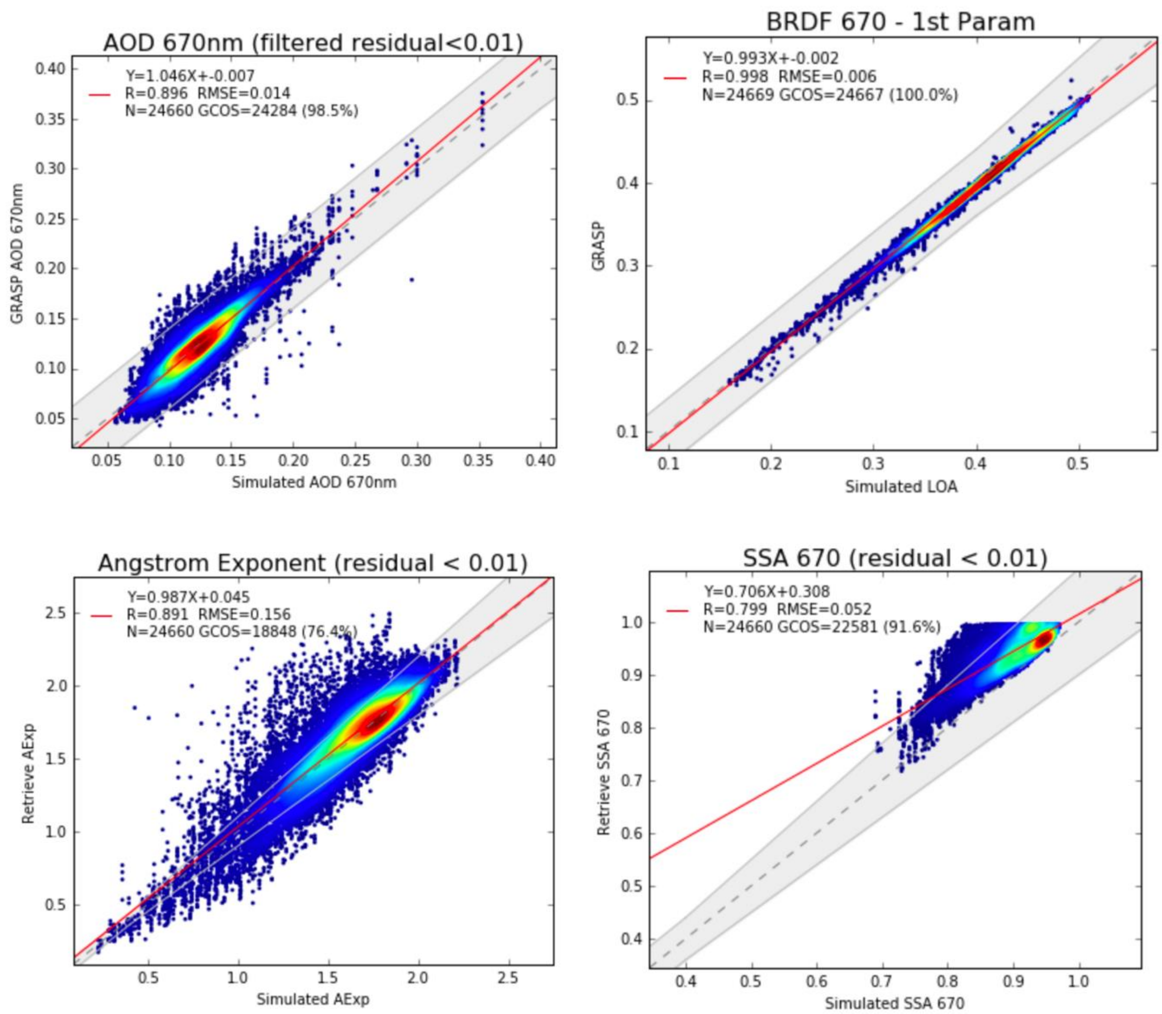

Figure 5.4 Aerosol retrieval from 3MI Proxy data at 4 selected wavelengths using GRASP high performance retrieval with no a priori information on surface reflectance.

Upper panel:

- (left): ADO(670);
- (right) first parameter of BRDF at 670 nm;
-(right) optimized retrieval with no a priori information on surface reflectance;

Lower panel:

-(left) Angstrom exponent;
-(right) SSA(670).

5.3 GRASP applications to EUMETSAT Synthetic Data Set

GRASP algorithm has been applied to the 3MI Level 1c Test **Synthetic Data Set** (generated by EUMETSAT). However, comparing retrieved aerosol properties with those used to generate the synthetic observations showed some differences between assumptions in simulations used by EUMETSAT and in GRASP retrieval, as well as inconsistencies between GRASP RT simulations and simulations used by EUMETSAT. The investigation of potential reasons for these inconsistencies is analysed in this section. Figure 5.5 shows the comparison of retrieved AOD(555) to the values used for generation of synthetic data set. Since the data files provided by EUMETSAT contained only information about AOD on one wavelength 550, only AOD(555) is presented in the figures.

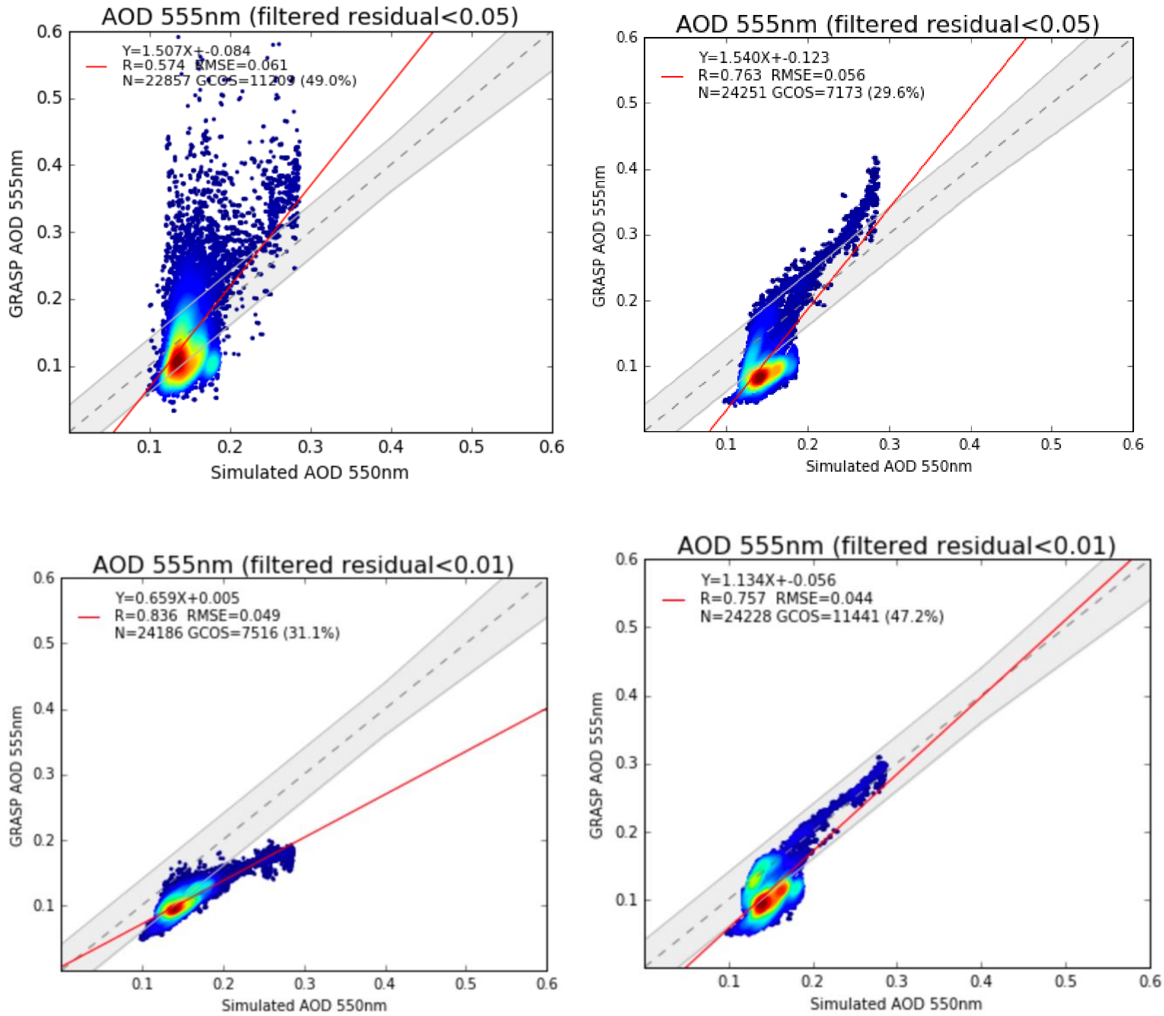

Figure 5.5 AOD of aerosol retrieval for different 3MI Level 1C data using different assumptions in GRASP:

Upper panel:

-(left): inversion Level 1C Synthetic data corregistered by EUMETSAT;

-(right) Inversion Level 1C ideal Synthetic data;

Lower panel:

-(left) Inversion Level 1C ideal Synthetic data simulated with no gas absorption;

-(right) Inversion Level 1C ideal Synthetic data simulated with no gas absorption with relaxed smoothness constraints on spectral dependence of 2-nd and 3-rd BRDF parameter.

As one can see from the first correlation shown on the left side of upper panel of Fig. 5.5, there is a significant spread of the retrieved AOD. The second correlation on the right side of the upper panel of Fig. 5.5 corresponds to the inversion of "ideal" level 1C data generated using the same input for aerosol and surface reflectance. The correlation is notably better than in the case of using level 1C data co-registered from level 1B data. However, it is still notably worse than expected from error free synthetic data (compare to Figs. 5.1–5.3). At the same time GRASP algorithm development within this project does not consider the effect of absorption of atmospheric gases. Generally, this effect is minor for considered 3MI channels and is planned to be addressed in future efforts. At the same time, in the considered example AOD is very low and atmospheric gases absorption may have significant effect. In order to verify the this, LOA team involved in generation of EUMETSAT data has simulated the data for one overlap with no gaseous absorption. The plot for this case is shown on the left side of the lower panel in Fig. 5.5. The correlation for this case has been improved but a notable bias (underestimation) is present. After close analysis of the data it was found that second parameter of BRDF (normalized 2nd parameter MODIS definition is used) in the EUMETSAT dataset has strong spectral dependence that was not allowed in the retrieval settings of GRASP. Such difference in the assumptions can affect aerosol retrieval results. The settings were changed and the last plot (on the right at the lower panel) in Fig. 5.5 shows the corresponding improved correlation. (It should be noted that results shown in the upper panel of Fig. 5.5 are also produced with the updated settings.) The using such strong spectral dependence of the second parameter of BRDF is probably based on some climatological results, however this assumption needs to be re-examined since in most of the surface reflectance analyses the second and third BRDF parameter are rather spectrally constant, e.g. see Litvinov et al. (2011).

5.4 Discussion of challenges and inconsistencies .

It should be noted that, the reproducing of the simulated 3MI data using the Report: "Study METIMAGE/3MI synthetic observation" is rather challenging. For example, the Report doesn't provide the values of spectral complex refractive index, single scattering albedo, and total extinction. The inputs for simulation data provide the phase matrices of aerosol and vertical information. This is fully correct general representation of the data necessary for RT calculations. However, such input is not easy to use for large amount of the data in GRASP simulations since, GRASP uses same set of input parameters in forward simulation as in the retrieval, i.e. including spectral complex refractive index , etc. Moreover, according to our understanding the 3MI Level 1B data that co-registered by EUMETSAT have been corrected and regenerated one or more times. The version of the data used in these studies was finalized early this 2018 year and several important corrections of assumption have been done. Evidently these recent corrections are not discussed in the original report on "Study METIMAGE/3MI synthetic observation". In addition, even Level 1C 3MI ideal data have been generated very recently and were not assumed to be used in the current project, therefore no documentation of these data was provided to retrieval team of ERA project. As a result, both simulated 3MI data of Level 1B and 1C ("ideal") are not fully transparent and hard to be reproduced or checked in the independent study. Unfortunately, in present retrieval efforts some consistency between simulation and the GRASP forward model was observed, and clarifying and fixing this inconsistency is not possible without full support of the team produced the data.

The team generated the 3MI Level 1B and Level 1C "ideal" idea data was contacted and some efforts have been taken by both teams to clarify the differences and inconsistencies. In these efforts, we tried to take into consider all possible factors that can cause the differences in the data simulations. Specifically, the differences between EUMETSAT and GRASP RT calculations can be caused by the following factors:

- differences in Solar Zenith Angle (SZA): in synthetic EUMETSAT/LOA data SZA changes by $\sim 1^0$ for different azimuthal observations , not in GRASP;
- model for vertical distribution of aerosol can be different;
- aerosol models may not be the same;
- molecular scattering is taken by EUMETSAT/LOA from climatologies, while in GRASP it is

approximated.

The above differences are rather objective because they always will be present in the processing of real 3MI data. The only difference in SZA can be accounted in principle but this would result in significantly slowing down the retrieval. The most of the above differences should have only minor effect. At the same time, the considered case (the overlap over very bright desert surface in Libya with very low AOD) is very challenging and even minor inconsistencies may have a notable effect. In order to check this the same "ideal" level 1C data were simulated using GRASP and the same properties of surface reflectance and aerosol as in EUMETSAT data. The data then were inverted using GRASP. The results are shown in Fig. 5.6. The main inconsistency between retrieval and simulation is likely to be related with usage of different aerosol models. In order to check the sensitivity to this factor two retrievals were conducted with two different scenarios: (i) using the same aerosol models (in this case the model based approach was employed) and (ii) using optimized settings (5 binned size distribution with complex index of refraction were retrieved). The upper panel of Fig. 5.6 illustrates the differences for AOD retrieval. They are quite minor. The results for angstrom exponent and SSA were less different and not shown. It should be noted that in the retrievals illustrated by Fig. 5.5 the employed set of aerosol models was fully consistent with those used in EUMETSAT data. Nonetheless, some notable differences remain. Thus, further analysis of potential inconsistencies between EUMETSAT and GRASP RT modeling is desirable. Specifically, parallel calculations of 3MI radiances by both team for several simplified scenarios (e.g., only for molecular atmosphere, for very clear atmosphere with different assumed surface, reflectance, the calculation for one clearly defined aerosol model, etc.) would likely be enough for identifying and addressing the issues. Unfortunately, in frame ordinary collaborations the requested calculations could not be supported due to luck of time and/or resources.

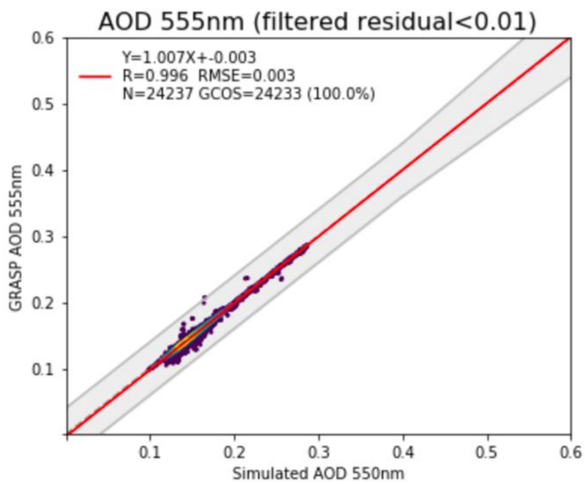

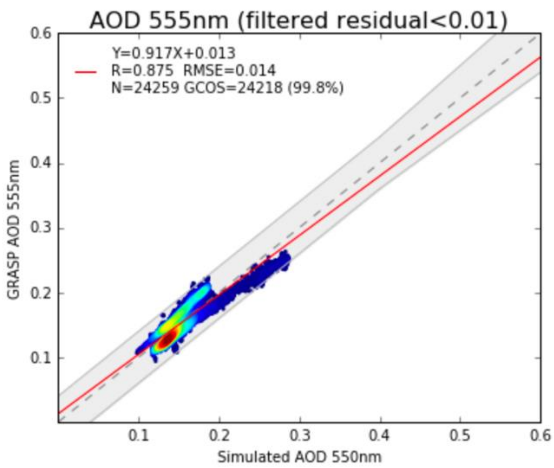

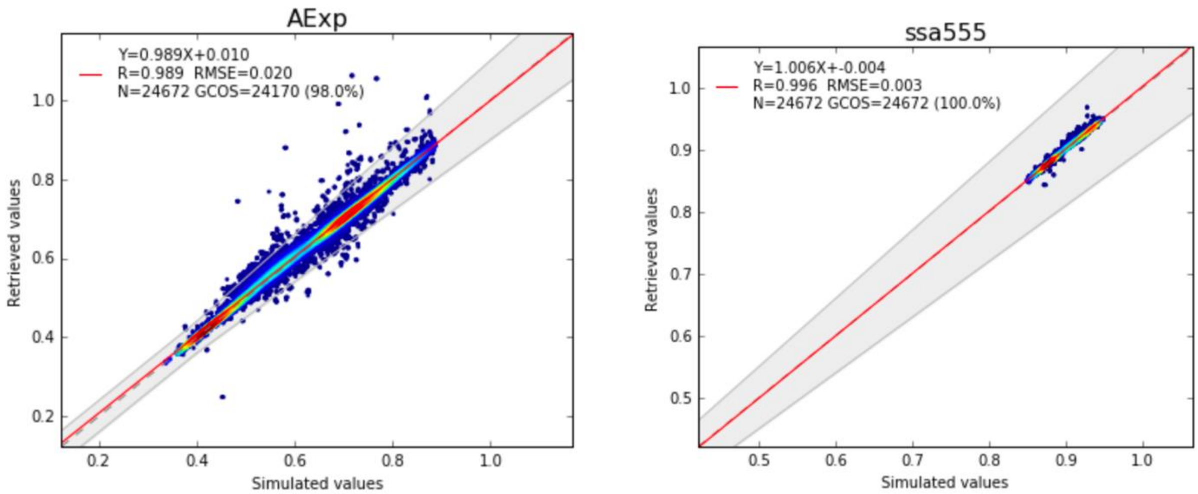

Figure 5.6 Aerosol retrieval from 3MI Proxy data using same input for aerosol and surface as in EUMETSAT data .

<u>Upper panel</u>:

- (left): AOD(555) derived by model based GRASP retrieval with a priori information on surface reflectance;
- (right) AOD(555) using optimized based GRASP retrieval optimized retrieval with a priori information on surface reflectance;

<u>Lower panel</u>:

-(left) Angstrom exponent derived by model based GRASP retrieval with a priori information on

-(right) SSA(555) derived by model based GRASP retrieval with a priori information on surface reflectance.

5.5 Summary

In the frame of the Task 5 activities, GRASP NRT algorithm was applied to the 3MI Level 1c Test Synthetic (generated by EUMETSAT) and Test Proxy (by GRASP) data sets. The performance of the algorithm with different settings identified in Task 4 was tested in order to identify the best trade-off between accuracy and speed of the retrieval. Based on the results GRASP retrieval implemented with *optimized* setting using a priori estimates of surface reflectance appeared to show the most adequate performance. The aerosol properties were retrieved rather accurately (the RMSE for AOD retrieval was below 0.03 and the correlation coefficient of ~ 0.95) for very challenging case of low aerosol loading over bright surface with significantly improved retrieval time compared to the most accurate retrieval with *high performance* settings (20 min for an orbit of 3MI data compared to 160 min). The *model based* retrieval showed even higher retrieval speed, while the accuracy of the retrieval is significantly lower. Nonetheless, this retrieval approach is considered and promising and recommended for possible future considerations for achieving further retrieval acceleration.

The possible potential of using the trade-off of retrieval speed and accuracy by decreasing the number of 3MI spectral channels used for the retrieval has been tested, as requested by EUMETSAT at PM meeting. It was shown that using only four spectral channels (410, 555, 670 and 870 nm) the time of calculation can be decreased in 2 times) while both aerosol and surface parameters can be retrieved quite reliably.

Finally, the apparent inconsistencies between GRASP RT simulations and simulations used by EUMETSAT have been investigated. Two main reasons for the inconsistencies have been identified: (i) EUMETSAT data include absorption by gases, while it is not accounted in GRASP and (ii) 2 BRDR parameters in input for EUMETSAT data has strong spectral feature that is not accounted in GRASP settings. Once these differences were accounted the data retrieved by GRASP from EUMETSAT data agreed quite well with the input for EUMETSAT data. At the same time, some minor inconsistencies seem to be present between EUMETSAT and GRASP RT calculations. Their analysis requires additional efforts (outside of this project).

6. TASK 6: Evaluation of EUMETSAT Co-registration Function

6.1 TASK: Evaluation of EUMETSAT Co-registration Function and comparison with co-registrations functions developed by NOVELTIS

6.1.1 Introduction

Context

The low orbit instrument 3MI on-board the Second Generation of Metop platform will acquire successive measurements in a short time laps while the satellite moves along its orbit. Then it will enable to look at a target under different viewing angles and for different spectral channels. Each measurement will be shifted from its previous one due to the displacement of the satellite. So the different observations of a given target have to be geo-localized and co-registered in a fixed 3MI L1C output grid.

Document content

In a previous phase of the "ERA - Enhanced Retrieval of Aerosol properties: reference and NRT" project, EUMETSAT and NOVELTIS have produced a 3MI L1C dataset according to their own co-registration techniques and a common input 3MI L1B dataset. This task section provides an evaluation of the performances of these two co-registration techniques by analyzing the output 3MI L1C datasets.

6.1.2 Differences between EUMETSAT and NOVELTIS co-registration methods

EUMETSAT approach overview

Definition of the overlap area

The first step in both EUMETSAT and NOVELTIS co-registration technique is to find the area covered by the L1C overlap of a multi-view acquisition sequence. Then the projected coordinates (I,J) of the pixels inside this area in the 3MI L1C output grid and the corresponding coordinates on the sensor focal plane (l,p) should be retrieved.

As is explained in **Error! Reference source not found.**, the overlap area of a multi-view acquisition sequence is defined according to the satellite ground velocity s_v and the VNIR acquisition period T_{VNIR}. Indeed a new overlap is defined for each new VNIR acquisition so the along-track size of an overlap is given by $overlap_{along-track\ size} = s_v.T_{VNIR}$. Then the target area is calculated as the projection of the border of a fictitious VNIR footprint acquired at time T_{OV} (the average time of the multi view acquisition sequence), during T_{VNIR}, *i.e.* with a reduced size in the along-track direction. Then, if (l,p) represents the sensor focal plane coordinates, the objective is to find the limits l_{min} and l_{max} in the along-track direction corresponding to the previous central fictitious VNIR acquisition. For each p, and each $l_{min} < l < l_{max}$ the corresponding projected coordinates in the output 3MI L1C grid (I,J) can be retrieved.

In order to perform this task, EUMETSAT follows this approach:

- l_{min} and l_{max} are found to trim the fictitious VNIR footprint acquired at T_{OV} during T_{VNIR}, thanks to the state vector of the satellite at some reference epoch, the satellite location, altitude and attitude at times T_{OV}, $T_{OV} - T_{VNIR}$, and $T_{OV} + T_{VNIR}$, and the 3MI focal plane definition.

- The trimmed footprint borders are projected on the 3MI L1C output grid.
- The borders are connected, because the spatial sampling at the edges of the 3MI acquisitions is lower than the spatial sampling of the fixed 3MI L1C output grid.
- The projected coordinates (I, J) of the overlap borders are got.

Co-registration technique

Once the overlap area with the corresponding (I, J) coordinates into the fixed 3MI L1C output grid have been defined, the different observations of the multi view acquisition sequence are co-registered as follows. For each pixel (I, J) into the overlap area:

- The LOS in the focal plane of the sensor from which the pixel is seen is retrieved giving the state vector of the satellite at some reference epoch, and the satellite location, altitude and attitude at the acquisition time;
- The fractional coordinates in the 3MI focal plane are computed thanks to the 3MI focal plane model;
- A bilinear interpolation in the 3MI focal plane is performed to retrieve the values of the stoke vectors in the fixed 3MI L1C output grid.

NOVELTIS approach overview

Unlike EUMETSAT, NOVELTIS did not know the 3MI focal plane model. So this model, as well as the state vector of the satellite at a reference epoch and an orbit propagation model, has not been used. In order to cope with this issue, the NOVELTIS approach uses information provided into the L1B geoloc files.

Definition of the overlap area

NOVELTIS has defined the overlap area as follows:

- Regarding the duration of a VNIR acquisition sequence T_{VNIR}, the satellite velocity s_v, and the spatial sampling of the 3MI instrument at the sub satellite point $3MI_{ss}$, the number of along-track lines in the 3MI focal plane, necessary to define a 3MI L1C overlap is equal to:

$$nb_{lines} = ceil\left(\frac{s_v . T_{VNIR}}{3MI_{ss}}\right)$$

where $ceil(x)$ returns the closest integer greater than or equal to x. Thus 35 lines of the focal plane are necessary to cover a 3MI L1C overlap. In order to avoid some holes between two consecutive overlaps, a margin of one additional line at the beginning and one additional line at the end of the overlap has been taken;

- Considering a multi view acquisition sequence of 14 VNIR acquisitions and 4 sub-overlaps of 12 SWIR acquisitions, see **Error! Reference source not found.**, the central acquisition time of a L1C overlap is equal to the acquisition time of the 2130nm spectral channel in the 8th SWIR acquisition sub-sequence of a L1C overlap. As is illustrated in Figure 6.1, the 8th SWIR acquisition sub-sequence of a given L1C overlap is a SWIR acquisition sub-sequence only.

Time (s)	-143	-132	-121	-110	-99	-88	-77	-66	-55	-44	-33	-22	-11	T_{OV}	11	22	33	44	55	66	77	88	99	110	121	132	143
VNIR overlap	1		2		3		4		5		6		7		8		9		10		11		12		13		14
SWIR ov. 1							1	2	3	4	5	6	7	8	9	10	11	12									
SWIR ov. 2								2	3	4	5	6	7	8	9	10	11	12	13								
SWIR ov. 3									3	4	5	6	7	8	9	10	11	12	13	14							
SWIR ov. 4										4	5	6	7	8	9	10	11	12	13	14	15						

Figure 6.1: VNIR and SWIR acquisition sub-sequences of a multi view acquisition sequence covering a L1C overlap.

Then the pixels' coordinates of a 3MI L1C overlap will be derived from the pixels latitude and longitude of the 2130nm spectral channel acquisition in the 8th SWIR acquisition sub-sequence of the considered overlap. Thereby l_{min} and l_{max} have been computed as follows:

$$l_{min} = \frac{N_{L_{SWIR}} - 37}{2}$$

$$l_{max} = \frac{N_{L_{SWIR}} + 37}{2}$$

where $N_{L_{SWIR}}$ is the number of line in the sensor focal plane of a SWIR acquisition;

- The (lat, lon) coordinates corresponding to the sensor pixels $(l, p, l_{min} < l < l_{max})$ of the 2130nm spectral channel acquisition in the 8th SWIR acquisition sub-sequence of a L1C overlap are projected into the fixed 3MI L1C output grid as follows:

$$I = round\left(grid_{param}(lat^{\circ} + 90) - \frac{1}{2}\right)$$

$$J = round\left(grid_{param}\left(\cos lat^{\circ}\left(long^{\circ} - ref_{long}\right) + 180\right) - \frac{1}{2}\right)$$

, where $grid_{param}$ is the number of points per degree of latitude, and ref_{long} is the reference longitude. Then a surface is obtained in the fixed 3MI L1C output grid corresponding to the overlap extent;

- Due to the spatial sampling differences between the 3MI acquisitions and the fixed 3MI L1C output grid, the surface obtained previously contains some holes. These holes are closed with a mathematical closing morphology operation.
- The indices (I, J) of all the pixels in the overlap area are stored.

Co-registration technique

Once the overlap area with the corresponding (I, J) coordinates into the fixed 3MI L1C output grid has been defined, the different observations of the multi view acquisition sequence are co-registered as follows for each viewing direction and spectral channel:

❖ A regular grid is built according to the (lat, lon) coordinates of the considered acquisition in the geoloc L1B file, using the WGS-84 system of projection, and the 3MI spatial sampling at sub satellite point. Then the stoke vectors, angles, and ancillary data of the considered acquisition are interpolated on this grid in a multi band image;

❖ The considered acquisition is co-registered, with the 2130nm spectral channel acquisition in the 8th SWIR acquisition sub-sequence of the L1C overlap as base image. For the multi band images corresponding to the acquisition to register and to the central acquisition, the first component of the stoke vectors, *i.e.* the reflectance values, are used for the co-registration, based on a feature extraction technique. Tie points are extracted, a transformation model is derived and a bilinear interpolation on the grid of the central acquisition is performed;

❖ The (I, J) pixels coordinates of the overlap into the fixed 3MI L1C output grid are projected into the grid of the co-registered acquisition, providing fractional coordinates in the latter grid. Then a bilinear interpolation is performed in order to retrieve the stoke vectors, angles, and ancillary data values of the considered co-registered acquisition into the fixed 3MI L1C output grid.

Main differences

The two co-registration methodologies are very different.

The EUMETSAT methodology relies on a perfect knowledge of the 3MI focal plane model and of 3MI state vector at any moment thanks to orbit propagation equations. The geographical coordinates of the acquired pixels for any viewing direction and channel stored in the L1B geoloc products are never used. As NOVELTIS did not know the 3MI focal plane model and the orbit propagation equations used by EUMETSAT, the NOVELTIS methodology generates an intermediate image for each acquisition based on the geographical coordinates of the acquired pixels stored in the L1B geoloc products. Then the co-registration function aims at correcting the potential errors of the geographical coordinates stored for each pixels of any acquisition.

In addition, NOVELTIS has derived the overlap area from a physical central SWIR acquisition whereas the overlap area defined by EUMETSAT is built according to a fictitious central VNIR acquisition.

The consequences of these differences on the output 3MI L1C datasets are assessed in the following section.

6.1.3 Absolute comparison

Approach

In order to assess the quality of the co-registration techniques implemented by EUMETSAT and NOVELTIS, the reflectance values of the 3MI L1C datasets produced with the two methods have been compared to the reflectance values of a "perfect" L1C dataset produced by LOA from a geometric and radiometric point of view. The reflectance values contained in the latter dataset have been generated thanks to a forward model directly from the co-registration grid. The 3MI L1C datasets relative to the 2008 orbit, generated with simulated data acquired on February 23rd, 2008 between 08:49:45s and 09:22:01s, have been chosen for this comparative study. As no specific parallax correction has been applied in NOVELTIS L1C dataset, the corresponding EUMETSAT L1C dataset has been chosen for comparison.

Geometric quality of the produced L1C datasets

The geometric quality of a co-registration techniques is assessed by retrieving, for each 3MI L1C pixel, its real coordinates in the fixed output grid. Then, in order to assess the geometric quality of the produced L1C datasets and thus of the co-registration techniques, the remaining offset between an acquisition in EUMETSAT or NOVELTIS L1C datasets and the corresponding acquisition in the "perfect" L1C dataset is computed.

In order to get these offsets the edges in the reflectance values for each viewing direction and spectral channel of an overlap have been extracted by convolution with a sobel filter for both EUMETSAT, NOVELTIS and "perfect" L1C datasets. Then a matching between the edges of the reflectance values of a given overlap, viewing direction and spectral channel for EUMETSAT or NOVELTIS L1C dataset, and the edges of the reflectance values of the corresponding overlap, viewing direction and central channel for the "perfect" L1C dataset has been performed. The normalized cross correlation metric has been used to assess the matching quality. The correlation surface C between the reflectance values of a given overlap, viewing direction and spectral channel for EUMETSAT or NOVELTIS L1C dataset, noted I, and the reflectance values of the corresponding overlap, viewing direction and spectral channel for the "perfect" L1C dataset, noted B, has been computed by FFT:

$$C = |ifft(fft(I)fft(B))|$$

The location of the maximum of correlation, *i.e.* the correlation peak, provides approximated pixel offsets $(\widetilde{\Delta x}, \widetilde{\Delta y})$, with a precision equal to 1 3MI L1C pixel as is illustrated by the left plot in Figure 6.2.

The obtained approximated offsets have been refined by the computation of a 4th degree bivariate polynomial fitted in a 5×5 window centred on the location of the correlation peak (black square in the “Correlation surface” and “Neighbourhood maximum” in Figure 6.2). 25 values of the polynomial for the different pixel locations in such a window enable to compute the 15 coefficients $A, \dots P$ of the polynomial:

$$Ax^4 + By^4 + Cx^3y + Dx^2y^2 + Exy^3 + Fx^3 + \cdots + Jx^2 + Ky^2 + Lxy + Mx + Ny + P = 0$$

Once the 4th degree bivariate polynomial has been defined, its value has been computed for each sub-pixel in a 21×21 window centred on the location of the maximum correlation and sampled at 0.1 surface correlation pixel (black square in the “Neighbourhood maximum” and “Interpolated max neighbourhood” in Figure 6.2). For a given overlap, viewing direction and spectral channel, the pixel location in this 21×21 window, giving the maximum polynomial value, is equal (after correction of the expected displacement linked to the proposed methodology) to the sub-pixel offsets $(\Delta x, \Delta y)$ between EUMETSAT or NOVELTIS data and the corresponding “perfect” L1C data with a precision of 0.1 3MI L1C pixel.

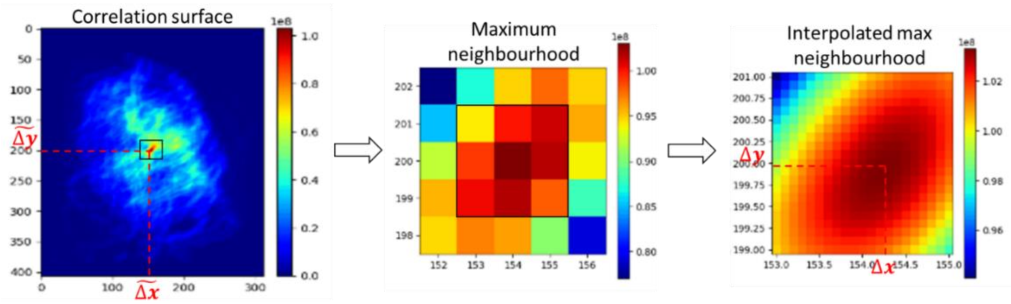

Figure 6.2: Sub-pixel offset estimation process.

If the EUMETSAT and NOVELTIS co-registration technique is efficient, the global remaining offsets $(\Delta x, \Delta y)$ should tend to 0 for the different viewing directions and spectral channels. Then, two evaluation metrics have been implemented:

- **Global offset** (in 3MI L1C pixel): this metric is equal to the absolute global offset for a given overlap, viewing direction and spectral channel. It is defined as:

$$\Delta = \sqrt{\Delta x^2 + \Delta y^2}$$

This metric represents the geometric accuracy of the compared datasets and thus of the co-registration techniques.

- **Confidence** (in %): this metric is equal to the value of the correlation peak and provides a confidence index on the obtained offset. Indeed, if the correlation peak is high, the correlation is good and the derived offset is reliable. On the contrary, if the correlation peak is low, the correlation is bad and the derived offset is not reliable. Then this metric represents the geometric precision of the compared datasets,

- and thus of the co-registration techniques.

Radiometric quality of the produced L1C datasets

Even if the geometric quality of a co-registration method is good, it is not sure that the 3MI pixels located at their real location have their real reflectance values. On the other hand, if a geometric error is observed, it is interesting to know what the error on the reflectance values knowing this geometric error is. Then in order to assess the radiometric quality of EUMETSAT and NOVELTIS datasets, and thus of the co-registration techniques, the following method has been applied. For each pixel of the 3MI L1C output grid, a percentage of error regarding the "perfect" L1C dataset has been computed for the reflectance values of each spectral channel and viewing direction as follows:

$$\%_{error} = 2 * 100 \frac{reflectance_{REF} - reflectance_{EUM/NOV}}{reflectance_{REF} + reflectance_{EUM/NOV}}$$

where $reflectance_{REF}$ is the reflectance value of a pixel of the "perfect" L1C dataset for a given spectral channel and viewing direction, whereas $reflectance_{EUM/NOV}$ is the reflectance value of the corresponding pixel of the EUMETSAT or NOVELTIS L1C dataset for the corresponding spectral channel and viewing direction. An illustration of the percentage of error on reflectance values for the first viewing direction and the 410nm spectral channel between the NOVELTIS and "perfect" L1C datasets is provided in Figure 6.3 for 10 successive overlaps over Southern Europe.

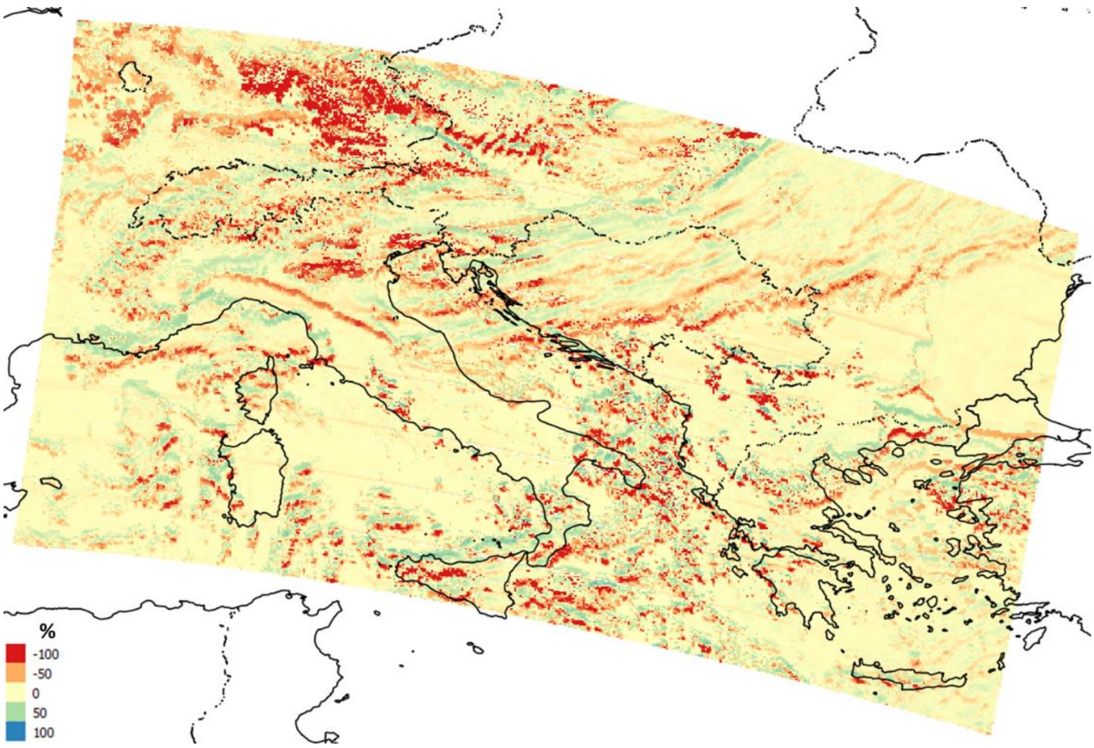

Figure 6.3: Percentage of error on reflectance values for the first viewing direction and the 410nm spectral channel between the NOVELTIS L1C dataset and the "perfect" L1C dataset for 10 successive overlaps over Southern Europe.

These percentages of error have been computed for all the pixels of the 3MI L1C datasets produced separately by EUMETSAT and NOVELTIS, for all the viewing directions and all spectral channels. Then histograms representing the number of pixels by bin of absolute percentage of error have been generated. Finally, several additional metrics in order to assess the quality of these histograms, and thus of the radiometric quality of the co-registration techniques, have been studied:

- **Global error** (in %): this metric is equal to the absolute percentage of error corresponding to the bin with the maximum of pixel in which, and reveals a bias on the produced datasets. If the datasets produced by EUMETSAT and NOVELTIS were perfect, this metric should be equal to 0% because all the pixels of the datasets would be in the central bin. This metric represents the radiometric accuracy of the tested datasets and thus of the co-registration techniques.
- **Peak maximum** (in %): this metric is equal to the percentage of pixels the absolute percentage of error of which is equal to the global error introduced above. This metric reflects the radiometric precision of the tested datasets, and thus of the co-registration techniques. Indeed if the majority of the pixels of EUMETSAT or NOVELTIS L1C datasets has the same percentage of error regarding the "perfect" L1C dataset, the corresponding method could be qualified as precise. On the contrary, a low peak maximum means that a lot of pixels have different percentages of error, representing a noisy generated datasets regarding the "perfect" L1C dataset.
- **Median error** (in %): this metric is equal to the range of percentage of error for 50% of the pixels with the lowest absolute error. As the latter metric, this one reflects the radiometric precision of the tested datasets and thus of the co-registration techniques. Indeed, the lower the median error, the more the reflectance values of the tested dataset, and thus the more precise the co-registration method is.

A histogram such as those generated with the different defined metrics is illustrated in Figure 6.4.

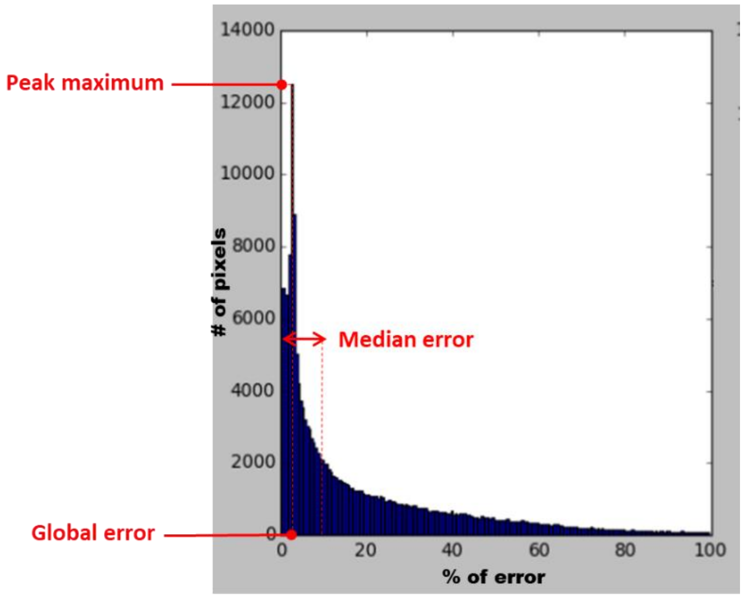

Figure 6.4: histogram of the percentage of error regarding the reflectance values of the pixels of a given overlap, viewing direction and spectral channel between NOVELTIS and "perfect" L1C datasets and defined assessment metrics.

The three additional metrics defined previously allow to characterize the pixels with a small absolute error regarding the "perfect" L1C dataset. These pixels will be located in homogeneous areas, where an error on the location will lead to a small error of reflectance value or in heterogeneous areas if the L1C datasets are perfectly co-registered. If it is not the case, an error on the location of the L1C pixels will lead to a high error of reflectance values, maybe close to or higher than 100%. But the defined metrics do not take into account these pixels with high error due to an imperfect co-registration in heterogeneous areas such as water/ground interfaces.

6.1.4 Results and discussion

Global result

The EUMETSAT and NOVELTIS 3MI L1C datasets have been compared to the “perfect” L1C dataset according to the approach presented above. The different metrics have been estimated and the average results are presented in Table 6.1.

Table 6.1: absolute comparison of EUMETSAT and NOVELTIS L1C datasets with the "perfect” L1C dataset

Dataset	Geometric assessment		Radiometric assessment		
	Global offset (3MI L1C pixel)	**Confidence (%)**	**Global error (%)**	**Peak maximum (%)**	**Median error (%)**
EUMETSAT	1,35	66,79	0,67	10,30	3,45
NOVELTIS	2,61	62,02	0,72	7,70	5,45

According to these results, the co-registration technique used by EUMTESAT is more accurate (from geometric point of view regarding the lower global offset, and radiometric point of view regarding the lower global error) and more precise (from geometric point of view regarding the higher confidence index, and radiometric point of view regarding the higher peak maximum and the lower median error) than the NOVELTIS one. But, for both EUMETSAT and NOVELTIS L1C datasets, an important average remaining offset greater than one 3MI L1C pixel is observed.

In the methodology chosen by EUMETSAT, the location of the different pixels is computed by using information about the satellite and sensor at a given acquisition time. If this technique works better with simulated data than the NOVELTIS one, based on co-registration using the reflectance values of the different acquisitions, the results of these two methodologies should be closer from each other using real data. Indeed, during real operation, various errors, such as deviations from prescribed orbit, attitude variations, uncertainty on the precise position of optical instrument components, or satellite vibrations could appear. Then the EUMETSAT co-registration technique could be impacted by these errors whereas the NOVELTIS one will not.

Results according to the spectral channels

The different metrics have been averaged by spectral channel. Figure 6.5 gives the trend of the geometric accuracy of the generated L1C datasets whereas Figure 6.6 gives the trend of the geometric precision for both EUMETSAT and NOVELTIS methods.

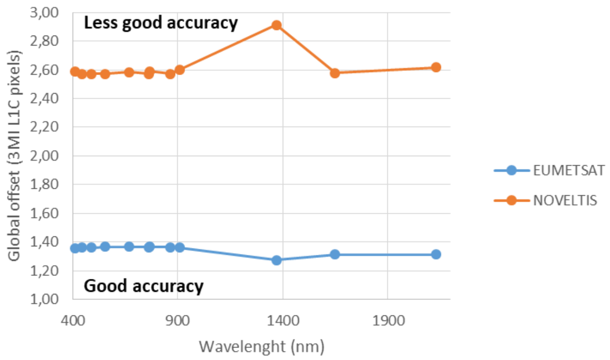

Figure 6.5: Geometric accuracy of the co-registration techniques (global offset) according to the spectral channels.

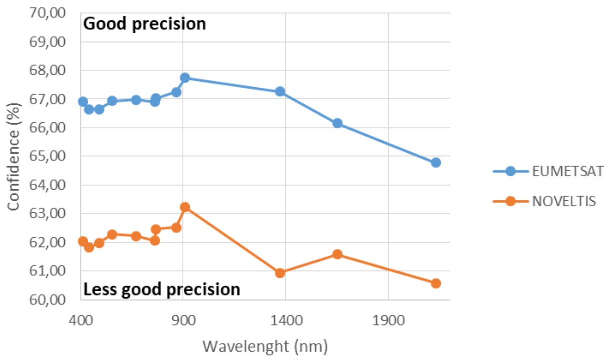

Figure 6.6: Geometric precision of the co-registration techniques (confidence) according to the spectral channels.

Regarding the geometric quality results for both EUMETSAT and NOVELTIS co-registration techniques, they are nearly constant for the different VNIR and SWIR spectral channels. The constant global offset for the different spectral channels between both EUMETSAT and NOVELTIS datasets and the “perfect” L1C dataset, suggests a simple constant bias between the L1C datasets.

The low geometric accuracy obtained for NOVELTIS dataset with the 1370nm spectral channel in comparison with the other spectral channels can be explained by the fact that the reflectance values have a far lower contrast at 1370nm than for the other spectral channels. Then as the reflectance values for this spectral channel is more homogenous, it is harder to register.

Then, considering the highlighted geometric errors, the radiometric quality for both EUMETSAT and NOVELTIS L1C datasets has been assessed. Figure 6.7 gives the trend of the radiometric accuracy of the compared L1C datasets whereas Figure 6.8 and Figure 6.9 give the trend of the radiometric precision for both EUMETSAT and NOVELTIS methods according to the spectral channels.

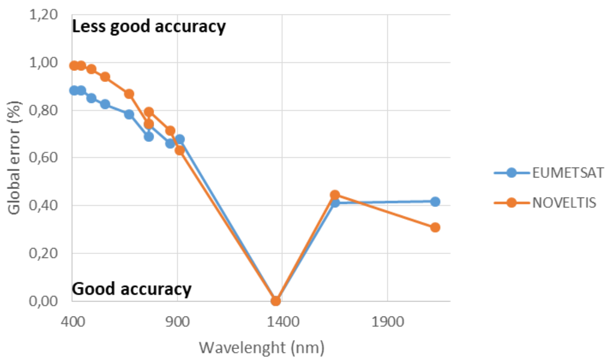

Figure 6.7: Radiometric accuracy of the co-registration techniques (global error) according to the spectral channels.

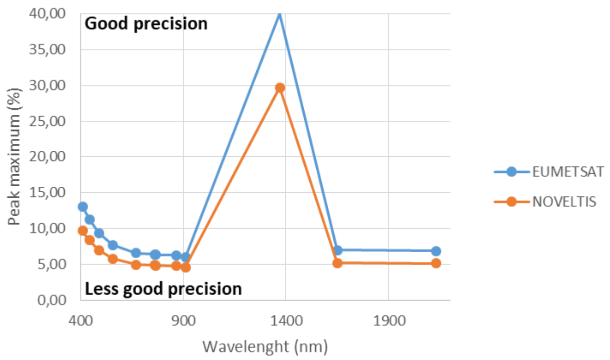

Figure 6.8: Radiometric precision of the co-registration techniques (peak maximum) according to the spectral channels.

Figure 6.9: Radiometric precision of the co-registration techniques (median error) according to the spectral channels.

First and foremost, the very good radiometric quality results obtained for the 1370nm spectral channel can be explained by the fact that the reflectance values of an overlap have a far lower contrast at 1370nm than for the other spectral channels as explained earlier. Then neighbour pixels have the same reflectance values for this spectral channel, and so the computed radiometric metrics are not significant for this channel.

In addition, the higher the wavelength, the more accurate but the less precise the co-registered results for both EUMETSAT and NOVELTIS co-registration techniques. Then it appears that for low wavelengths, the reflectance values for both EUMETSAT and NOVELTIS L1C datasets suffer from a simple bias regarding to the reflectance values of the “perfect” L1C dataset. And, while the wavelength increases, the reflectance values of the spectral channels tend to the real reflectance values of the "perfect" L1C dataset, but are noisier.

This phenomenon can be explained because higher the spectral channel wavelength, higher the reflectance values contrast (without considering the 1370nm spectral channel). So if the contrast of the reflectance values increases, the normalized difference between the compared L1C datasets decreases for homogeneous areas, where reflectance values to compared are close, *i.e.* for pixels with a low global error. Then if the contrast of the reflectance values increases, the radiometric global error decreases, so the radiometric accuracy is better. Moreover, if the contrast of the reflectance values increases, location errors on the compared L1C datasets leads to more important radiometric errors for pixels located in heterogeneous areas such as coastlines, and to a worse radiometric precision.

Results according to the viewing directions

The different evaluation metrics for EUMETSAT and NOVELTIS datasets have been averaged by viewing direction. Figure 6.10 gives the trend of the geometric accuracy of the compared L1C datasets whereas Figure 6.11 gives the trend of the geometric precision for both EUMETSAT and NOVELTIS methods.

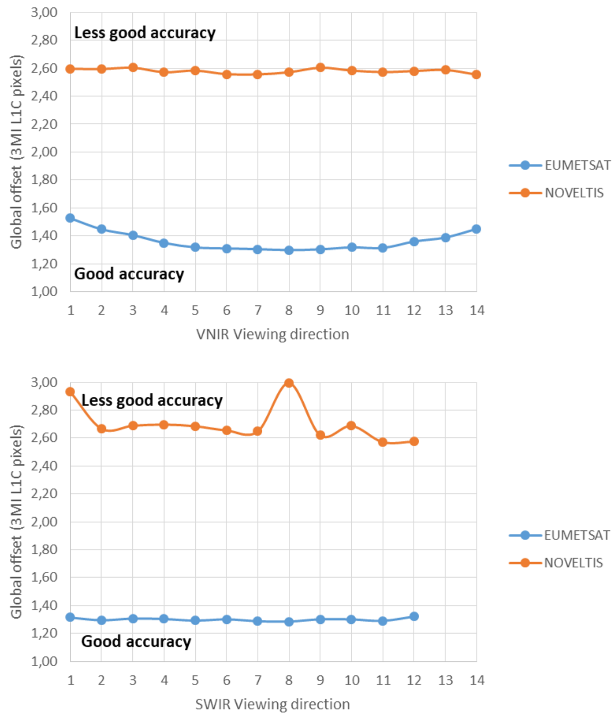

Figure 6.10: Geometric accuracy of the co-registration techniques (global offset) according to the VNIR and SWIR viewing directions (for common viewing directions, VNIR (SWIR respectively) spectral channels are considered only in the left (right respectively) plot).

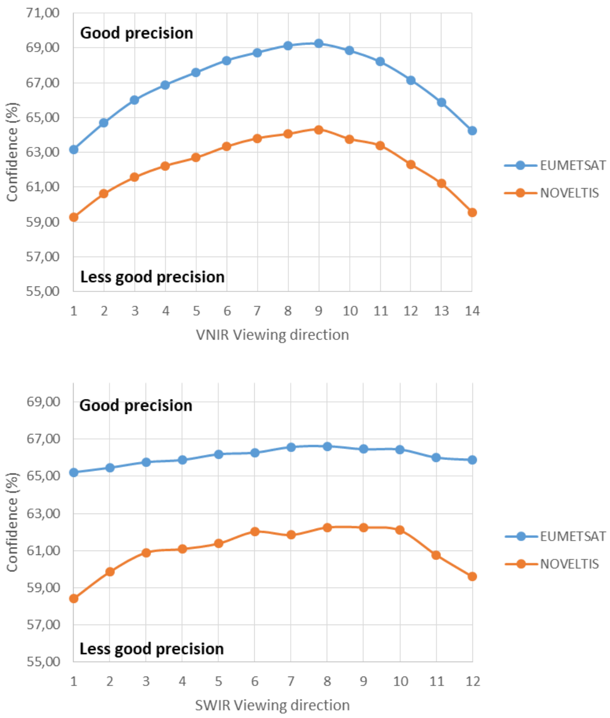

Figure 6.11: Geometric precision of the co-registration techniques (confidence) according to the VNIR and SWIR viewing directions (for common viewing directions, VNIR (SWIR respectively) spectral channels are considered only in the left (right respectively) plot).

Regarding Figure 6.10, the co-registration accuracy is nearly constant according to the viewing directions for both EUMETSAT and NOVELTIS methods. The variations observed for NOVELTIS L1C datasets with SWIR viewing directions have to be mitigated considering the abnormal results for the 1370mn spectral channel. Figure 6.11 spotlights that EUMETSAT and NOVELTIS L1C datasets are more precise for central viewing directions regarding the “perfect” L1C dataset. This is an expected result because no specific parallax correction has been applied on EUMETSAT and NOVELTIS L1C datasets. Thus, if the global offset in comparison with the “perfect” L1C dataset, is nearly the same according to the viewing directions, the confidence index on this offset is higher for viewing directions at NADIR because of similar geometry acquisition at NADIR, in comparison with the corresponding viewing directions of the “perfect” L1C dataset.

The parallax impact is stronger on EUMETSAT L1C dataset than on NOVELTIS L1C dataset. Indeed, in Figure 6.10, the remaining global offset for EUMETSAT L1C dataset is slightly lower for the NADIR acquisitions than for the extreme acquisitions whereas the remaining global offset for NOVELTIS L1C dataset is nearly constant. Moreover, in Figure 6.11, the difference between the confidence index of EUMETSAT and NOVELTIS L1C datasets is higher for the NADIR acquisitions than for the extreme acquisitions; the confidence index is flatter according to the different viewing directions for NOVELTIS L1C dataset. This is due to the NOVELTIS co-registration technique. Indeed, in the NOVELTIS methodology, each 3MI acquisition of a L1C overlap is registered with the central acquisition of the corresponding overlap, which is little impacted by parallax purpose because it is acquired at NADIR. Then the NOVELTIS co-registration technique reduces the parallax impact on the produced L1C dataset although no specific parallax correction is applied.

Then, considering the geometric errors highlighted, the radiometric quality for both EUMETSAT and NOVELTIS L1C datasets has been assessed. Figure 6.12 gives the trend of the radiometric accuracy of the datasets whereas Figure 6.13 and Figure 6.14 give the trend of the radiometric precision for both EUMETSAT and NOVELTIS methods according to the VNIR and SWIR viewing directions.

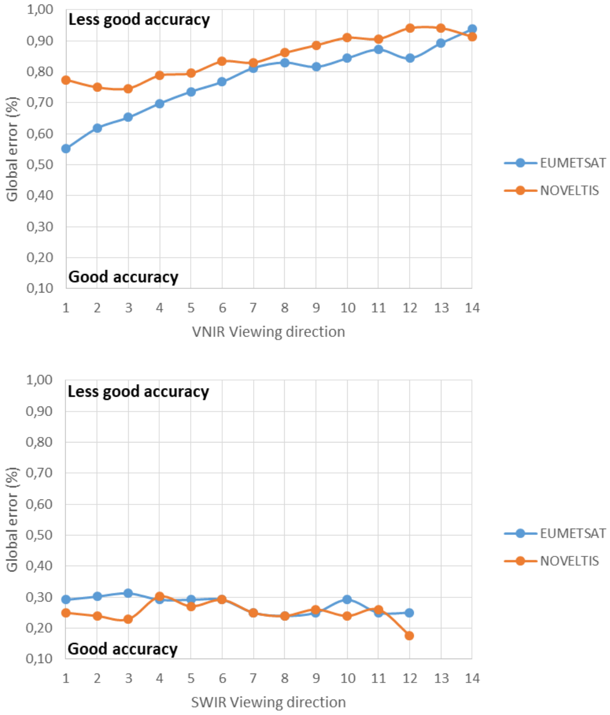

Figure 6.12: Radiometric accuracy of the co-registration techniques (global error) according to the VNIR and SWIR viewing directions (for common viewing directions, VNIR (SWIR respectively) spectral channels are considered only in the left (right respectively) plot).

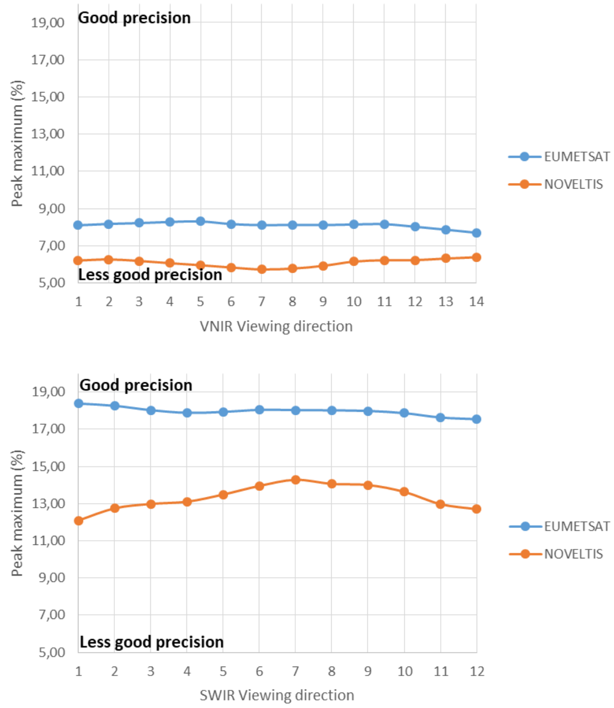

Figure 6.13: Radiometric precision of the co-registration techniques (peak maximum) according to the VNIR and SWIR viewing directions (for common viewing directions, VNIR (SWIR respectively) spectral channels are considered only in the left (right respectively) plot).

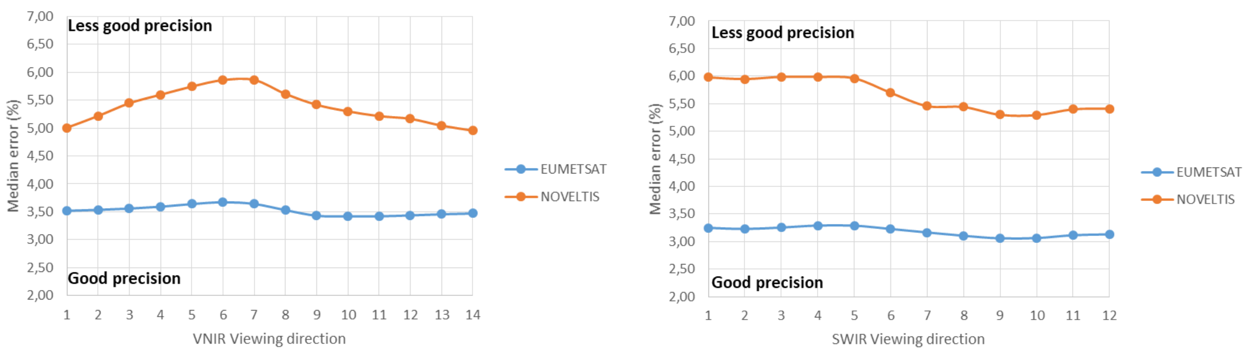

Figure 6.14: Radiometric precision of the co-registration techniques (median error) according to the VNIR and SWIR viewing directions (for common viewing directions, VNIR (SWIR respectively) spectral channels are considered only in the left (right respectively) plot).

Regarding Figure 6.12, the radiometric accuracy of the co-registration techniques seems to be better for SWIR viewing directions than for VNIR viewing directions. However, results for SWIR viewing directions are contaminated by the very good results obtained for the 1370nm spectral channel and cannot be stated as an absolute truth. So the metrics obtained for the SWIR vexing directions will not be longer analysed in this section.

Considering the VNIR directions only, the higher the viewing direction, the lower the radiometric accuracy of the co-registered results for both EUMETSAT and NOVELTIS methodologies, as is presented in Figure 6.12. And as is shown in Figure 6.13 and Figure 6.14, the radiometric precision of EUMETSAT co-registration technique is nearly constant according to the VNIR viewing directions whereas the radiometric precision of NOVELTIS co-registration technique is worse for central viewing directions. No correlation has been found in the scope of this study and further investigations should be led to explain these results.

Thus regarding the presented plots, it seems that the spectral channels have a major impact on the radiometric precision of the co-registered L1C datasets whereas the viewing directions have a major impact on the geometric precision of the co-registered results.

These results for both EUMETSAT and NOVELTIS 3MI L1C datasets should be mitigated regarding the "perfect" L1C dataset. Indeed the absolute comparison of the 3MI L1C datasets produced by EUMETSAT and NOVELTIS to another reference dataset could be erroneous if the reference dataset is not correct. Moreover, regarding the above plots, if the gaps between EUMETSAT and NOVELTIS curves are caused by the differences in co-registration techniques, the similar variations for both EUMETSAT and NOVELTIS curves are linked to the input L1B data and/or to the "perfect" L1C dataset that is used as a reference dataset for these comparisons.

In addition, the absolute comparison of EUMETSAT and NOVELTIS L1C datasets to the "perfect" L1C dataset has shown an important remaining offset. As is shown in Figure 6.6 and Figure 6.10 this offset is not null for the central acquisitions (central SWIR viewing direction and 2130nm spectral channel) of NOVELTIS L1C dataset. However for NOVELTIS co-registration technique, the central acquisition of an overlap is not registered, but interpolated on the 3MI L1C output grid according to the geographical coordinates stored in the L1B geoloc files. And the central acquisition of an overlap is the base image for the registration of the other acquisitions of the considered overlap. Thus, the absolute location of the pixels for all the viewing directions and spectral channels in the NOVELTIS 3MI L1C dataset will be erroneous in comparison with the "perfect" L1C dataset because the pixels location of the central acquisition, as is reported in the L1B geoloc files, is erroneous.

Then a relative comparison is necessary in order to assess EUMETSAT and NOVELTIS co-registration techniques fully.

6.2 TASK: Performance of the aerosol properties retrieval algorithm on 1c datasets

6.2.1 Objectives of Task 6.2 and overview of the efforts

The objective of the Task 6 is to evaluate the quality of co-registered 3MI Level 1C data and assessment of impact of the co-registration uncertainty on the retrieval of aerosol properties from 3MI observation. In the frame of this project, the co-registration of Level 1B 3MI data was done by two different teams (EUMETSAT and NOVELTIS) using different methodologies. The direct comparison of the two different co-registered data sets was done by NOVELTIS team in scope of sub-Task 6.1 The results have been summarized in the corresponding Task 6.1 section.

The sub-Task 6.2 includes the analysis of the co-registration error effect on the retrieval of the aerosol properties. With that purpose the synthetic co-registered 3MI Level 1C data for one orbit were inverted using inversion settings defined in the Task 5 and results were compared with the aerosol parameters that were assumed for the simulations of synthetic data as well as with results of the aerosol retrieval from the ideal 3MI Level 1C data (i.e. with data with no co-registration errors). Thus, Sections 6.2.2 and 6.2.3 of this document discuss the retrieval results correspondingly obtained from EUMETSAT and NOVELTIS co-registered data and Section 4 provide discussion and conclusions.

6.2.2 Aerosol retrievals from synthetic 3MI Level 1C data co-registered by EUMETSAT team

One orbit of Level 1C 3MI data co-registered by EUMETSAT from Level 1B synthetic data was inverted using GRASP code. The model based retrieval using a priori information on surface reflectance was performed. The detailed setting description was provided in Task 5 section. The results of the retrieval were compared with the aerosol parameters that were assumed for the simulations of synthetic data. The illustrations of the retrievals and comparisons are provided in Figs. 6.15 – 6.16.

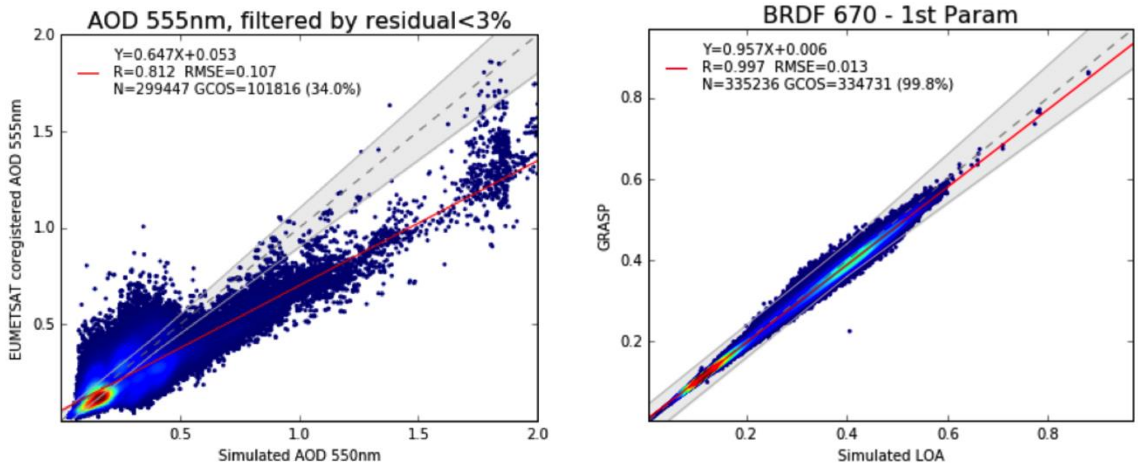

Figure 6.15 The correlation of the results for AOD (left) and first parameter of BRDF (right) derived from 3MI Level 1C data co-registered by EUMETSAT with the values assumed for the generation of Level 1B data.

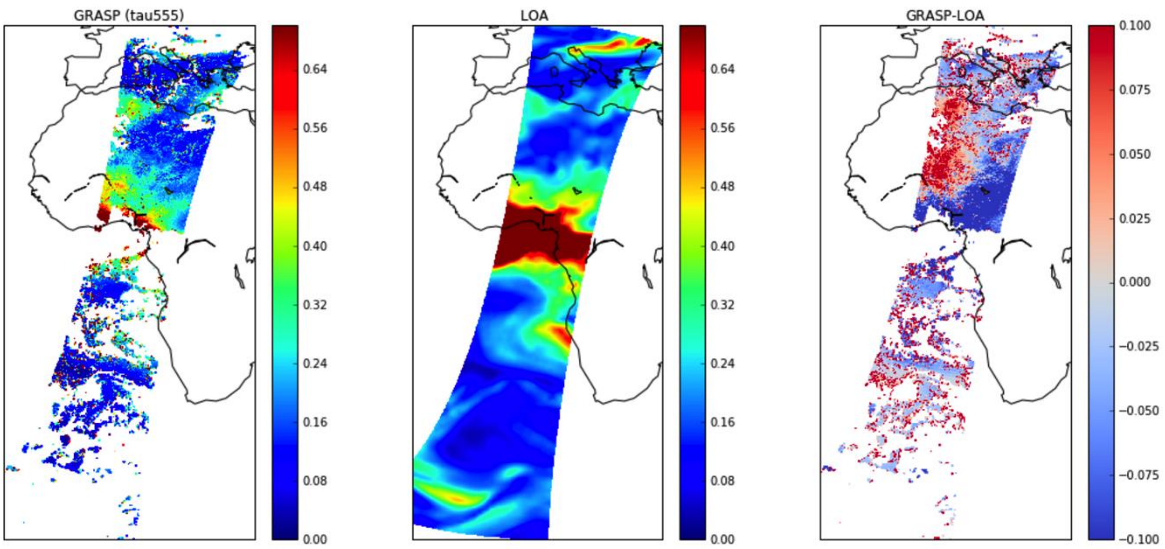

Figure 6.16 The illustration of the results for AOD(555) derived from 3MI Level 1C data co-registered by EUMETSAT with the values assumed for the generation of Level 1B data: (left) – retrieved; (center) – assumed; (right) – difference.

As one can see from Figs. 6.15–6.15, the retrieved surface properties agree very well with assumed values for the simulations. The retrieved AOD(555) correlates well with the assumed values too: correlation coefficient is ~0.82, while the slope of 0.65 and RMSE (Root-Mean-Square-Error) of ~0.1 indicate presence of some discrepancies. The horizontal distribution of the deviation can be seen in Fig. 6.15. It should be noted that Figs. 6.15-6.16 only the retrieval with residual of 3% or less (for radiances) were used.

Thus, the comparisons shown in Figs. 6.15-6.16 suggest that co-registration errors have notable effect on the retrieval of aerosol properties. Indeed, the Task 6.1 section suggested the possibility of the co-registration errors of order of several per cents. Figure 6.17 illustrates the co-registrations error in similar manner as retrievals of aerosol properties in Fig. 6.15.

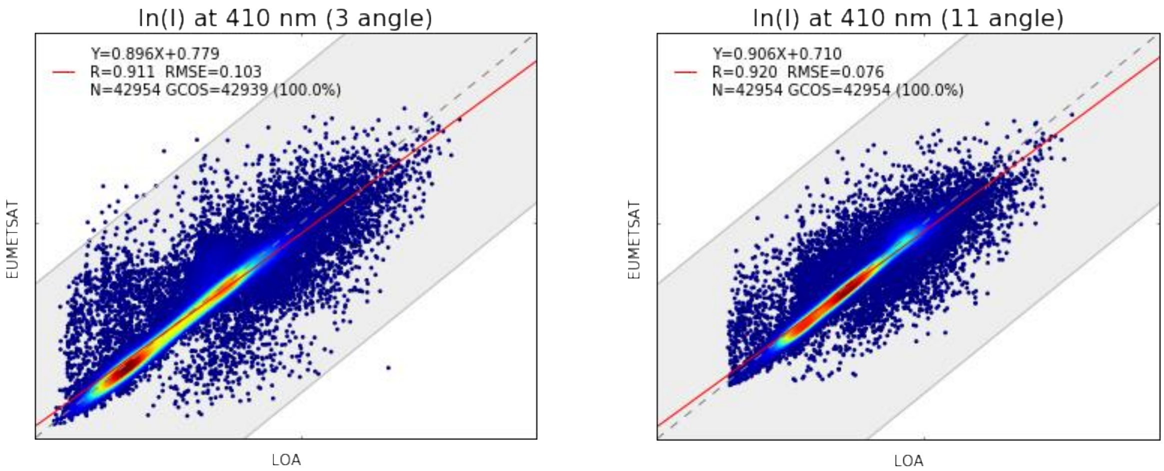

Figure 6.17 The correlation of the radiances provided in 3MI Level 1C "ideal" data with the radiances provided in 3MI Level 1C data co-registered by EUMETSAT.

One can see from Fig. 6.17 that the ideal Level 1C radiances and the co-registered have notable differences: correlations coefficients of 0.91–0.92, slopes of ~0.9 and RMSE of 0.1 – 0.08 in logarithmic scale (that approximately corresponds to 8–10% of relative error). Certainly, the errors of such magnitude should have notable effect on the aerosol retrieval. At the same time, it should be noted that the differences between retrieved and assumed AODs seen in Figs. 6.15-6.16 can be caused not only by the co-registration uncertainties but also by some differences and inconsistencies between the assumptions used for simulations 3MI data and those employed in GRASP retrievals. Unfortunately, as discussed in the Task 5 section hose differences and inconsistencies could not be completely eliminated in the frame of this project. Therefore, in order to exclude the effect of various factors not directly related with uncertainty of co-registration, the retrieval results from co-registered data were compared also with the retrieval results from "ideal" Level 1C co-registered data.

6.2.3 Comparison of aerosol retrievals from synthetic 3MI Level 1C data co-registered by EUMETSAT team and "ideal" 3MI Level 1C data

Figures 6.18 and 6.19 illustrate the retrieval results obtained from the "ideal" 3MI Level 1C data. The comparisons in Fig. 6.18 on the left and right sides differ by filtering criteria. The figure on the right side shows only the results corresponding to best retrievals where the fit with residual of 1% of radiances or better was achieved. One can see that even retrieval from the ideal data have notable spread (RMSE ~0.09) and bias (slope is ~0.7). These features are likely related with the inconsistencies between the calculation of "ideal" Level 1C data and the assumptions made in the GRASP retrieval. The inconsistencies where discussed in Task 5 section.

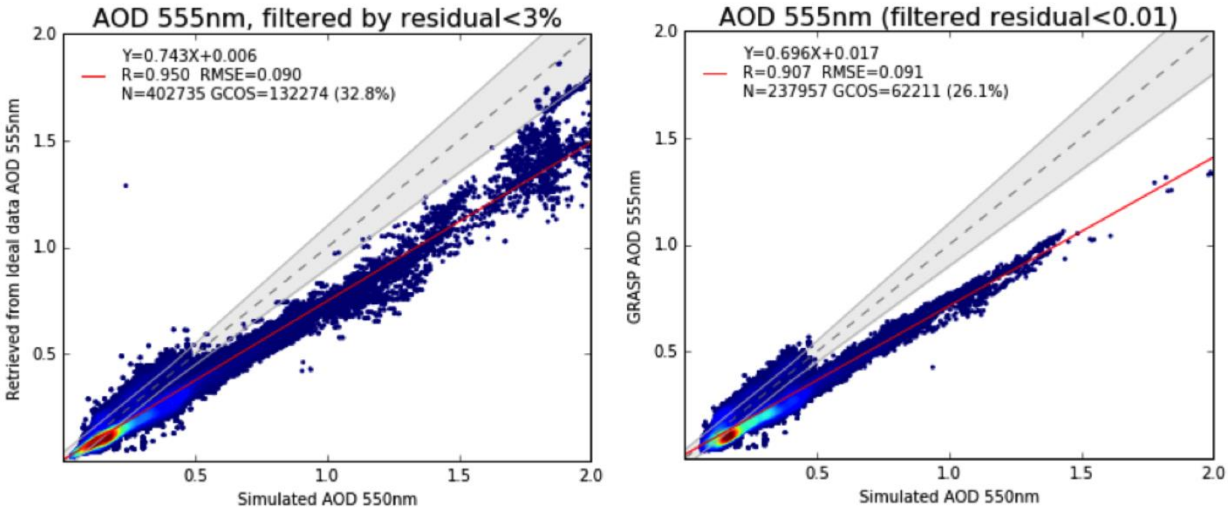

Figure 6.18 The correlation of the results for AOD derived from 3MI Level 1C "ideal" data with the values assumed for the generation of 3MI Level 1C "ideal" data: (left) – for results with fitting error less than 3%; (right) – for results with fitting error less than 3%.

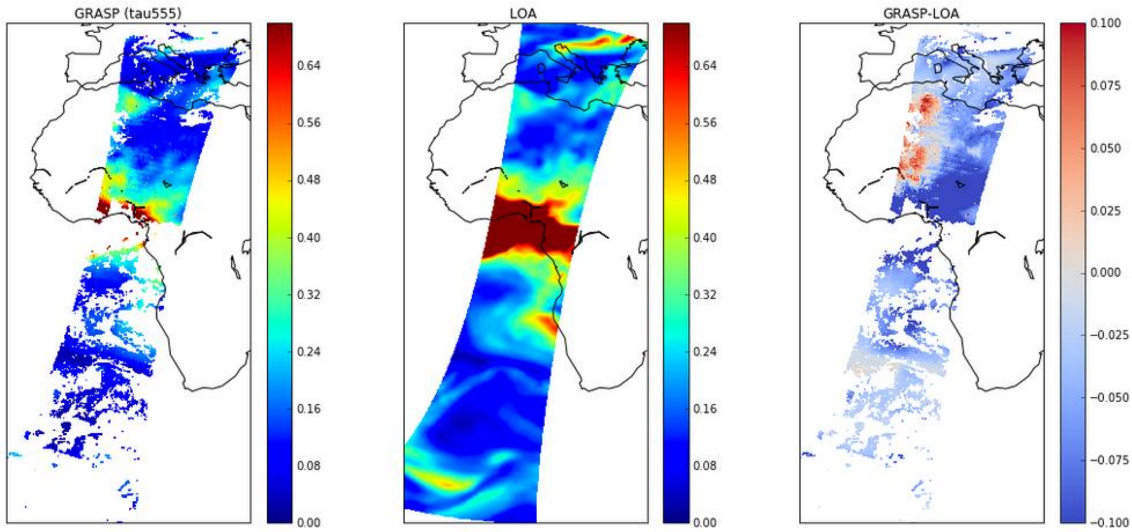

Figure 6.19 The illustration of the results for AOD derived from 3MI Level 1C "ideal" data with the values assumed for their simulations: (left) – retrieved; (center) – assumed; (right) – difference.

Thus, in order to outline only the differences in retrieval caused by co-registration errors, the comparisons were also made of the results obtained from data co-registered by EUMETSAT and from data with "ideal" co-registration. Figures 6.20-6.23 illustrate the results of such comparisons.

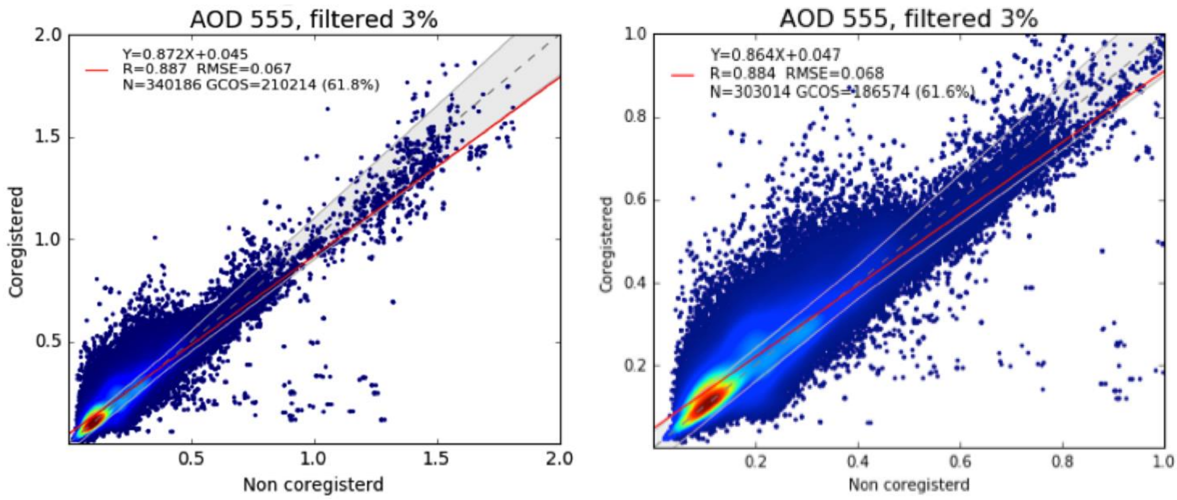

Figure 6.20 The correlation of the results for AOD derived from 3MI Level 1C "ideal" data with the values derived from 3MI Level 1C "ideal" data: (left) – the results are shown up to AOD=2.0; (right) – the results are shown up to AOD=1.0.

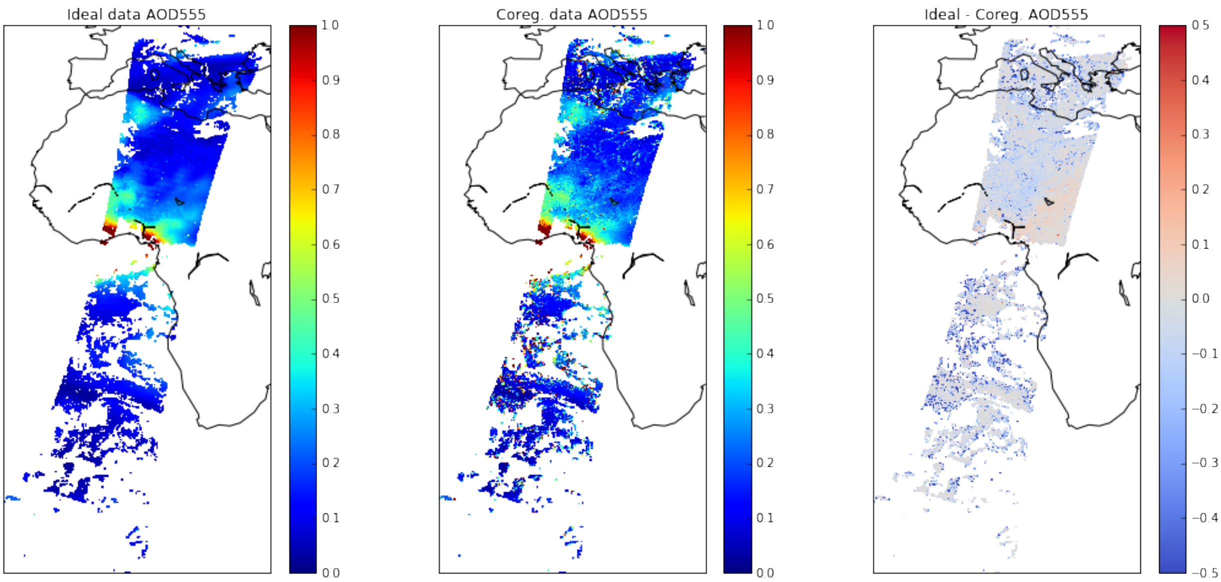

Figure 6.21 The illustration of the results for AOD derived from 3MI Level 1C co-registered by EUMETSAT from 3MI Level 1B data: (left) – retrieved; (center) – assumed; (right) – differences.

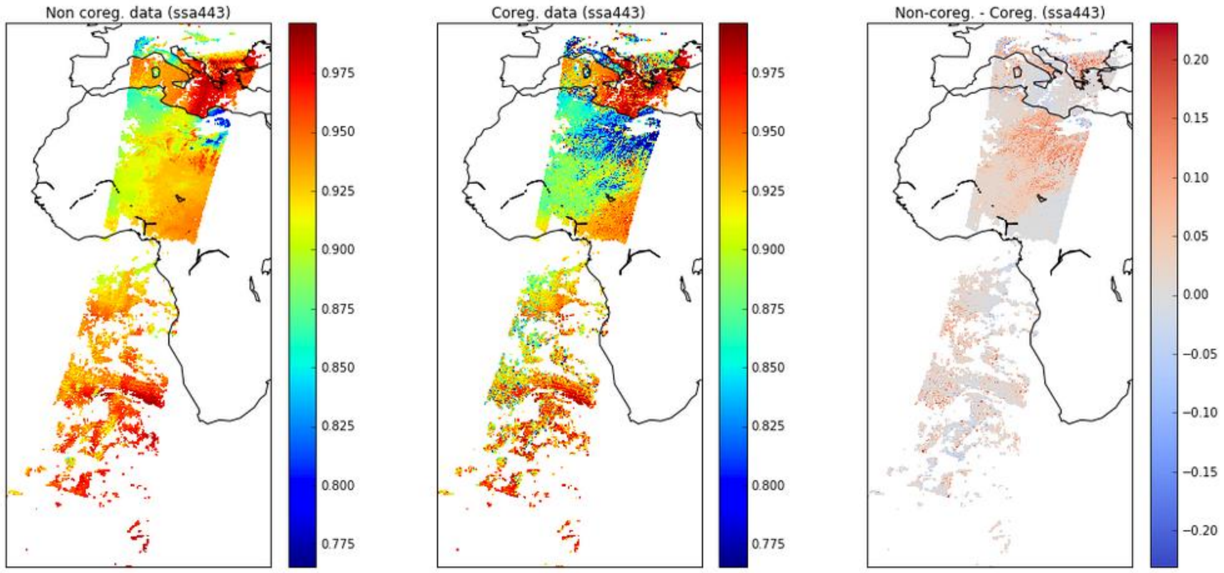

Figure 6.22 The illustration of the results for SSA derived 3MI Level 1C co-registered by EUMETSAT from 3MI Level 1B data: (left) – retrieved; (center) – assumed; (right) – difference.

« ideal » 1C data

	niterations	residual_relative_noise0	residual_absolute_noise1
count	24676.000000	24676.000000	24676.000000
mean	9.612579	0.004609	0.002075
std	2.517298	0.002215	0.000958
min	2.000000	0.001853	0.001220
25%	8.000000	0.003538	0.001781
50%	9.000000	0.004310	0.001982
75%	11.000000	0.005167	0.002280
max	15.000000	0.193616	0.106666

EUMETSAT co-registered

	niterations	residual_relative_noise0	residual_absolute_noise1
count	24566.000000	24566.000000	24566.000000
mean	8.531588	0.010979	0.003538
std	2.158402	0.009434	0.002092
min	2.000000	0.003081	0.001425
25%	7.000000	0.005765	0.002590
50%	8.000000	0.007936	0.003238
75%	10.000000	0.012319	0.003901
max	15.000000	0.170211	0.077280

Figure 6.23 The illustration of the iteration number of statistic of data fitting.

As can be seen from Fig. 6.20 in comparison with Fig. 6.18 the bias almost disappeared. This is especially clear from the graph shown on the right part of Fig. 6.20. Moreover, the agreement is rather evident in the map comparisons in Figs. 6.22-6.23, even for single scattering albedo (except the areas with very low AOD) the parameter that is very difficult to retrieve from satellite observations. The statistical values of the errors introduced by co-registration can be estimated using fitting error statistics shown in Fig. 6.24. The GRASP retrieval could fit 3MI "ideal" Level 1C data with the mean error <0.005% for intensity and error < 0.002 for polarization (Q/I and U/I). For fitting of EMETSAT co-registered data the values increase to <0.011% and <0.004 correspondingly. Therefore, one can consider that the co-registration of the data implemented using EUMETSAT approach introduced an error to cloud-free data of about 0.006% for intensity and 0.002 for polarization that are quite minor errors. Thus, it is possible to conclude that co-registration errors in EUMETSAT approach have rather minor effect on the retrieval results.

6.2.4 Aerosol retrievals from synthetic 3MI Level 1C data co-registered by NOVELTIS team

Initially one orbit of Level 1C 3MI data co-registered by NOVELTIS from Level 1B synthetic data was inverted using GRASP code. The same retrieval settings were used as those discussed in Section 6.2.2. However, the results of retrieval were highly unsatisfactory. One of the reasons was the fact that it was very hard to find perfect correspondence between NOVELTIS co-registered Level 1C data and assumed data in "ideal" calculation for surface reflectance. This is due to different number of pixels in NOVELTIS data set with somewhat different coordinates. In order to exclude these possible uncertainties due to this issue and generally to understand situation better, the detailed and focused study of the situation, was done using one overlap with different retrieval settings. The best results were achieved for most general retrieval approach when aerosol and surface were retrieved simultaneously. Figures 6.24-6.25 show these results compared to the results obtained using similar methodology from "ideal" and EUMETSAT co-registered Level 1C data.

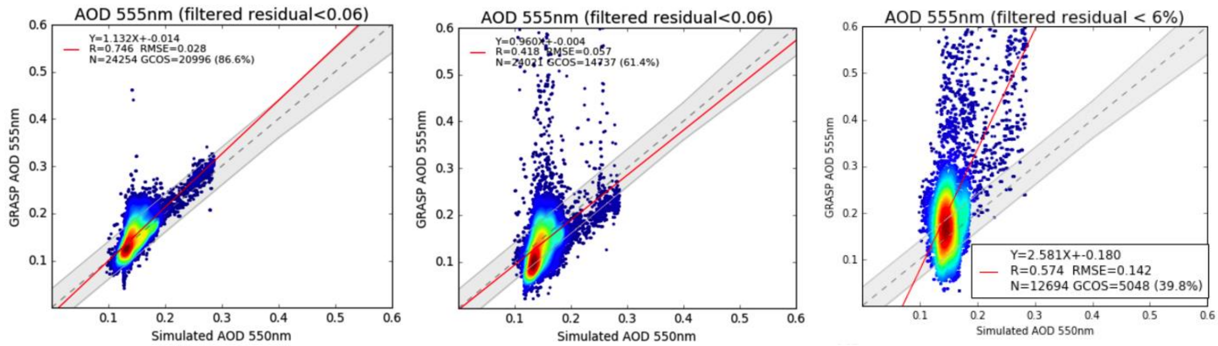

Figure 6.24 The correlation of the results for AOD derived from 3MI Level 1C data with AOD assumed for the generation of the Level 1B data: (left) – retrievals from "ideal" data; (center) – retrievals from EUMETSAT co-registered data; (right) – retrievals from NOVELTIS co-registered data.

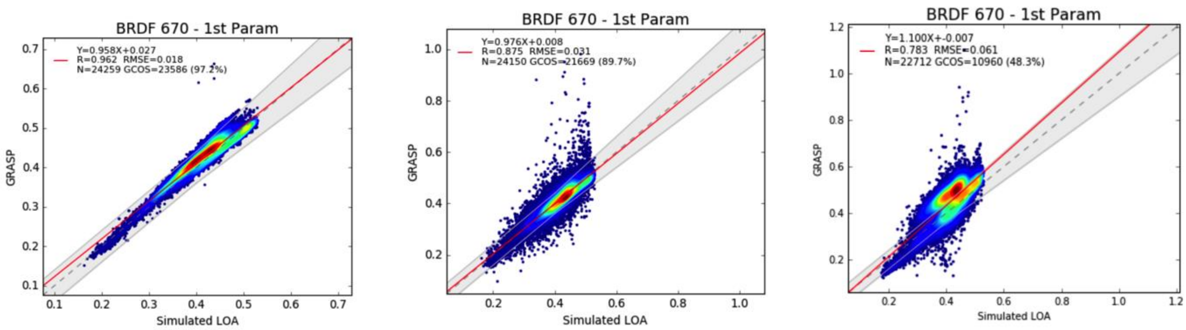

Figure 6.25 The correlation of the results for BRDF derived from 3MI Level 1C data with AOD assumed from in the generation of the Level 1B data: (left) – retrievals from "ideal" data; (center) – retrievals from EUMETSAT co-registered data; (right) – retrievals from NOVELTIS co-registered data.

It can be seen from Fig. 6.24 that retrievals obtained from NOVELTIS co-registered data were quite unsuccessful for AOD. For example, slope was ~3 and RMSE of ~0.14. It should be noted that the results shown in Fig. 6.24 for NOVELTIS data were strongly filtered by values of the residual. The rather large threshold value of the residual of ~6% resulted in 50% reduction of the remaining points. The overall statistic of fitting is shown in Figure 6.26.

	niterations	residual_relative_noise0	residual_absolute_noise1
count	23500.000000	23500.000000	23500.000000
mean	4.609106	0.058414	0.032606
std	0.994501	0.023654	0.011453
min	2.000000	0.025642	0.014479
25%	4.000000	0.045986	0.027759
50%	4.000000	0.057813	0.032374
75%	5.000000	0.067326	0.035398
max	12.000000	0.421296	0.203867

NOVELTIS co-registered

Figure 6.26 The illustration of the iteration number of statistic of data fitting.

Based on this statistic the co-registration using NOVELTIS approach leads to the errors of ~5.5% for intensity and 0.03 for polarizations. These are large errors that are much larger than the errors obtained for data co-registered by EUMETSAT. That was an unexpected result taking into the account the Task 6.1 didn't indicate any particular issue. In order to understand the situation, the direct comparison of 3MI co-registered and "ideal" Level 1C data was made. The results these of comparisons are shown in Figs. 6.26-6.27

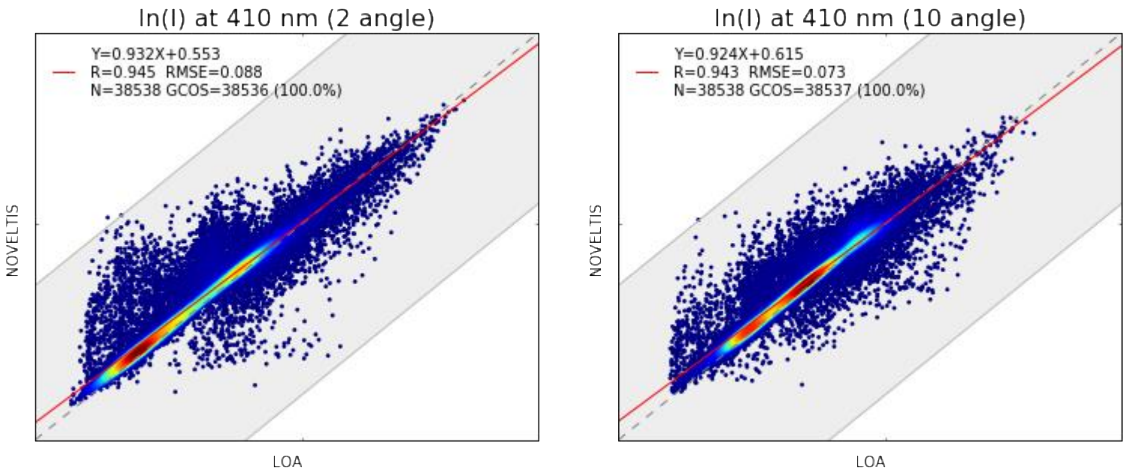

Figure 6.27 The correlation of the radiances given for 3MI Level 1C "ideal" data with the radiances provided in 3MI Level 1C data co-registered by NOVELTIS.

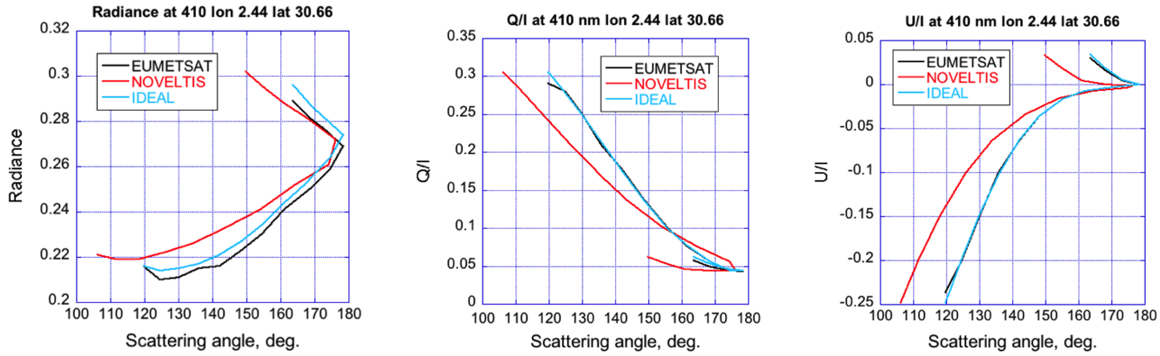

Figure 6.28 The correlation of the radiances given for MI Level 1C "ideal" data with the radiances provided in 3MI Level 1C data co-registered by EUMETSAT and NOVELTIS.

Comparing Fig. 6.27 with Fig. 6.17 it is clear that the actual values of the intensities in NOVELTIS and EUMETSAT data sets are quite consistent for each direction. However, from the illustration in Fig. 6.28 it follows that the angular dependencies of the intensity and polarization obtained from NOVELTIS and EUMETSAT data sets are very different. NOVELTIS data seem to be apart from "ideal" and EUMETSAT data by ~10 degrees. Therefore, the analysis suggests the geometry provided in the NOVELTIS data may need to be corrected if the data are planned to be used for the retrievals.

6.2.5 Discussion and Conclusions

The analysis discussed in previous sections showed that co-registration errors in EUMETSAT approach have rather minor effect on the retrieval results. At the same time, the analysis was done only for AOD while the retrieval of more detailed properties such as aerosol Angstrom Exponent and SSA were not discussed because these parameters couldn't be retrieved accurately even for "ideal" co-registered 3MI Level 1C data. The difficulties were caused by the presence of inconsistencies between simulations and assumptions in the retrieval and the fact that simulated data provide only limited scenarios for assumed aerosol parameters. For example, the calculations for original Level 1B data are dominated by very low AOD (<~0.2–0.3) and variability range of Angstrom Exponent and SSA are very limited. Therefore, here are some illustrations of the retrievals were added for Proxy 3MI data generated using PARASOL and MODIS retrieval climatology (see Task 2 section). Figures 6.29-6.32 illustrate the results for the numerical test where one orbit of Proxy Level 1C data was inverted.

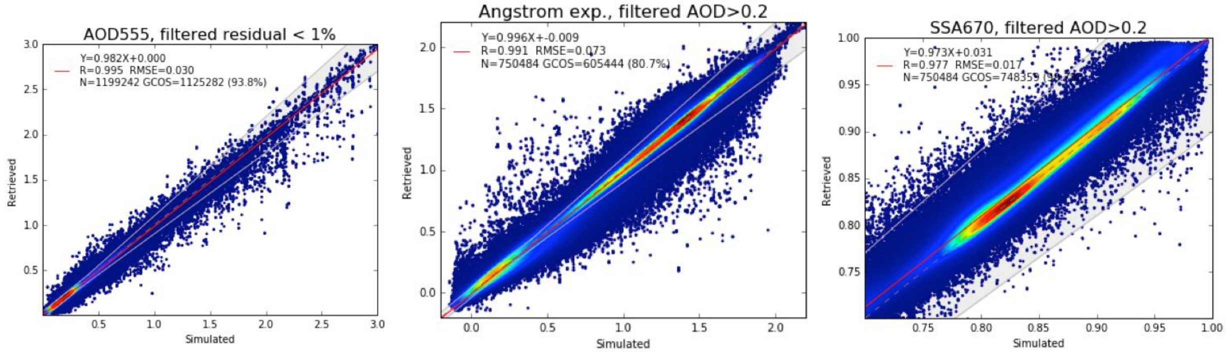

Figure 6.29 The correlation of the results derived by GRASP from 3MI Level 1C data Proxy data simulated using PARASOL and MODIS climatologies with the assumed values: (left) –AOD(555); (center) – Angstrom Exponent; (right) – SSA(670).

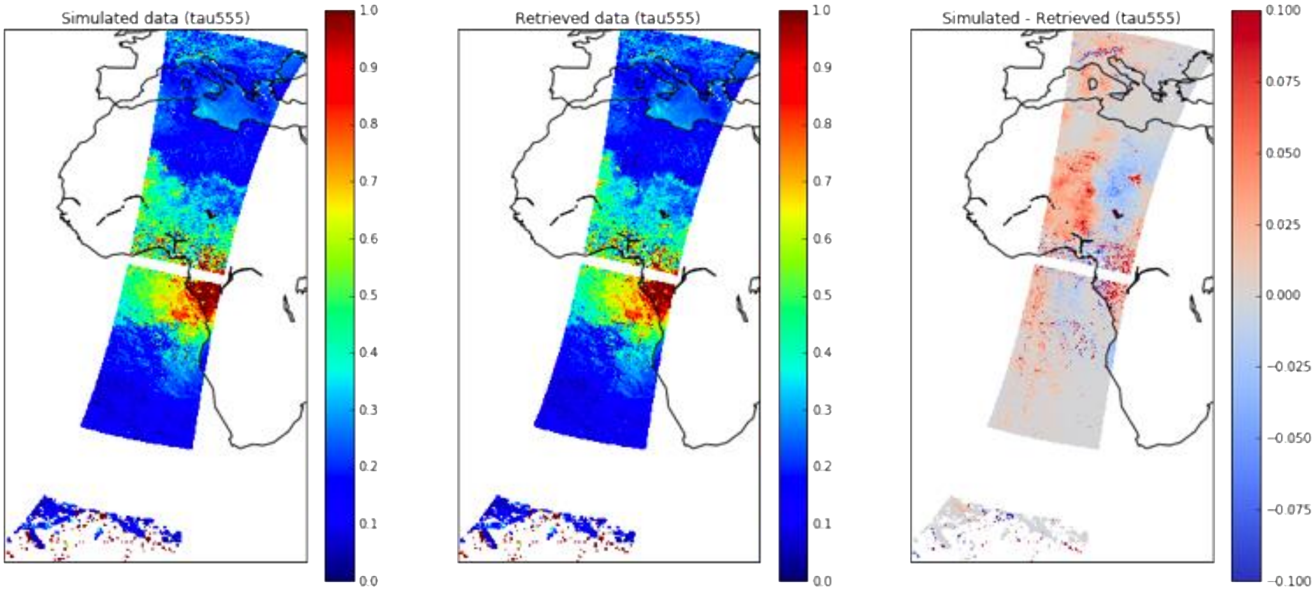

Figure 6.30 The illustration of the retrieval results for AOD(555) derived from 3MI Level 1C data Proxy data simulated using PARASOL and MODIS climatologies with the assumed values: (left) – retrieved; (center) – assumed; (right) – differences.

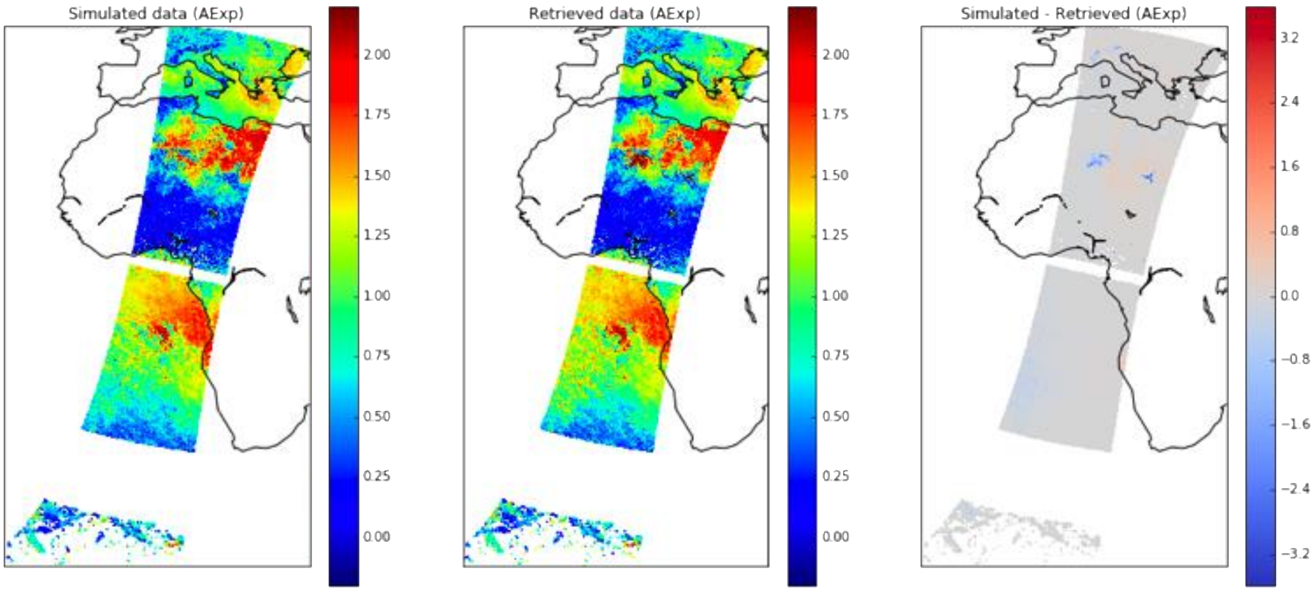

Figure 6.31 The illustration of the retrieval results for Angstrom Exponent (440/870) derived from 3MI Level 1C data Proxy data simulated using PARASOL and MODIS climatologies with the assumed values: (left)- retrieved; (center) – assumed; (right) – difference.

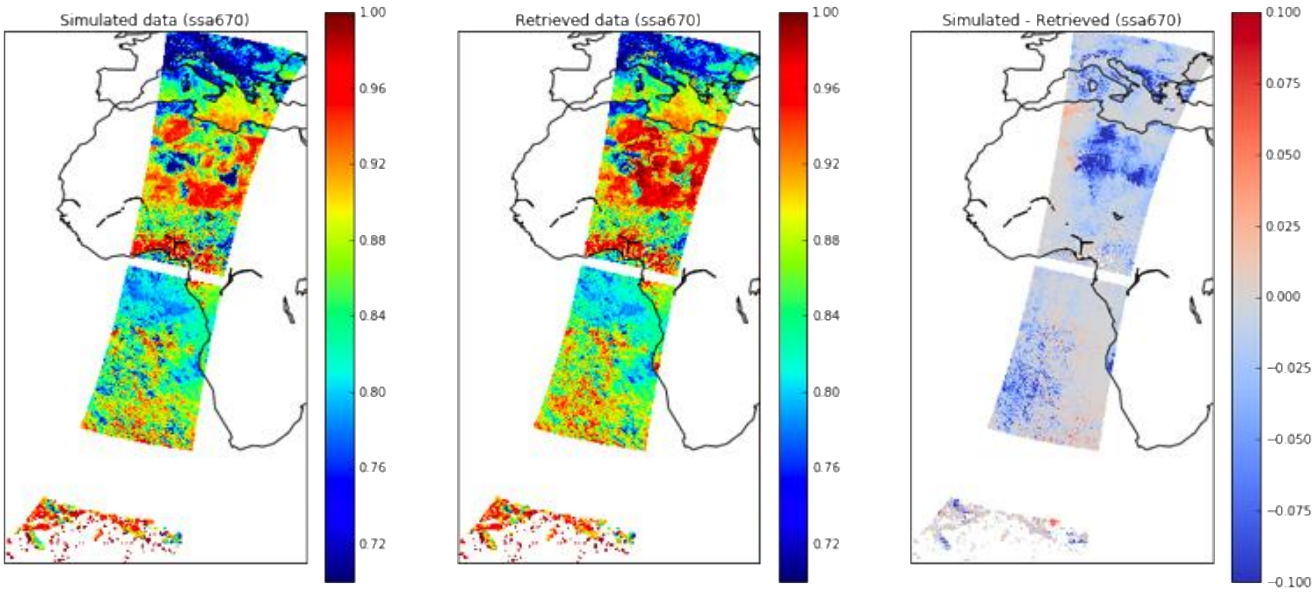

Figure 6.32 The illustration of the retrieval results for SSA (670) derived from 3MI Level 1C data Proxy data simulated using PARASOL and MODIS climatologies with the assumed values: (left)- retrieved; (center) – assumed; (right) – difference.

Thus, it can be seen from Figs. 6 .29-6.32 that the main aerosol parameters including AOD Angstrom Exponent and SSA targeted by the requirements of 3MI mission can be retrieved accurately (no bias and low RMSE) from 3MI Level 1C Proxy data using proposed 3MI/GRASP retrieval algorithm. Certainly, addition of co-registrations errors (~0.6% for intensity and 0.002 for polarization) and uncertainties related with GRASP retrieval assumptions gaseous absorption, same solar zenith angle, modeling molecular scattering, vertical variability of aerosol, etc.) would decrease the accuracy of the aerosol retrievals. However, the spread of the deviations of retrieved values from the assumed and especially bias are likely smaller than those observed in Figs. 6.18-6.19. For example, Fig. 6.33 illustrates the results retrieved from POLDER/PARASOL data compared with the AERONET data. The comparisons are shown for the results obtained for whole archive of PARASOL data (2004 – 2013) and all available AERONET data.

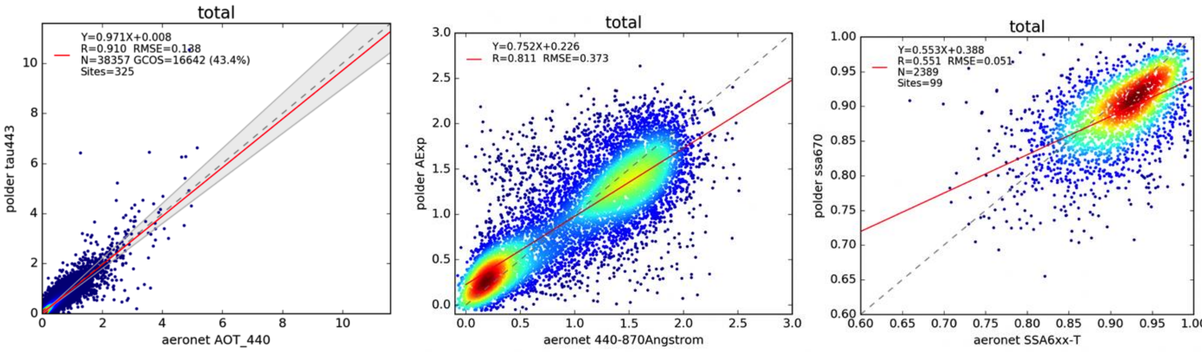

Figure 6.33 The correlation of the results retrieved from POLDER/PARASOL data using GRASP with observation of AERONET. The correlations are shown for entire PARASOL archive (2004 –2013) and all available data of AERONET: (left) – AOD(443); (center) – Angstrom Exponent; (right) – SSA(670).

Figure 6.33 provides the evaluation of the GRASP retrieval from real PARASOL data. Evidently, these real data include all possible uncertainties: calibration, co-registration, and atmosphere radiation models and other errors. In addition, the real data include uncertainties caused by atmosphere and surface inhomogeneities and cloud-mask errors. It would be reasonable to assume that 3MI retrieval should look at least as good and likely notably better because of evident advances in the design of 3MI compared to POLDER/PARASOL. Thus, appealing to the illustrations in Figs. 6.29-6.33 we would like to suggest that the effect of co-registration errors on the retrieval results is likely even less significant compared to the one shown in Figs. 6.20-6.23. If there is an interest to a more accurate evaluation of this effect, additional analysis is desirable.

Thus, the main conclusion of Task 6.2 studies can be summarized as follows:

- The co-registration approach employed by EUMETSAT allows for generating Level 1C 3MI data with accuracy sufficient for reliable retrieval of aerosol properties. Based on analysis of fitting the RMSE introduced by the co-registration can be estimated at the level of 0.6% for intensity and 0.002 for polarization.
- The 3MI data Level 1C co-registered by NOVELTIS could not be properly inverted. The correct calculation of observational geometry needs to be introduced into NOVLETIS co-registration approach if the resulted data are expected to be used for aerosol retrieval.
- The completed evaluation of the effect of data co-registration may not be fully accurate due to presence of several inconsistencies between simulated data and assumptions in GRASP retrieval. The actual effect of data co-registration is expected smaller than showed by numerical test in the present study. If further clarifications are desired the analysis with involvement of the team generated the Level 1B data is desirable.

7. Conclusions

Based on the materials presented in this report we can make the following conclusions:

- The enhanced Near Real Time aerosol algorithm for retrieving aerosol from 3MI observation has been developed and tested with synthetic 3MI data. The algorithm is based on GRASP retrieval concept. It retrieves properties of aerosol and surface simultaneously. The retrieved detailed properties of aerosol include particle sizes, complex index of refraction, spectral AOD, single scattering albedo, fraction of non-spherical particles. For surface reflectance full BRDF and BPDF are retrieved.
- The extensive tests showed that time EUMETSAT required for processing one orbit can be successfully achieved with proposed algorithm using rather modest computer cluster of ~ 100 cores. This can be viewed as a considerable success taking into account that GRASP algorithm performs full radiative transfer calculations on line.
- In frame of this project the function for co-registration of 3MI data was comprehensively tested. First, the results of EUMETSAT co-registration were compared with results generated by NOVELTIS co-registration function developed within this project. The comparisons showed that EUMETSAT co-registration is superior. Also, the effect of co-registration errors on retrieved aerosol parameters was evaluated. The analysis showed that the errors in Level 1C data due to co-registration can be estimated on the level of ~0.6% for intensity and 0.002 for polarization and aerosol spectral optical thickness is retrieved with sufficient accuracy.

Thus, the results of this project can be considered as highly successful.

8. Identified Issues

During the project execution some managerial and scientific issues were identified

8.1 Managerial issues

Unfortunately, the project was delayed due to several following issues:

- The start of the project was delayed because some legal issues in project set up were identified by CNRS. The clarification of these issues took at least three months. That experience will be taken in account in preparation of future EUMETSAT projects to avoid similar delays.
- During the project the volume of the efforts was significantly increase due to several factors:
    - Format of 3MI data is of high complexity was set and modified during the project. The final version of format was established only in the beginning 2018;
    - The Synthetic data of Level 1B were corrected several times and the version appropriate for utilization was released also only in the beginning of 2018.

- Some additional work was required with ideal Level 1C data simulation. The use of such data was not originally planned in the project.

8.2 Scientific issues

As scientific issue we would like to mention that we found very difficult and practically impossible to demonstrate full potential of the algorithm using 3MI Level 1C co-registered data by UMETSAT or "ideal data" provided by EUMETSAT. The following specific issues can be listed:

- In order to verify retrieval of different aerosol parameters such as AOD, single scattering albedo, it is necessary to have data corresponding to wide range of each parameter variability. In contrast the synthetic data provided by EUMETSAT are dominated by low AOD for cloud free scenes and one type of aerosol (e.g. absorbing aerosol is not well represented)
- The aerosol parameters used for generation the synthetic data are provided in the format that is not convenient for comparisons with retrieved data (not all parameters are given explicitly). The independent reproduction has not been done. We have done significant efforts with a help of the scientific team that designed these data to reproduce the calculations. As a result, we succeeded for very limited set of data to achieve good consistency. *However, for large set of data it turned to be very efforts consuming that could not be completed in frame of this project.* Some more detailed explanations can be found in Section 5.5.
- The simulated data are directly based on climatologies and reanalysis of data used in climate modelling. These data provide good physical basis but they may not be the best basis for simulating measurements of radiation. In fact, due to uncertainties in those data the resulting simulation may not be fully consistent with the atmospheric radiation models used in remote sensing. For example, vertical variability of aerosol size distribution and complex refractive index is highly uncertain and may not be consistent with scenario used in EUMTSAT simulations where aerosol is represented as a mixture of several components with fully vertically constant properties and varying concentrations. At the same time, such scenario can't be realized in the retrieval algorithm and therefore full consistency in "error free" conditions cannot be achieved.

In general, the best approach for sensitivity tests is to work with simulated data generated to represent wide realistic variability of aerosol properties. Also, it is desirable the availability of simulated data with different level of complexity, i.e. starting from the data that can be fully reproduced by forward model of retrieval algorithm and going to more complex scenarios based on assumptions which can't be fully accounted in the retrieval (complex vertical variability, inhomogeneous aerosols, non-spherical, etc). These suggestions can be accounted in future studies on exploration of the 3MI potential for aerosol retrieval.

Also, it should be noted that most of the factors mentioned above were anticipated and listed as **"Risks"** in original submitted project quoted below:

"However, the following risks and challenges were identified:

- (***General***) The implementation of such project including rather different research and technical tasks during relatively short period of 15 month is challenging since some efforts are original and rather unique;
- (***General***) There are some uncertainties in estimation of efforts related to ***limited availability of EUMETSAT information about expected development strategy and data formats.***
- (***Tasks 2 and 6***) The usage of EUMETSAT generated 3MI observations ***is based on the assumption of complete coherence of EUMETSAT synthetic data with real atmospheric properties and observation***. The appearance of any inconsistencies may results in necessity of unplanned work;
- (***Tasks 2 and 6***) Sufficient clarity and completeness and documentation for the algorithms (LUT base algorithm), level 1b synthetic data set and software (co-registration function) provided by EUMETSAT is expected;
- (***Tasks 2.2 and 6.1***) SOW of this study states in sub-Task of Task 2, the requirement of generating independent level 1b synthetic 3MI data set. However, similar requirement was a main objective of entire study (see EUM/MET/SOW/12/680615: "on Test Data for the EPS-SG instruments METimage and 3MI") of scale similar to present study. Therefore, the requested effort seems disproportional to one sub-Task scale. Correspondingly, the clarification of EUMETSAT expectations regarding scale of efforts and provided support (information, software, etc.) for this sub-Task is critical for success of the Task completion;
- (***Task 6***) EUMESAT's and Contractor's co-registration algorithms will be evaluated and compared to each other at the end of the project. In case of appearance of any inconsistencies, the possible effect on the retrieval will not be addressed fully. Comparison of the different co-registration algorithms should rather be a subject of separate project in advance to this project."

9. References

ATBD (Algorithm Theoretical Basis Document), ERA – Enhanced Retrieval of Aerosol properties: reference and NRT algorithm prototype for 3MI mission project, deliverable to EUMETSAT.

Bréon, F.-M., D. Tanré, P. Lecomte, and M. Herman, **1995**: Polarized reflectance of bare soil and vegetation: measurements and models. *IEEE Trans. Geosci. Remote Sens*. 33, 487–499.

Cairns, B., E. E. Russell, and L. D. Travis, **1999**: The Research Scanning Polarimeter: calibration and ground-based measurements. *Proc. SPIE* 3754, 186–196.

Cox, C., and W. Munk, **1954**: Measurements of the roughness of the sea surface from photographs of the Sun's glitter. J. Opt. Soc. Amer., 44, 838-850.

Derimian Y., O. Dubovik, D. Tanre, P. Goloub, T. Lapyonok, and A. Mortier, **2012**: Optical properties and radiative forcing of the Eyjafjallajökullvolcanic ash layer observed over Lille, France, in 2010. *J. Geophys. Res*. 117, D00U25

Deuze, J. L., F. M. Bréon, C. Devaux, et al., **2001**: Remote sensing of aerosols over land surfaces from POLDER-ADEOS-1 polarized measurements. *J. Geophys. Res*. 106, 4913–4926.

Diner, D. J., A. Davis, B. Hancock, G. Gutt, R. A. Chipman, and B. Cairns, **2007**: Dual-photoelastic-modulator-based polarimetric imaging concept for aerosol remote sensing. Appl. Opt. 46, 8428–8445.

Dubovik, O., and M. D. King, **2000**: A flexible inversion algorithm for retrieval of aerosol optical properties from Sun and sky radiance measurements, J. Geophys. Res., 105, 20673–20696.

Dubovik O., B. Holben, T. F. Eck, et al., **2002**: Variability of absorption and optical properties of key aerosol types observed in worldwide locations, J. Atmos. Sci., 59, 590-608.

Dubovik, O., A. Sinyuk, T. Lapyonok, B. N. Holben, M. Mishchenko, P. Yang, T. F. Eck, H. Volten, O. Munoz, B. Veihelmann, W. J. van der Zander, M. Sorokin, and I. Slutsker, **2006**: Application of light scattering by spheroids for accounting for particle non-sphericity in remote sensing of desert dust, J. Geophys. Res., 111, D11208, doi:10.1029/2005JD006619d.

Dubovik, O., Herman, M., Holdak, A., Lapyonok, T., Tanré, D., Deuzé, J.L., Ducos, F., Sinyuk, A., Lopatin, A., **2011**: Statistically optimized inversion algorithm for enhanced retrieval of aerosol properties from spectral multi-angle polarimetric satellite observations. Atmos. Meas. Tech. 4, 975–1018.

Dubovik, O., Lapyonok, T., Litvinov P., Herman, M., Fuertes, D., Ducos, F., Lopatin, A., Chaikovsky, A., Torres, B., Derimian, Y., Huang, X., Aspetsberger, M., and Federspiel, C., **2014**: GRASP: a versatile algorithm for characterizing the atmosphere. SPIE. 10.1117/2.1201408.005558.

Gerrit de Leeuw, Thomas Holzer-Popp, et al., **2015**: Evaluation of seven European aerosol optical depth retrieval algorithms for climate analysis. Remote Sensing of Environment, 162, 295-315.

Flowerdew, R. J., and J. D. Haigh, **1996**: Retrieval of aerosol optical thickness over land using the ATSR-2 dual-look satellite radiometer. Geophys. Res. Lett. 23, 351–354.

Hasekamp, O. P. and Landgraf, J., **2007**: Retrieval of aerosol properties over land surfaces: capabilities of multiple-viewing-angle intensity and polarization measurements, Appl. Optics, 46, 3332– 3344.

Herman, M, J.-L. Deuzé, A. Marchant, B. Roger, and P. Lallart, **2005**: Aerosol remote sensing from POLDER/ADEOS over the ocean: Improved retrieval using a nonspherical particle model, J. Geophys Res., 110, D10S02, doi : 10.1029/2004JD004798.

Holben, B. N., T. F. Eck, I. Slutsker, et al., **1998**: AERONET - A federated instrument network and data archive for aerosol characterization, Rem. Sens. Environ.

Holzer-Popp T., G. de Leeuw, D. Martynenko, et al., **2013**: Aerosol retrieval experiments in the ESA Aerosol_cci project. Atmospheric Measurement Techniques, 6, 2353-2411.

Hovenier, J.W., Van der Mee, C., Domke, H., **2004**. Transfer of polarized light in planetary atmospheres. Kluwer academic Publishers.

Kahn R. and B. Gaitley, **2015**: An analysis of global aerosol type as retrieved by MISR. *J. Geophys. Res*. 120, 4248.

Kokhanovsky, A. A., and G. de Leeuw (Eds.), **2009**: *Satellite Remote Sensing Over Land* (Springer, Berlin).

Kokhanovsky A. et al., **2016:** EPS-SG Multi-View, -Polarisation, -Spectral Imager (3MI) Level 2 Algorithm Theoretical Basis Document (Aerosol). EUMETSAT

Li, X., and A. H. Strahler, **1992**: Geometrical-optical bidirectional reflectance modeling of the discrete crown vegetation canopy: effect of crown shape and mutual shadowing. IEEE Trans. Geosci. Remote Sens. 30, 276–292.

Litvinov, P., O. Hasekamp, B. Cairns, and M. Mishchenko, **2010**: Reflection models for soil and vegetation surfaces from multiple-viewing angle photopolarimetric measurements. J. Quant. Spectrosc. Radiat. Transfer 111, 529–539.

Litvinov, P., O. Hasekamp, and B. Cairns, **2011a**: Models for surface reflection of radiance and polarized radiance: comparison with airborne multi-angle photo-polarimetric measurements and implications for modeling top-of-atmosphere measurements. Remote Sens. Environ., doi:10.1016/j.rse.2010.11.005.

Litvinov, P., Hasekamp, O., Cairns, B., Mishchenko, M., **2011b**: Semi-empirical BRDF and BPDF models applied to the problem of aerosol retrievals over land: testing on airborne data and implications for modeling of top-of-atmosphere measurements, in: Mishchenko, M.I., Yatskiv, Y.S., Rosenbush, V.K., Videen, G. (Eds.), *Polarimetric Detection, Characterization and Remote Sensing*. Springer Netherlands, Dordrecht, the Netherlands. NATO Science for Peace and Security Series C: Environmental Security, pp. 313–340.

Litvinov, P., Hasekamp, O., Dubovik, O., Cairns, B., **2012**: Model for land surface reflectance treatment: Physical derivation, application for bare soil and evaluation on airborne and satellite measurements. J. Quant. Spectrosc. Radiat. Transfer 113, 2023–2039.

Maignan, F., F.-M. Bréon, E. Fedele, and M. Bouvier, **2009**: Polarized refectances of natural surfaces: Spaceborne measurements and analytical modeling. Remote Sens. Environ. 113, 2642–2650.

Mishchenko, M. I., and L. D. Travis, **1997a**: Satellite retrieval of aerosol properties over the ocean using polarization as well as intensity of reflected sunlight. J. Geophys. Res. 102, 16989–17013.

Mishchenko, M. I., and L. D. Travis, **1997b**; Satellite retrieval of aerosol properties over the ocean using measu-rements of reflected sunlight: Effect of instrumental errors and aerosol absorption, J. Geophys. Res., 102, 13543–13553.

Popp T., G. de Leeuw, C. Bingen, C. Brühl, V. Capelle, A. Chedin, L. Clarisse, O. Dubovik, R. Grainger, J. Griesfeller, A. Heckel, S. Kinne, L. Klüser, M. Kosmale, P. Kolmonen, L. Lelli, P. Litvinov, L. Mei, P. North, S. Pinnock, A. Povey, C. Robert, M. Schulz, L. Sogacheva, K. Stebel, D. Stein Zweers, G. Thomas, L. Gijsbert Tilstra, S. Vandenbussche, P. Veefkind, M. Vountas and Y. Xue, **2016**: "Development, Production and Evaluation of Aerosol Climate Data Records from Euro-pean Satellite Observations (Aerosol_cci)", Remote Sens., 8, 421; doi: 10.3390/rs8050421.

Rondeaux, G., and M. Herman, **1991**: Polarization of light reflected by crop canopies. Remote Sens. Environ. 38, 63–75.

Roujean, J.-L., M. Leroy, and P.-Y. Deschamps, **1992**: A bidiractional reflectance model of the Eart's surface for the correction of remote sensing data. J. Geophys. Res. 97, 20455–20468.

Ross, J. K., **1981**: The Radiation Regime and Architecture of Plant Stands (Dr. W. Junk Publishers, The Hague, The Netherlands).

Sayer, A. M., A. Smirnov, N. C. Hsu, and B. N. Holben, **2012**: A pure marine aerosol model, for use in remote sensing applications, J. Geophys. Res., 117, D05213.

Strahler, A.H., Muller, J.-P., **1999**: MODIS Science Team Members. MODIS BRDF/Albedo Product: Algorithm Theoretical Basis Document Version 5. MODIS Product ID: MOD43 Version 5.0.

Tanre D, Breon F-M, Deuze JL, Dubovik O, Ducos F, Francois F, et al., **2011**: Remote sensing of aerosols by using polarized directional and spectral measurements within the A-Train: the PARASOL mission. Atmos Meas Technol 4, 1383–95.

Veefkind, J. P., G. de Leeuw, P. Durkee, **1998**: Retrieval of aerosol optical depth over land using two-angle view satellite radiometry during TARFOX. *Geophys. Res. Let.* **25**, 3135–3138.

Volten, H., O. Munoz, E. Rol, J.F. de Haan, W. Vassen, and J.W. Hovenier, **2001**: Scattering matrices of mineral aerosol particles at 441.6 nm and 632.8 nm , *J. Geophys. Res.* 106, D15, 17,375-17,401.

Voss, K.J., A. Morel, and D. Antoine, **2007:** Detailed validation of the bidirectionnal effect in various Case 1 waters for application to ocean color imagery, Biogeosciences, 4, 781-789.

Wanner, W., X. Li, and A. H. Strahler, **1995**: On the derivation of kernels for kernel-driven models of bidirectional reflectance. J. Geophys. Res. 100, 21077–21089.